UNIVERSITÀ DI PARMA

UNIVERSITA' DEGLI STUDI DI PARMA

PhD PROGRAMME IN
" Civil Engineering and Architecture "

XXXVII CYCLE

THERMO-MECHANICAL OPTIMIZATION OF MATERIALS AND STRUCTURES

Coordinator:
Prof. Andrea Spagnoli

Tutor:
Prof. Roberto Brighenti

PhD Candidate: Farzad Tatar

ACADEMIC YEARS: 2021/2022 – 2024/2025

Acknowledgment

I would like to express my sincere gratitude to my supervisor, Professor Roberto Brighenti, for his invaluable guidance, unfathomable patience, and constant support throughout the course of my PhD period.

I would also like to express my appreciation to my friends and colleagues, Matteo and Alberto who have made this journey both enriching and enjoyable. Whether it was through the guidance with Italian tips or simply providing encouragement during challenging moments, your support is truly appreciated. I also express my sincere gratitude to my lifelong friends, Reza, Mehdy, Behrouz, Reza, Sam, and Mostafa, for their permanent support.

Finally, I owe my deepest gratitude to my family, especially my parents, Cheragh-Khan and Gol-banou, for their unconditional love and support. Your encouragement during my academic path have been my core of strength and serenity. This work would not have been possible without your constant support.

Abstract

This thesis presents a comprehensive investigation into topology optimization (TO) and its applications to structural and thermal systems. It spans theoretical developments, computational implementations, and practical validations, with a focus on enhancing efficiency, accuracy, and versatility in addressing complex engineering challenges. The development and application of the Immersed Level-Set Topology Optimization (ILSTO) framework, which decouples the finite element (FE) mesh from the level-set (LS) grid, enabling precise boundary representations without the computational burden of adaptive meshing is the central novelty of the thesis.

The research is organized into three thematic areas: (1) the design and characterization of advanced lattice and metamaterial structures, including Triply Periodic Minimal Surface geometries and porous metaplates (2) a critical review and development of numerical approaches in TO, highlighting the potential of LS-based methods and their integration into multi-physics frameworks; and (3) applications of ILSTO in thermo-mechanical TO, addressing problems involving conflicting objectives such as minimizing structural compliance and thermal transport simultaneously.

Key contributions include novel strategies for mapping field variables between the FE mesh and LS grid, enhanced convergence criteria, and innovative interpolation schemes to balance computational cost and solution accuracy. The findings demonstrate the robustness of the ILSTO framework in solving complex TO problems while maintaining flexibility for extensions to nonlinear material models thus soft robotics applications, multi-scale designs, and integration into commercial FEM software.

This work not only bridges theoretical and practical advancements in TO but also lays the foundation for future developments in high-performance structural design, offering insights into optimizing multi-functional materials and systems for engineering applications.

Table of Contents

List of Figures

Acronyms

ILSTO :	Immersed Level Set Topology Optimization
LS :	Level Set
LSM :	Level Set Method
PLSM :	Parametric Level-Set Method
LSF :	Level Set Function
TO :	Topology Optimization
ALM :	Augmented Lagrange Multiplier
RBF :	Radial Basis Function
OF :	Objective Function
TPMS :	Triply Periodic Minimal Surface
LSTO :	Level Set Topology Optimization
GP :	Gauss Point
FE :	Finite Element
IDW :	Inverse Distance Weighted
MSTO :	Multi Scale Topology Optimization

NOMENCLATURE

$\Gamma(t)$	:	Material boundary at time t
$\varphi(\boldsymbol{x})$	:	Level set function
$\boldsymbol{x}$	:	Generic location
$\boldsymbol{x}_i = (x_{i1}, x_{i2})$	:	grid node location
$dV\,, dA$	:	Differential volume or area elements
$f(\boldsymbol{x})$	:	Objective function
$\|\ \|$	:	Norm
$\boldsymbol{v}(\boldsymbol{x}, t)$	:	Velocity extension field normal velocity to the LS surface
Ω	:	material boundary
D	:	design domain
L	:	LS domain
C	:	iso-value of the function
$\nabla_{\boldsymbol{x}}$	:	Gradient operator
t	:	time
Δt	:	fictitious time step
$\boldsymbol{t}$	:	Traction force vector
$\boldsymbol{T}_n$	:	Nodal temperature values
$H(\varphi)$	:	Heaviside (step function)
$w_i(t)$	:	time-dependent weights for LSF parametrization
R_i	:	Euclidean radial distance
$\boldsymbol{P}$	:	Polynomial vector
$\bar{\delta}$	:	distribution function replacing the gradients
$\overline{\|\nabla\varphi(\mathbf{x})\|}$	:	average of the LS gradient calculated along $\Gamma(t)$
$\bar{V},\quad \bar{A}$	:	Target volume or area
ψ_{st}	:	Strain energy density
$\boldsymbol{\varepsilon}, \boldsymbol{\sigma}$	:	Strain and stress tensors
$\boldsymbol{C}$	:	Elasticity tensor
$\boldsymbol{u}$	:	displacements field
$\boldsymbol{w}$	:	an arbitrary virtual displacement field
Γ_u and Γ_t	:	displacements and surface tractions imposed on Γ_u and Γ_t
$\boldsymbol{N}(\boldsymbol{x})$	:	Shape function matrix

$\boldsymbol{B}(\boldsymbol{x})$	:	strain-displacement matrix
$\boldsymbol{K}$	:	Global stiffness matrix
$\lambda\,(\Omega(\varphi), t)$	:	constraint term in ALM method
$c(\varphi, t)$	:	constraint function
$\boldsymbol{k}$	:	thermal conductivity tensor
κ	:	thermal conductivity
$\boldsymbol{Q}$	:	heat source/sink
$\overline{T}$ on Γ_T	:	Dirichlet BCs
$k\,\nabla T \cdot \boldsymbol{n} = \overline{\boldsymbol{q}}$ on Γ_q	:	Neumann BCs
ψ_{th}	:	heat transport potential capacity
γ^n	:	penalty parameter for ALM
μ	:	Lagrange multiplier for ALM
V_n, A_n	:	Varying target volume or area at iteration n
β	:	weight parameter
c_t	:	Scaling factor for CFL-based time step
L_e	:	FE characteristic length
f, g	:	Scaling factors for distribution function $\bar{\delta}$ and interpolation support radius $\overline{R}$
ds	:	minimum LS grid size
d_{ij}	:	Distance
p	:	Penalizing exponent for interpolation
$\overline{R}$	:	support radius of the local interpolation
e, c	:	Small positive values to avoid singularities

Chapter 1

INTRODUCTION: TOPOLOGY-RELATED PROPERTIES OF STRUCTURES

1.1 Introduction

One of the hot topics in the field of modern engineering is developing new functional materials and structures to meet emerging needs, including physical limitations, numerical capabilities, and manufacturing tools. This field provides two primary strategies: modifying the chemical composition within a material engineering spectrum to obtain new chemical-physics properties or focusing on the layout of materials and designs. Following the latter strategy, this thesis explores how geometrical and topological characteristics can be modified to improve the thermo-mechanical performance with the goal of obtaining optimal lightweight structures in the line of sustainability and cost savings.

In structural mechanics and thermal analysis, topology and geometry significantly influence mechanical and thermal properties. Features such as holes, connectivity, and stress concentrators govern material behavior under mechanical loads, thermal gradients, or combined boundary conditions. From a structural point of view, stress concentrations taking place around voids can weaken structures' strength, whereas the connectivity of a material's internal network enhances load distribution and energy dissipation. The interplay between topology and material performance motivates innovative approaches to push the boundaries of existing design paradigms to new achievements.

1.2 Porous structures and their characteristics

Porous structures or composites, including foams, honeycombs and lattices, with their intricate networks of voids and connections, serve as a natural platform for exploring topological effects, see *Figure 1-1* [1-4]. Their applications span various domains, including lightweight structural components, thermal insulation, and energy absorption, as well as biocompatible structures [5]. Ashby and Medalist appropriately described the efficiency of cellular solids by comparing them to structural engineering components: "Cellular solids are Nature's equivalent of the I-beam" [6]. Within structural mechanics, the use of porous materials represents a convenient strategy to design with the aim of an optimal balance between mechanical strength and weight. Mechanical applications exploit the presence of material where the maximum stress arises [7, 8], while thermal applications leverage the reduced material density to control heat transfer rates [9, 10].

Porous structures can generally be categorized as stochastic or regular. Stochastic porous structures feature randomly distributed pores, often inspired by natural structures, while regular porous structures – which include lattices

and honeycombs – exhibit periodic and uniform distributions of voids, enabling precise control over their properties, see *Figure 1-1* [6].

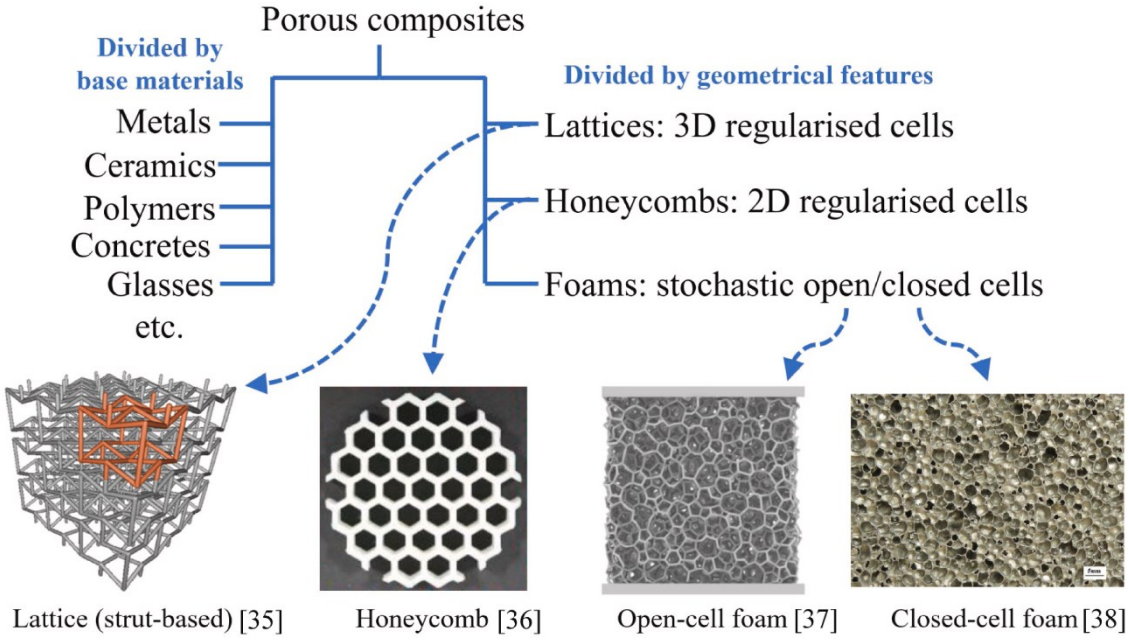

Figure 1-1. *Different porous structures. Foams, honeycombs and lattice structures as geometrically different groups of porous solids. Reproduced under the terms of CC-BY license. © 2023 The Author(s). Published by Elsevier Ltd [4].*

1.3 Towards cellular structures

Among porous materials, a deeper classification can be made to include stochastic and regular porous structures as stated before. Stochastic porous structures, often inspired by natural forms like foams or trabecular bone, feature irregularly distributed pores, resulting in isotropic but less predictable properties. These structures are advantageous for applications requiring randomness, such as shock absorption or fluid permeability [11, 12]. On the other hand, regular porous structures are characterized by periodic and uniform pore distributions. This precise arrangement enables tailored mechanical and thermal properties, suitable for optimized load-bearing applications and/or thermal regulation.

Within regular porous structures, two main categories emerge: strut-based lattices, which consist of interconnected beam-like elements, and wall-based lattices, which are made of continuous sheet-like elements [13]. Both categories provide pathways for exploring innovative material designs, with applications ranging from lightweight structures to enhanced heat exchangers. The interconnected beam-like characteristic of strut-based structures makes them ideal for high stiffness-to-weight ratios. In contrast, wall-based lattice structures utilize sheet-like elements, providing superior performance in applications

requiring enhanced load distribution and thermal conductivity. In general, lattice structures represent a pivotal category characterized by systematic arrangements of struts or walls.

The study of lattice structures has naturally progressed to include geometries such as closed and open cells foams, honeycombs, and triply periodic minimal surfaces (TPMS) which optimize surface area and connectivity. Lattice structures provide tailored mechanical, thermal, and good biological-related behavior, enabling precise performance optimization for specific applications. For instance, TPMS structures have been the focus of many bio-inspired structures due to the TPMS-like structures that exist in many natural structures. Figure 1-2 shows a green hairstreak butterfly whose wings create vibrant colors by diffraction, interference, and selective reflection of light, thanks to Gyroid-like topology embedded in the wings structure [3].

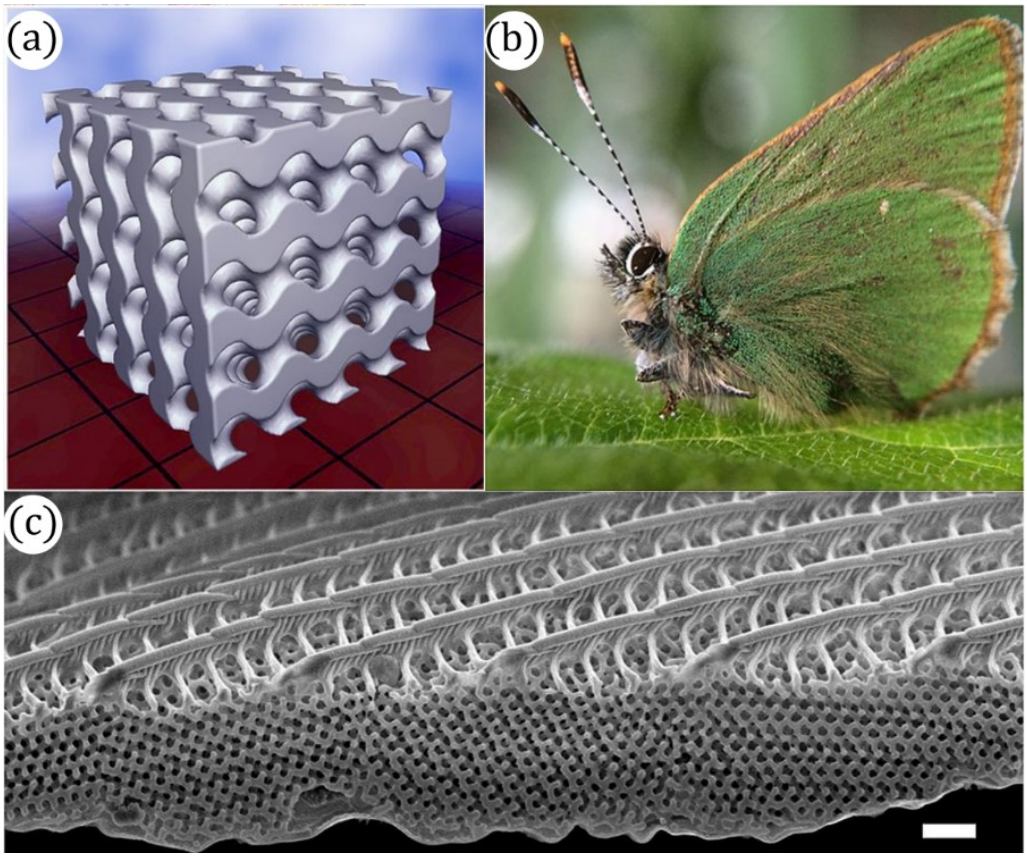

Figure 1-2. CAD model of gyroid TPMS structure with 4×4 unit cells (a). A green hairstreak butterfly (b). SEM image of a wing (c). Scale bar in (c) indicates 1 µm. Reproduced under the terms of the CC BY 4.0 License. published by the Royal Society © 2017 The Authors [3].

1.4 Limits of porous structures and topology optimization

The mechanical and thermal properties of porous materials are typically constrained by theoretical limits, such as those provided by the Hashin-Shtrikman

bounds [14]. These bounds define the maximum achievable effective properties of composites based on the constituent material phases and their relative densities [6]. While these bounds are invaluable for guiding material design, they also impose restrictions that can hinder innovation [15]. By leveraging advanced computational tools and optimization techniques, such as topology optimization (TO), it becomes possible to design materials and structures that approach or even exceed these traditional limits [16].

TO has emerged as a transformative approach for material and structural design [17]. This mathematical approach enables the systematic exploration of design spaces to identify optimal configurations and layouts that satisfy one or more performance objectives (mathematically known as Objective Functions, OFs) while fulfilling well-defined design constraints. In its general form, in optimization problems TO operates through iterative solutions, balancing objectives – like minimizing material usage or minimizing stress concentration – while maximizing stiffness or global thermal conductivity [18, 19].

In the present thesis, the development of an efficient mathematical approach and its computational application aimed at optimizing, from both the mechanical and thermal perspective, a generic structure is presented and discussed in detail, underlying its features, drawbacks, and potentialities. As part of this work, an in-house FE code for performing TO, designed to efficiently handle structural and thermal optimization problems, has been developed using Modern Fortran programming language.

1.5 The structure of the thesis

This thesis relies on the interplay between topological properties, geometric features, and computational optimization to design materials and structures. Chapter 2 focuses on the design of advanced structures and metamaterials considering different functionalities. It begins with an introduction to lattice structures and metamaterials, emphasizing their role in optimizing structures. Then, graded porous TPMS-based structures with a focus on biomechanical applications are considered. The following parts of the chapter are devoted to a group of metamaterials with a focus on thermal and mechanical optimization of the proposed designs. It concludes by identifying advancements in TPMS and metaplate designs, setting the stage for future research directions.

Chapter 3 provides an extensive overview of the existing TO methods explaining the main governing equations and computational techniques. It begins with an overview of structural optimization and presents the role of TO in engineering design. Then, key methods in TO, including Solid Isotropic Material with Penalization (SIMP), Evolutionary Structural Optimization (ESO), and the

Level-Set Method (LSM), are discussed alongside their applications and limitations. Finally, multi-scale and multi-objective TO approaches are also highlighted, underlying their capacity to address complex optimization problems across various physical domains.

Focusing on the theoretical and numerical foundations of LSMs, Chapter 4 details its application to TO. It introduces LS functions for representing interfaces and discusses their evolution using Hamilton-Jacobi equations. The chapter illustrates in detail parametric LSM, LS function initialization, and reinitialization techniques. Applications of LSM in optimizing mechanical and thermal problems are explored, with a detailed explanation of the Augmented Lagrange Multiplier (ALM) method required for handling constraints related to the material use allowed by design requirements.

Chapter 5 presents an innovative Immersed Level-Set TO (ILSTO) approach tailored for combined thermo-mechanical TO. The method decouples the finite element (FE) mesh from the LS grid, enabling superior computational flexibility and precision. It discusses the principles of the ILSTO, regularization techniques, and mapping approaches. The chapter also addresses thermal and mechanical TO based on the FE method, providing insights into convergence strategies and numerical stability. The proposed framework is demonstrated to be a robust tool for solving multi-objective and multi-physics optimization problems. The structure and implementation details of the in-house ILSTO FE code, along with its modular design and computational advantages, are explained thoroughly in this chapter.

In Chapter 6 numerical case studies are provided to validate the proposed ILSTO approach. It includes examples of mechanical, thermal, and combined thermo-mechanical TO problems, demonstrating the flexibility and efficiency of the developed computational strategy. The chapter investigates the impact of various parameters, such as grid density, time step length, and interpolation radius, on optimization results. Each example illustrates the potential of the proposed methods to address real-world engineering challenges.

Finally, Chapter 7 contains the summary of the research conducted across the various chapters, and the main conclusion of the study is provided. Additionally, it discusses the implications of the obtained results and outlines the directions for future research, such as expanding the applicability of the proposed ILSTO frameworks to broader multi-physics and multi-scale optimization problems.

Chapter 2

ADVANCED LATTICE AND METAMATERIAL STRUCTURES FOR THERMAL AND MECHANICAL PROBLEMS

2.1 Introduction to lattice structures and metamaterials

An overview of lattice structures and metamaterials, with an emphasis on their applications, design principles, and recent advancements is provided in the present chapter. It focuses on three-dimensional (3D) and two-dimensional (2D) lattice structures and metamaterials whose structure enables obtaining specific responses in mechanical and thermal conduction problems. A brief literature review on metamaterials and architected materials is provided, and a deep insight into the field is presented in this chapter. It will be demonstrated that various mechanical and thermal responses can be achieved by combining different structures, generating or merging arbitrary voids in 3D or 2D domains.

2.2 TPMS lattice structures: design, experiments, and manufacturing challenges

The development of metamaterials and functional design of structures has advanced significantly over the last decade, especially thanks to modern production processes, such as the Additive Manufacturing (AM) technology [20], enabling to overcome shape and topology limitations typically encountered in traditional material building technologies. The first efforts toward implementing AM-based production dates back to the 1980s, when researchers used this method to create prototypes [21]. AM enables the creation of complex geometries, featuring a wide range of unit cell sizes, that are not attainable with traditional production methods like casting, molding, or machining [22]. Additionally, modern AM processes facilitate multi-material printing, which is promising for creating materials structures with multiple functionalities [23]. Thus, the production feasibility of complex designs calls for a deeper dive into the realm of advanced materials and structures.

This section provides a literature review on lattice structures and their applications such as those in biomechanics. It also covers metamaterials and thermo-mechanical applications of metaplates.

2.3 The importance of lattice structures: TPMS topologies and their functionalities

Lattice structures, known for their interesting and unique physical properties, have gained significant attention over the last years. Tissue engineering, a multidisciplinary field focused on enhancing, restoring, or maintaining damaged or deteriorated natural tissues, particularly benefits from these structures [24, 25]. Thanks to advancements in manufacturing processes, researchers have made

significant progress in bone tissue engineering over the past decades. One method for creating artificial tissues is using AM, a process called bioprinting [26]. In biomimicry, scaffold design is crucial for effective tissue regeneration. In this line of thought, in bone tissue engineering numerous challenges arise from replicating the structure and function of the host bone [27].

A compelling field of application of AM is generating biomimicking organs or artificial tissues. For instance, AM scaffold tissues can bear considerable loads while being efficient and lightweight at the same time [28, 29]. Mimicking the hosting cell heterogeneity is the main advantage of creating artificial tissues using AM. Bone tissues have a heterogenous morphology that can be replicated by printed lattice structures with complex geometry; further, AM is particularly suitable to tailor the material structure according to patient-specific purposes. Therefore, designing and fabricating novel porous structures for bone tissue engineering has been extensively taken into consideration by researchers.

Designing bone scaffolds using a precise mathematical description of the desired shape, has led the researchers to adopt a special class of porous materials known as Triply Periodic Minimal Surface (TPMS) structures [30, 31]. Beyond biological-related applications, these novel geometries are used in various fields, including heat exchangers, body implants, and lightweight structures [32-34]. In biomechanical applications, TPMS-based bone scaffolds offer several advantages such as excellent nutrient transportation, good oxygen diffusion, and ion exchange, etc., making them ideal for cells proliferation leading to tissue regeneration [35, 36]. Their applications in bioengineering have provided innovative solutions for creating biomimetic tissues and organs. For instance, Song et al. designed and analyzed a dental implant based on TPMS structures, and outlined the advantages with respect to traditional implants [37]. It is worth noticing that, due to their geometric complexity, TPMS structures can be nowadays produced only using AM technologies.

In order to mimic natural tissue topology, three main gradings – namely density, cell size, and lattice type – are required [38]. Various surface formulae have been proposed to define unique TPMS lattice structures; among others, the Schoen-Gyroid, Schwarz-Diamond, and Primitive can be mentioned. Depending on the scaffold's mechanical behavior and biological applications, combining these structures can lead to biomechanically efficient structures [39, 40]. Restrepo et al. evaluated three 3D-printed ceramic patterns for bone tissue engineering, while Liao et al. assessed radial-gradient TPMS structures under compressive tests [41, 42]. Another study demonstrated the use of selective laser melting technology to print multi-morphology scaffolds and investigated their mechanical response [43]. However, the adopted cell type has relevant consequences in load-bearing porous

structures, thus requiring a study of the transitional zone in multi-morphological scaffolds.

The literature review indicates that comprehensive studies on multi-morphology scaffolds are still lacking. In the following, multi-morphology bone scaffolds with sudden and gradual transition zones, designed and printed using a Carbon NanoTube Polylactic Acid Polymer (CNT-PLA) filaments within the Fused Deposition Modeling (FDM) AM technology, are considered.

Due to unavoidable printing anomalies in FDM processes, microtomography (μCT) analysis can be usefully employed to assess the printing quality and to determine the actual geometry of the scaffolds. The effects of printing direction, cell type, and filament variation were also examined. Performing complex mechanical tests on specimens remains a challenge in biomechanical research. To address this issue, a method combining microtomography and Finite Element Modeling (μCT-FEM) is used here to evaluate the mechanical behavior of the printed bone-like scaffolds.

2.3.1 Design and optimization of multi-morphology lattice structures

TPMS structures, such as gyroid, diamond, and I-WP lattices, are defined by mathematical equations representing minimal surfaces with high porosity, see Figure 2-1 [26]. These surfaces are generated with precise control over cell size and porosity, allowing to create materials that are both lightweight and strong.

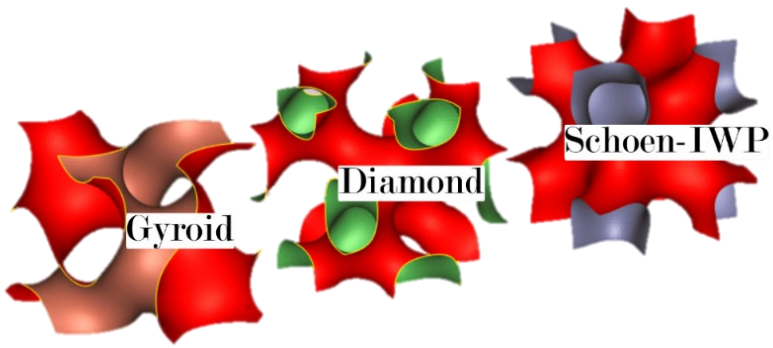

Figure *2-1. Three common TPMS structures [26].*

Each surface is obtained using one of the following equations:

Schoen Gyroid:
$$\sin(2\pi x/d)\ \cos(2\pi y/d) + \sin(2\pi y/d)\ \cos(2\pi z/d) + \sin(2\pi z/d)\ \cos(2\pi x/d) = t \quad (2\text{-}1)$$

Schwarz-Diamond:
$$\cos(2\pi x/d)\ \cos(2\pi y/d)\ \cos(2\pi z/d) - \sin(2\pi x/d)\ \sin(2\pi y/d)\ \sin(2\pi z/d) = t \quad (2\text{-}2)$$

Schoen I-WP:
$$2(\cos(2\pi x/d)\ \cos(2\pi y/d) + \cos(2\pi y/d)\ cos(2\pi z/d) + cos(2\pi x/d)\ cos(2\pi z/d)) - (cos(4\pi x/d) + cos(4\pi y/d) + cos(4\pi z/d)) = t \quad (2\text{-}3)$$

where t defines the iso-surfaces where the periodic cells can exist, x, y, z are the coordinates, and d is the dimension that dictates the size of the unit cell [44]. As can be observed from the above equations, a larger t leads to a denser unit cell. Assuming $\frac{d}{2\pi} = 1$, which leads to the unit cell size with $d = 6.28\ mm$, the following equations are obtained for generating the TPMS structures used in this study:

Schoen Gyroid: $$\sin(x)\cos(y) + \sin(y)\cos(z) + \sin(z)\cos(x) = t \quad (2\text{-}4)$$

Schwarz-Diamond: $$\cos(x)\cos(y)\cos(z) - \sin(x)\sin(y)\sin(z) = t \quad (2\text{-}5)$$

Schoen I-WP: $$2(cos(x)\,cos(y) + cos(y)\,cos(z) + cos(x)\,cos(z)) - (cos(2x) + cos(2y) + cos(2z)) = t \quad (2\text{-}6)$$

Multi-morphology lattice structures, specifically those based on TPMS, provide flexibility in mechanical properties by combining different morphologies within a single scaffold. This capability is particularly useful in biomedical and structural applications, where gradient transitions between regions with distinct mechanical requirements are often desired. Some studies have shown that transition zones between TPMS structures can manage stress distribution, improving load-bearing performance while maintaining structural continuity [30, 31, 38, 45, 46]. The transition zone between different TPMS structures is essential for achieving graded mechanical properties across the lattice, which is particularly beneficial in applications requiring varied load-bearing capacities within a single material. To obtain a multi-morphology structure, the following function controlling the transition between two different lattices is introduced:

$$\varphi_{MML} = \gamma\varphi_G + (1-\gamma)\varphi_D \quad (2\text{-}7)$$

where φ_{MML} is the multi-morphology surface equation for the lattice structure, which is made of two specific lattice types: $\varphi_G\ and\ \varphi_D$. In this study, φ_G and φ_D represent the Schoen-Gyroid and Schwarz-Diamond TPMS structures, respectively. Furthermore, γ is the transitional function introduced for smoothly changing the structure from φ_G to φ_D as follows:

$$\gamma = \frac{1}{1 + e^{Kx}} \quad (2\text{-}8)$$

Depending on the value of the constant K in Eq. (2-8), the multi-morphology structure can change either suddenly or gradually, see Figure 2-5 for more details. Moreover, since the above function γ is defined based on the variable x only, it controls the structure change from φ_G to φ_D along the x coordinate. Further, variations in the lattice type can be achieved by relating this function to the other coordinates. Thus, K is a crucial variable to be carefully taken into account when load bearing capacities of hybrid structures is desired.

2.3.2 3D printing, scanning, and mechanical test of TPMS structures

In this section, the details of practical steps required for the study of TPMS structures are provided. Since the cellular type varies along the x axis according to Eq. (2-8), the longest edge lies along such a direction. After generating the points containing the expected features of the TPMS surfaces, the generated surfaces are converted to volumetric models, then they are exported as STL files. Afterward, the model files are printed using two types of PLA filaments with different mechanical properties. Based on the flowchart of the process shown in Figure 2-2, another FEM analysis is done after printing and scanning the scaffolds using a micro-CT scanner, equipped with a cone-beam micro-focus X-ray source and a flat panel detector, to investigate the effect of printing anomalies. The printing parameters of the Fused Filament Fabrication (FFF) method and the corresponding filaments, which have been implemented for printing these samples, are reported in Table 2-1.

Table 2-1 3D printing parameters used in the study of TPMS structures

Filament	Nozzle temp.	layer height	Deposition speed	Platform Temp.
PLA 1	190^{o}C	50 µm	10 mm/s	24^{o}C
PLA 2	220^{o}C	50 µm	10 mm/s	24^{o}C

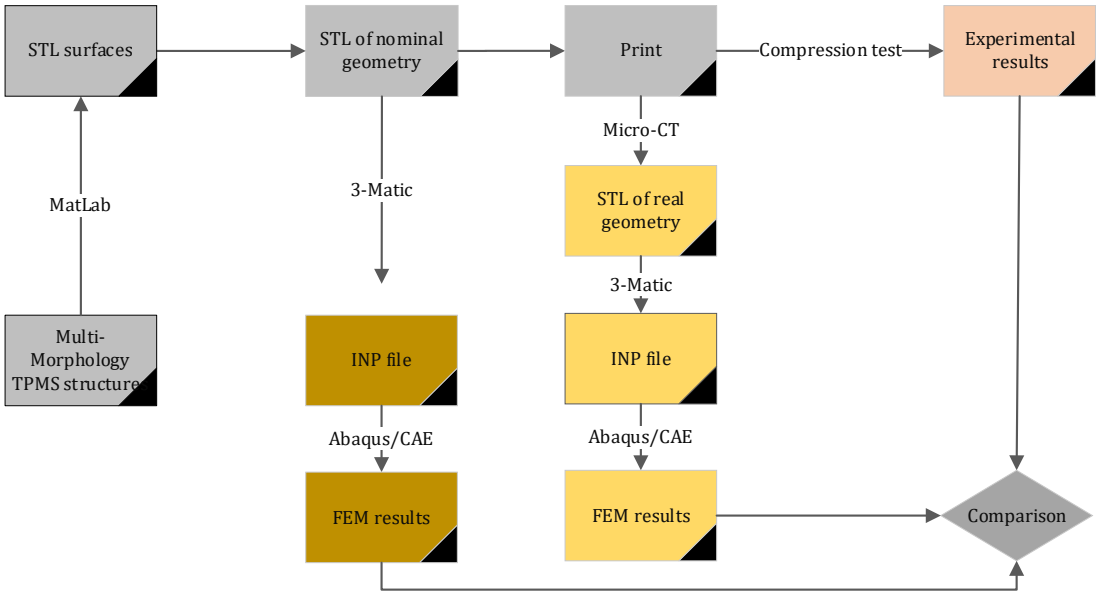

Figure 2-2. Flowchart of the steps and tasks being done in the multi morphology TPMS structures

As can be seen in Figure 2-3, the printing errors, which are mainly due to over extrusion or lack of coasting causing blunt edges, are not negligible. Therefore, it

is necessary to consider them for correcting the FEM results to obtain a precise design of lattice structures when FFF methods are used.

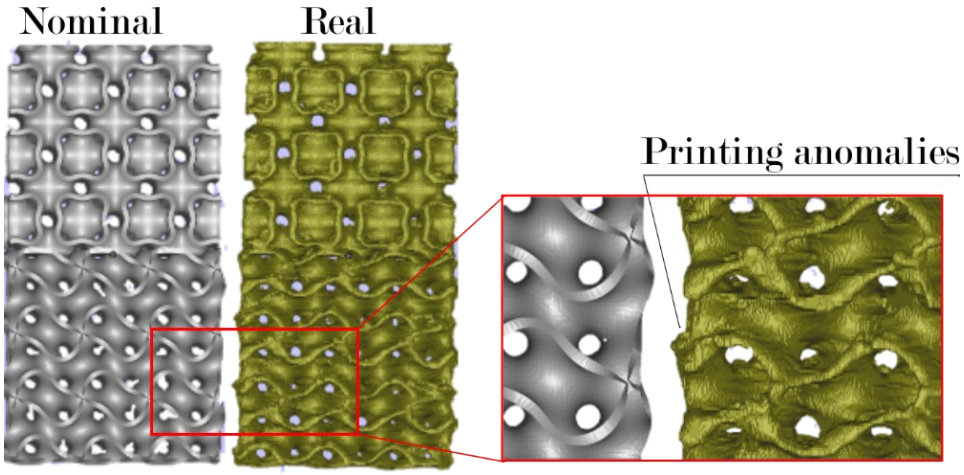

Figure 2-3. Nominal and Real design of bone scaffolds [26].

Mechanical testing of TPMS-based scaffolds involves compression and tensile tests to evaluate the stiffness or the load-bearing capacity. Experimental data reveals that gyroid and diamond TPMS structures provide complementary mechanical benefits, with gyroid offering flexibility and diamond providing rigidity. Flexibility will provide a good opportunity for energy absorption while rigidity provides stiffness. Compression tests on TPMS-based metaplates, designed for both thermal and mechanical optimization, show that they retain high stiffness while facilitating heat dissipation, making them well-suited for applications like heat exchangers or structural panels exposed to thermal fluctuations [45-47].

2.3.3 Experimental results on TPMS-based lattices

This section presents experimental results related to hybrid TPMS structures. It was observed that for structures with identical native scaffolds, a sudden transition from Gyroid to Diamond structures, Figure 2-4b, leads to a stiffer material, highlighting the impact of the transitional zone size on the overall performance. However, this conclusion is not definitive, as the porosity of the porous structures was not uniform, even though the wall thickness was controlled in the scaffold design. It is possible that porosity, rather than the transitional factor K in Eq.(2-8), or the structure type, could be the primary factor influencing the scaffold's performance [6]. Higher porosity results in a lower scaffold density and a reduced stiffness. A relationship to estimate the Young's modulus of porous materials has been proposed in the following form:

$$\frac{E}{E_s} \propto \left(\frac{\rho}{\rho_s}\right)^2 \tag{2-9}$$

where ρ_s indicates the density of the reference material with Young's modulus E_s, while ρ and E represent the corresponding quantities of the porous material of interest, namely the scaffolds. The above relationship does not account for the geometry of the pores; it has been found that the scaffolds' behavior weakly depends on the cell type, while the porosity, i.e. the relative density, plays the main role [26].

Cellular structure topologies allow them to deform by either bending or stretching of the constituent cells [48]. While bending-dominated lattices are recognized with lower stiffness and strength but higher energy absorption, stretching-dominated lattices transfer loads primarily through axial stretching or compression of their struts, resulting in higher stiffness and mechanical efficiency. In this line of thought, according to Figure 2-4a, the Gyroid structure exhibits bending-dominated behavior, while the Diamond structure displays stretching-dominated behavior. As the transitional zone increases, it enhances the smoothness between the walls, favoring the bending behavior over the stretching, see Figure 2-5.

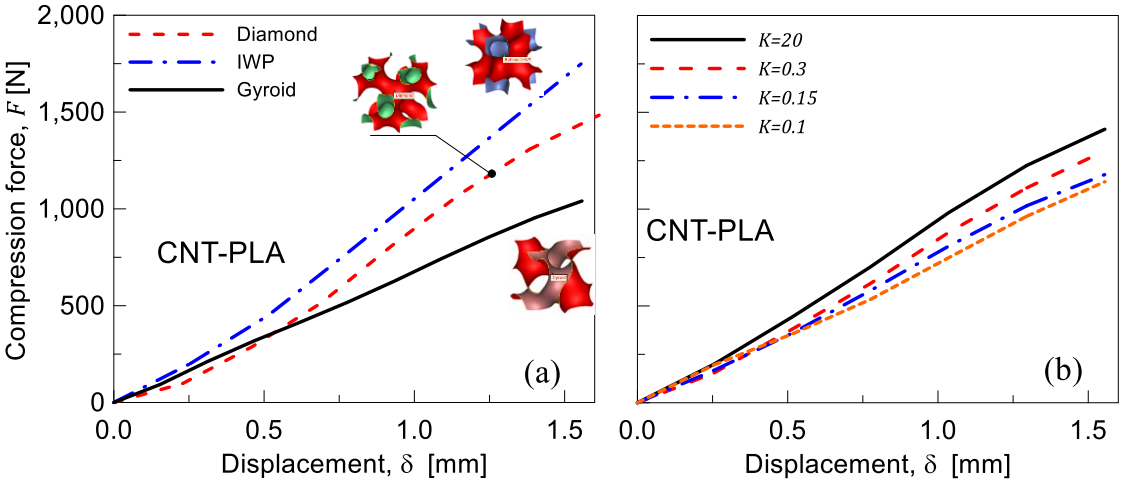

Figure 2-4. *Mechanical response under compression of single-cell scaffolds type: Gyroid, I-WP, and Diamond* (a). *Effect of variation of the transitional zone under compression:* $K = 20$, *sharpest transition to (b)* $K = 0.1$, *smoothest transition [26]. Reproduced under the terms of CC BY-NC 4.0 license. © 2022 Noroozi, et al.*

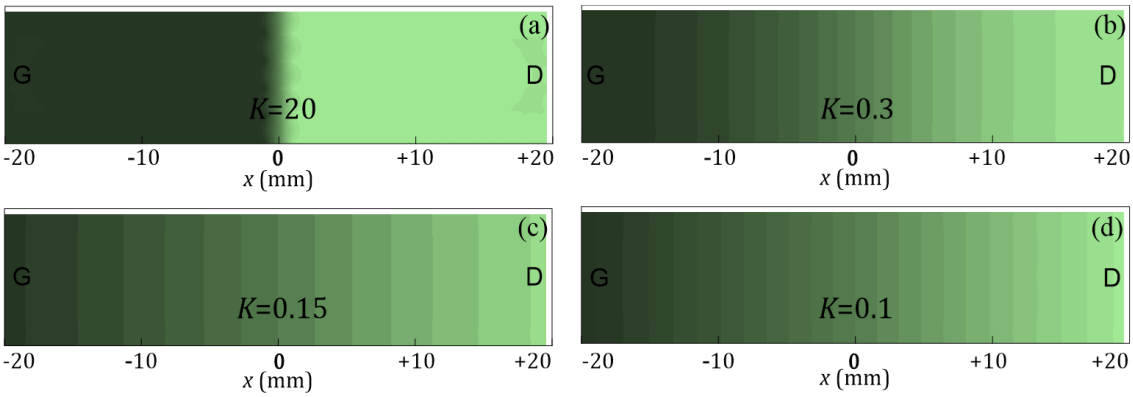

Figure 2-5. Scheme of the geometric transition between two different cell structures (such as Gyroid to Diamond) according to the value of the parameter K in Eq. (2-8) [26]. Reproduced under the terms of CC BY-NC 4.0 license. © 2022 Noroozi, et al.

2.3.4 Finite element modeling of TPMS-based lattices

In this study, a linear elastic material model was used to validate the lattice response during the initial small deformation regime. The load-displacement curves extracted from the linear portion of the experiments were compared with the FEM results for the µ-CT scaffolds to assess and verify the accuracy of the numerical model. After performing a mesh convergence parametric study, the FE model with the highest number of finite elements (approximately 5.2 million tetrahedral elements) was considered as the reference solution, and the rest of models with different mesh densities were compared to it. The model with the optimal mesh, which was identified to have around 2 million elements (among the roughest model with 2×10^5 to the finest one with 5.2×10^6 elements), was imported into ABAQUS as an orphan model. It should be noted that each of the generated meshes were prepared using an external application to produce solid mesh on a scanned scaffold prior to the analysis.

As previously discussed, comparing FEM results of CAD-designed scaffolds with the µ-CT scanned samples of the same CAD file can offer valuable insights into production errors and their impact on the mechanical performance of lattice structures. In this regard, Figure 2-6 shows the von Mises stress contours of a hybrid TPMS lattice containing Gyroid and Diamond structures. Results show that the printing direction has an influence on the final compression performance of the multi-morphology structure. The combination of bending dominated and stretch dominated structures is observed from the hybrid structures scaffold, depending on the dominance of each region during the compression test. A promising conclusion of this study is that both the *real* and *nominal* geometries

of the scaffolds predict the region of failure, regardless of the minor differences in the provided geometrical details.

The von-Mises stress contour in Figure 2-6 reveals that the Gyroid region of the scaffold is more prone to failure because of the higher stress localization compared to the Diamond one. However, notable differences exist between the von-Mises stress contours of nominal geometry and the real specimen (scanned ones). In the nominal geometry, sharp boundaries cause stress concentration, whereas in real specimens such sharp boundaries are absent due to the imprecision of the FFF printing process, resulting in a smoother material distribution. Consequently, predictions based on the real geometry obtained via μCT scans are more accurate than those obtained from nominal scaffolds.

Additionally, the direction of stress concentration in the middle of the Gyroid section varies slightly between the nominal and the real geometry. Load-displacement curves further highlight this discrepancy, showing a 23.49% error in total force for the nominal geometry, compared to 10.70% for the real geometry. This indicates a 12.79% improvement in FEM accuracy when using μCT-derived real geometry. Thus, a better prediction of the mechanical response of TPMS lattice structures is obtained when using μCT-scanned models.

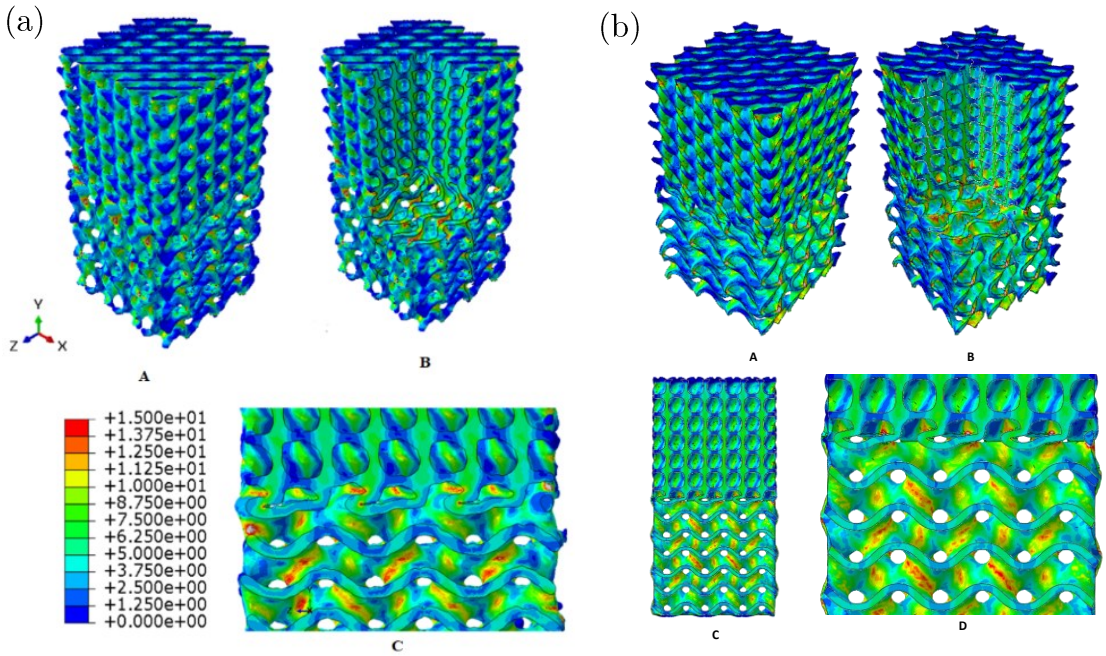

Figure 2-6. Contours of the von Mises stress [MPa] obtained by FEM for a multi-morphology considering its real (a) and nominal (b) geometry [26]. reproduced under the terms of CC BY-NC 4.0 license. © 2022 Noroozi, et al.

2.4 Design and optimization of thermo-mechanical metamaterials

Metamaterials are engineered structures with tailored unit cell topologies, enabling unconventional properties. Their performance is dictated by their topological design, which can enhance stiffness, strength, and thermal conductivity while maintaining low weight. In 2D space, metaplates consist of 2D unit cells embedded in thin plates, allowing precise control over their behavior, mechanical or thermal behavior, for instance.

Metaplates considered in the following are 2D porous structures which are required to be optimized for enhanced thermal and mechanical performance at the same time. The task of optimization involves computational techniques to balance multiple performance objectives. By configuring pore shapes and void orientations designers can create materials that achieve superior thermal transfer without sacrificing mechanical integrity.

Heat transfer contributions beyond conduction, such as radiation and convection, are assumed negligible and are not considered in the present study. Additionally, the holes are assumed to be filled with non-conductive material (e.g., low-conductivity gas or vacuum), preventing heat transfer across the void regions. In the following, a literature review on the metamaterials with a special focus on their thermo-mechanical behavior is provided.

2.4.1 Literature review on metamaterials

Metamaterials, initially designed to control electromagnetic waves, surpass the limitations of conventional materials. Their unique properties stem from the design of their unit cell or Representative Volume Element (RVE), rather than just chemical composition. These engineered materials, named for their ability to go beyond ('meta' in Greek) natural properties, have advanced rapidly in recent years [49-51].

Metamaterials offer remarkable solutions across fields such as mechanics [52-56], optics and magnetism [57, 58], acoustics [59, 60], and biology [61]. They are used in applications like nano/micro-electromechanical devices and biomaterials development [62, 63]. Their unique properties arise from precisely designed unit cells, arranged in patterns smaller than the wavelengths they influence, with tailored topology, shape, geometry, size, and orientation to achieve specific functionalities [64, 65].

The management of thermal properties using metamaterials is a growing field [66-68]. Key applications include mechanical, thermal, and thermo-mechanical systems, showcasing the adaptability of metamaterial design [69-71]. Thermal

metamaterials are classified as functional, which redirect heat flux, and porous, which regulate heat conduction [72]. These innovations could transform thermal management systems, barriers, and thermoelectrics [69, 73-78]. For instance, a thermal concentrator focuses heat, improving thermal storage efficiency. Recent developments also enable thermal and mechanical cloaking [79-81], heat shielding [69, 82], and acoustic control [83]. Metamaterials' precise structural design enables unique properties like wave manipulation and negative refractive indices, not found in conventional materials [84]. Additionally, 3D metamaterials, such as those obtained using TPMS, offer advanced control of heat transfer and fluid flow [26, 46, 85].

It is worth noticing that porous materials, made of solid and void phases, enable control over thermal conductivity [86]. Typically defined by their porosity (volume fraction of voids), other microstructural aspects – such as void size, shape, and connectivity – are often overlooked [73, 87]. While specific heat per unit mass is unaffected, the overall elastic constants and thermal conductivity strongly depend on the porosity and microstructure. To this end, predictive numerical and theoretical models for their thermal and mechanical properties have been widely developed [88-90].

Following the previous statements, this section of the present chapter examines the thermal and mechanical behavior of 2D porous metamaterial plates (metaplates) containing elliptical voids introduced to provide an intrinsic macroscopic porosity. In this way, metaplates can be efficiently designed without considering complex physics for obtaining a metamaterial feature. While the amount of porosity is fixed, the voids' size, shape, position, and orientation vary as design parameters. Both regular and random void configurations are analyzed to study their impact on heat flux and mechanical response. Numerical results are presented, compared, and discussed, together with some 3D printed and mechanically tested plates to validate FE analyses in the linear elastic regime and linear heat conduction flow.

2.4.2 Design of metaplates

According to well-established literature, the lower (Wiener) bound for the dimensionless thermal resistance ρ_L^* and the upper (Paul) bound for the dimensionless mechanical stiffness k_U^* of a generic porous material are well-known as the following:

$$\rho_L^* = \frac{1}{1-p}\,, \qquad k_U^* = 1 - p \tag{2-10}$$

respectively [91]. When an isotropic porous material with porosity p is considered, the above properties are lower or upper bounded by the Hashin-Shtrikman expressions [89]:

$$\rho_{Li}^{*} = \frac{1+p/2}{1-p}, \qquad k_{Ui}^{*} = \frac{1-p}{1+p} \tag{2-11}$$

The above relationships are based only on the material's porosity, without considering microstructural factors like void size, shape, orientation, position, and connectivity so they are valid in the limit of numerous small voids. These parameters, especially the presence of large voids, significantly influence the physical properties of the porous plate, as will be shown in the results section. However, it should be noted that some models, which include also the shape of the voids, for predicting the mechanical stiffness exist [92].

The design process in this chapter involves adjusting the voids parameters such as pore shape, orientation, and location to achieve specific objectives. The multi-objective optimization process balances thermal conductivity with mechanical response by fine-tuning these geometrical features inside an assumed Representative Cell Element (RCE). This ensures that the plate can perform optimally under thermal and mechanical loads simultaneously. It is important to note that the optimization process does not involve reverse design, i.e. it does not identify the best layout through problem-solving. Instead, it selects the best configuration from the analyzed options. Based on Figure 2-8, a parametric study has been conducted to examine the effects of the shape and orientation of the elliptical holes on the thermo-mechanical performance of the metaplates.

2.4.2.1 Thermal conduction in porous media

Thermal conduction, mathematically described by an energy balance equation, is governed by the Fourier's law, which relates the heat flux $\boldsymbol{q}$ to the temperature gradient ∇T via a linear relationship through the thermal conductivity tensor $\boldsymbol{\kappa}$:

$$\boldsymbol{q} = -\boldsymbol{\kappa}\,\nabla T \tag{2-12}$$

For isotropic materials, $\boldsymbol{\kappa} = \lambda\,\mathbf{1}$, where λ is the thermal conductivity of the material. However, in porous media, voids induce local anisotropy, resulting in off-diagonal terms ($\kappa_{ij} \neq 0$ for $i \neq j$). The anisotropy diminishes by increasing the uniformity of the void distribution but remains significant for localized structures.

To model heat conduction in porous domains, a simple theoretical approach is here proposed: it is assumed that, starting from points at elevated temperatures to points characterized by the lowest temperatures, the heat flow follows the shortest path within the domain [16]. The hydrodynamic analogy (modelled through the so-called waterfall algorithms, [93]) of the model is based on the assumption that a water particle – flowing due to a pressure gradient within a medium containing impermeable obstacles (here represented by the voids embedded in the domain) – travels following the shortest path. The heat flux can be approximated as:

$$\tilde{\boldsymbol{q}} = -\tilde{\boldsymbol{\kappa}}\,\nabla T \;\cong -\boldsymbol{\kappa}\,\nabla\tilde{T}\,, \quad \tilde{T}_{,X_i} = c_i^{-1}\,T_{,X_i} \tag{2-13}$$

where $\tilde{\boldsymbol{q}}$ and $\tilde{\boldsymbol{\kappa}}$ are the global heat flux vector and thermal conductivity matrix. $\nabla\tilde{T}$ is the corrected global temperature gradient which is related to the tortuosity of the metaplate along with the heat flow, see Figure 2-7. In other words, the anisotropy of thermal conductivity is assumed to be embedded into the corrected global temperature gradient vector, $\nabla\tilde{T} = \tilde{T}_{,X_i}$, while assuming an isotropic material.

The components of the global temperature gradient, evaluated over the heat path within the porous material, have been expressed by introducing the coefficients $c_i \geq 1$, $i = 1, 2, 3$. Here, c_i quantifies the increase in direction i of the thermal path length due to the path's tortuosity. The coefficients c_i are determined using the waterfall algorithm, which identifies the weighted shortest paths between the hottest T_h and coldest T_l edges of the domain, see Figure 2-7. The average path length in direction X_1 is expressed as:

$$c_1 = \frac{1}{L}\left[\frac{1}{n}\sum_{i=1}^{n} l_{p_i}\right] \tag{2-14}$$

where L is the actual length between T_h and T_l and n is the total number of the considered heat flow paths in the plate and

$$l_{p_i} = \sum_{j=1}^{m} w_j\, l_{p_{ij}} \tag{2-15}$$

where m is the number of either straight or curved segments (see the blue and green lines in Figure 2-7) that constitute the $i-th$ path, and w_j is the weight factor related to each segment. The weights w_j account for the alignment of the path segments with the applied temperature gradient:

$$w_j = 1 + W \ln\left(1 + \frac{\Delta X_{2j}}{\Delta X_{1j}}\right) \geq 1 \tag{2-16}$$

In the previous equation, W is a parameter dependent on void arrangement. According to this equation, the segments with higher geometrical slope ratios ($\Delta X_{2j}/\Delta X_{1j}$ according to Figure 2-7) are more effective in increasing the thermal resistance of the plate. To determine the appropriate number of paths n for evaluating the average minimum path length c_1, numerical simulations have been conducted to effectively calculate c_1. The results show that c_1 becomes nearly independent of n when the number of paths exceeds approximately 150, ensuring reliable estimation across different geometries and arrangements of holes in the considered simple rectangular domain.

By equating Eq. (2-12) and Eq. (2-13), the global thermal conductivity tensor of the porous material is approximated as:

$$\tilde{\boldsymbol{\kappa}} = \lambda \, \mathrm{diag}\,(c_i^{-1}) \tag{2-17}$$

with the corresponding thermal resistance tensor:

$$\tilde{\boldsymbol{\rho}} = \tilde{\boldsymbol{\kappa}}^{-1} = \lambda^{-1} \, \mathrm{diag}\,(c_i) \tag{2-18}$$

The above relations enable to estimate the thermal resistance of the porous domain without extensive computational resources. This model illustrates that, stemming from the tortuous pathways that heat must traverse, porous structures inherently create localized anisotropy even with isotropic materials; this effect is captured by the proposed model.

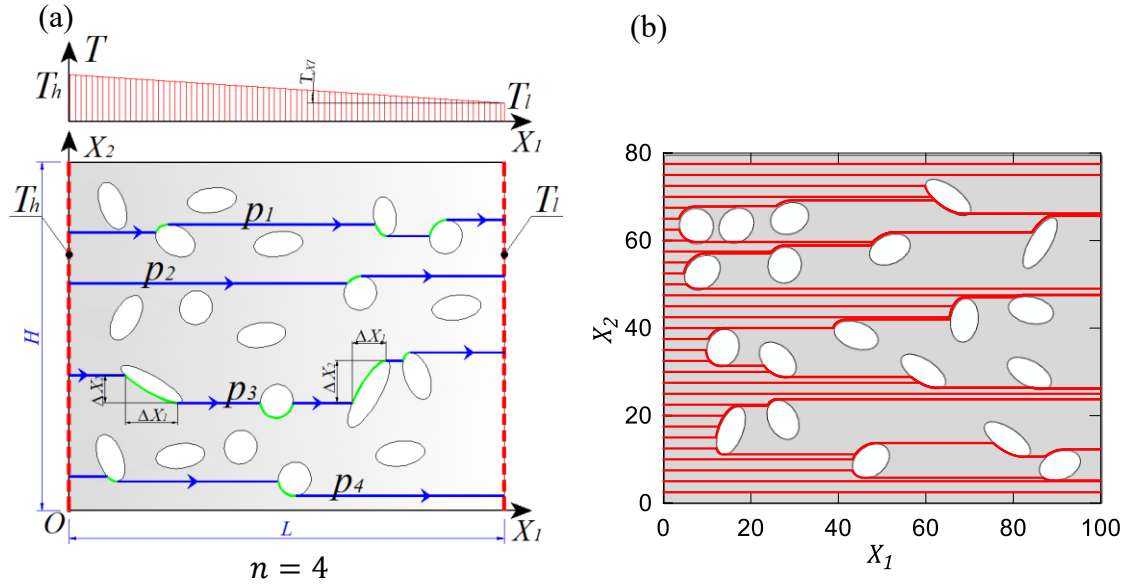

Figure 2-7. Heat flow paths in a porous plate: tortuous routes due to randomly positioned voids. Minimum path lengths computed using the waterfall algorithm: different heat flow paths $p_1 - p_4$, from edge at T_h to the edge with T_l (a). Example of shortest paths obtained in a randomly voided plate (b) [16]. Reproduced under the terms of © 2022 Elsevier Ltd.

2.4.2.2 Regular positioning of voids

In the present section, the considered geometrical parameters include the aspect ratio $r = b/a$, where b and a are the major and minor axes of the elliptical voids, the orientation of the void α, and their position. When the geometrical variables are assumed to vary randomly, the geometrical characteristics of the voids, such as aspect ratio r and the orientation angle α, are assumed to vary within the ranges $1 \leq r \leq 3$ and $-\pi \leq \alpha \leq \pi$, respectively, see Figure 2-8. The positions of the holes' center are set randomly, with appropriate constraints to prevent the voids from intersecting each other or intersecting the plate's boundary.

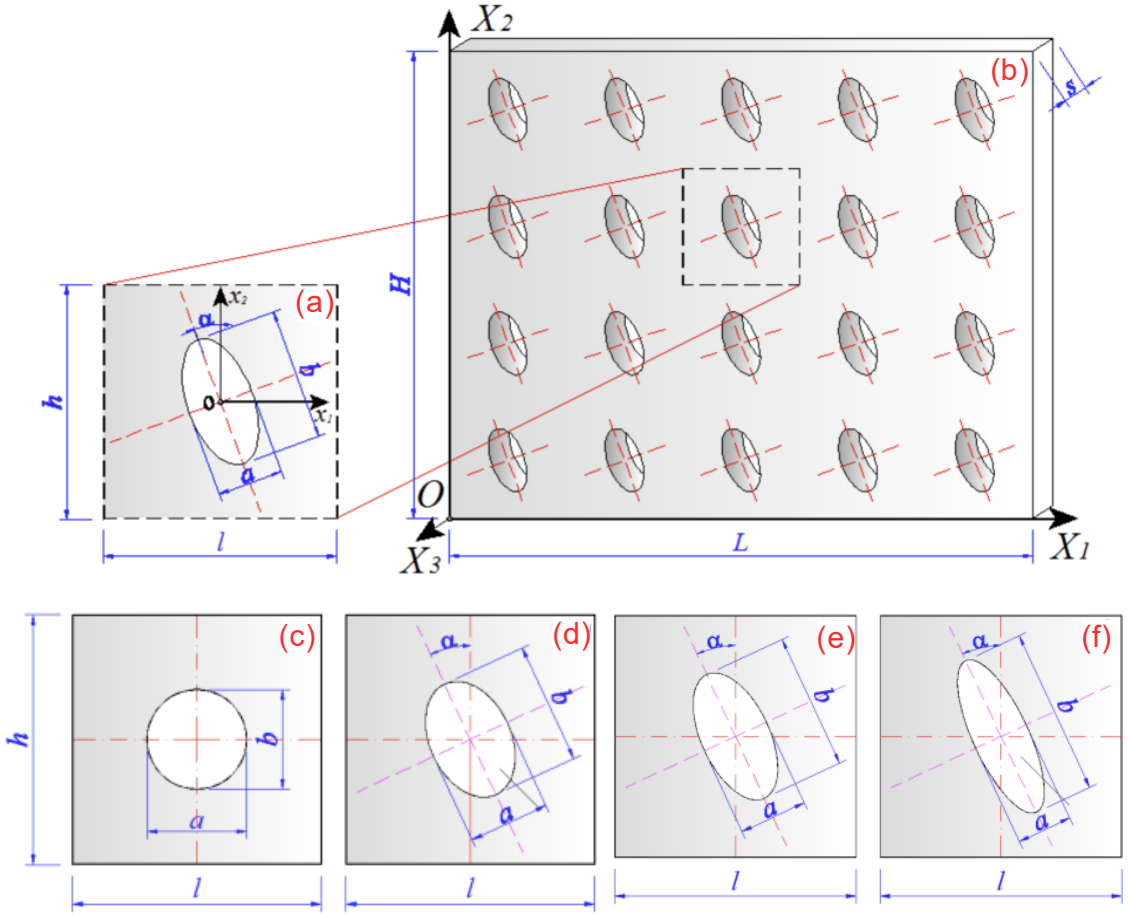

Figure 2-8. RCE featuring an elliptical hole with aspect ratios $r = b/a$ *and orientation* α *(a). Regular assembly of 20 RCEs with constant porosity* $p = 0.04\pi$ *(b). RCEs featuring holes with different geometrical aspect ratios:* $r = 1$ *(c),* $r = 1.5$ *(d),* $r = 2$ *(e) and* $r = 3$ *(f)) and orientation* α *[16]. Reproduced under the terms of © 2022 Elsevier Ltd.*

Moreover, while keeping constant the total amount of voids, the number of holes is increased to determine the size below which the mechanical and thermal characteristics remain unchanged, thereby identifying the homogenization limits. The parameter named as the plate size-unit cell ratio $\gamma = L/l$ is introduced to understand the above-mentioned effect efficiently. Four different layouts with values of plate size-unit cell ratio ($\gamma = 5, \gamma = 10, \gamma = 15, \gamma = 20$) were simulated, two of which are shown in Figure 2-9.

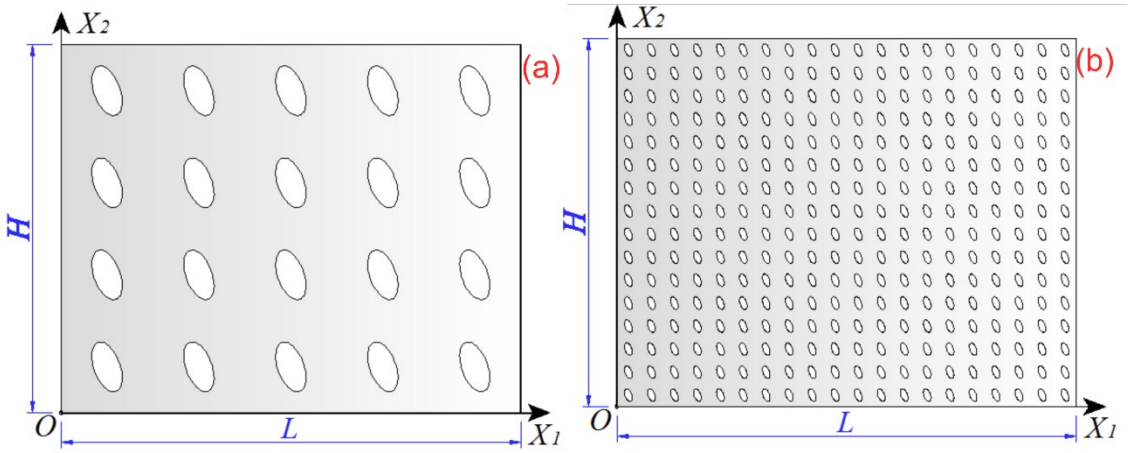

Figure 2-9. Metamaterial plates with an assumed fixed porosity $p = 0.04\pi$ *with regular pattern of identical and equally oriented holes. Plate size-to-unit cell ratio,* $\gamma = L/l = H/h = 5$ *(a), along with intermediate values of* $\gamma = 10$ *and* $\gamma = 15$ *up to* $\gamma = 20$ *were also simulated (b) [16].*

2.4.2.3 Randomizing the geometrical parameters

Porous plates containing randomly arranged voids are studied in this section. In different cases, the position, orientation or the aspect ratio of the voids are randomized by keeping the other geometrical factors either constant or variable. However, for the sake of brevity, we do not provide details for each case. The aspect ratio value is kept between 1 to 3, and the orientation α is limited such that $0 \leq \alpha \leq \pi/2$. Since for each random case the final Objective Functions (OFs) can accidentally improve or worsen, each case is repeated, by randomly generating its geometrical features, for at least 5 times in order to get different final topologies.

For 2D porous plates with a random arrangement of holes, the average plate size-to-unit cell ratio γ cannot be defined as for regular patterns due to the absence of a RCE. Instead, by using the plate's gross area per hole, LH/N , the characteristic length per hole is defined as $l' = \sqrt{LH/N}$, while the plate's overall characteristic length is $L' = H' = \sqrt{LH}$. The average relative fictitious plate size-to-unit cell ratio can then be expressed as:

$$\gamma' = L'/l' = \sqrt{N} \tag{2-19}$$

This quantity will be used to quantify the relative plate size compared to the void size for plates with a random hole arrangement.

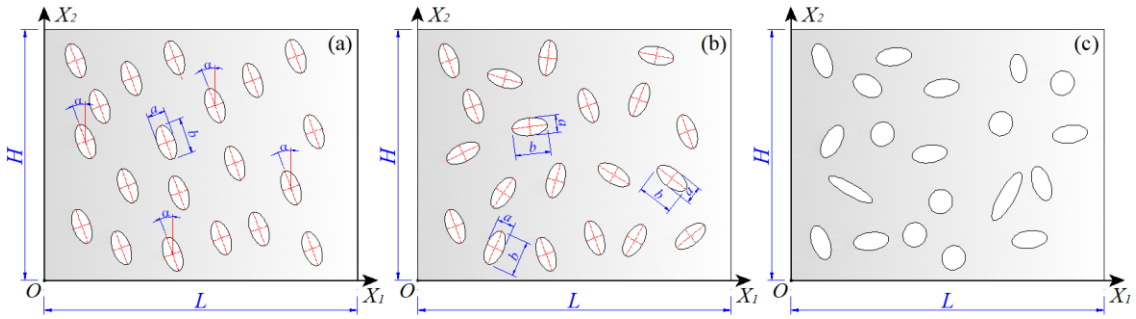

Figure 2-10. Metamaterial plate with fixed porosity $p = 0.04\pi$ given by a random distribution of: identical holes with constant orientation (a), identical holes with random orientation (b), holes with random aspect ratios and random orientation (c). In all cases the area of each hole is assumed to be the same [16]. Reproduced under the terms of © 2022 Elsevier Ltd.

2.4.2.4 Optimization of the combined thermo-mechanical performance

As mentioned in previous sections, the mechanical or thermal response of a 2D metamaterial plate depends on the characteristics and arrangement of its voids. However, the optimal thermal design often does not agree with the mechanically optimal configuration. However, in many applications, achieving the best combined thermal and mechanical performance is essential. To address this, a suitable OF must be defined. The following expression has been adopted for this purpose:

$$f(\boldsymbol{\beta_i}) = a_1\, f_M(\boldsymbol{\beta_i}) + a_2\, f_T(\boldsymbol{\beta_i}) \tag{2-20}$$

where $f_M(\beta_i)$ represents the OF associated with the mechanical problem (e.g., stiffness or compliance under tension, bending, etc.), while $f_T(\beta_i)$ represents the OF for the thermal problem (e.g., thermal resistance or conductivity). The vector $\boldsymbol{\beta_i}$ contains the design parameters (such as r, α, γ, γ', …) and a_1, a_2 are user-defined weighting factors. Both OFs $f_M(\boldsymbol{\beta_i})$ and $f_T(\boldsymbol{\beta_i})$ are normalized with respect to the corresponding properties of a non-porous plate, ensuring $0 \leq f_M \leq 1$, $0 \leq f_T \leq 1$.

2.4.3 Experimental and numerical results on porous metaplates

This section presents the results related to the mechanical and thermal response of metaplates. Regarding the thermal response, both the orientation angle α and the aspect ratio r of the elliptical voids significantly influence the overall thermal resistance. As r increases from the reference case ($r = 1$), the effect of α on the thermal resistance becomes more pronounced, as shown in Figure 2-11 a. The results indicate that for $\alpha \cong 60°$, the influence of r nearly disappears. Additionally, the plot shows that the numerical results generally align with the theoretical lower limit of thermal resistance, ρ^*_{Li}, except for the case where $r = 3$ and $\alpha \to \pi/2$.

The proposed theoretical model satisfactory predicts the thermal resistance of porous domains results, except in cases where $r = 3$. For plates with a regular hole arrangement, the model tends to underestimate the thermal resistance because the weighted average path length is predominantly determined by the first column of holes encountered by the heat flow originating from the (left-hand) edge with the highest temperature.

As for the mechanical response, Figure 2-11b shows that metaplates with voids with a high aspect ratio ($r > 1$) aligned with the loading direction, exhibit an increased stiffness, reaching a maximum when the elliptical holes are perfectly aligned to the load direction ($\alpha = \pi/2$).

The FE results of the metaplates under tension also deviate from the theoretical upper limit of dimensionless stiffness, k_{Ui}^*, for $r > 1$ and $\alpha \to \pi/2$. This discrepancy arises because the theoretical bounds account only for material porosity, ignoring void shape, which significantly affects the overall mechanical properties. However, the FE results demonstrate that the void's shape plays a crucial role in the overall mechanical properties of metaplates. The lower and upper limits of the relative thermal resistance (ρ_{Ui}^*) and mechanical stiffness (k_{Ui}^*), respectively, evaluated according to Eq. (2-11), are illustrated in Figure 2-11.

Experimental tensile test results reflect the general trend of the FE simulations, despite some minor discrepancies can be appreciated. These differences can be attributed to geometric inaccuracies in the 3D-printed metaplates caused by the limited resolution of the FDM printer used, and to the inhomogeneity of the material, despite a 100% infill density has been used to produce the plates. The average Young's modulus of the printed material results to be approximately $E = 2.182\ GPa$. Mechanical tests on the metaplates were confined to the linear response regime being our interest the determination of the plates' stiffness. For low strain values, the material exhibits a nearly perfect linear elastic response. However, deviations occur for strains exceeding about 1%, primarily due to mechanical response of the used PLA material and the FDM-based AM production process, which inherently introduces inhomogeneities and imperfections from the deposition of successive small filaments.

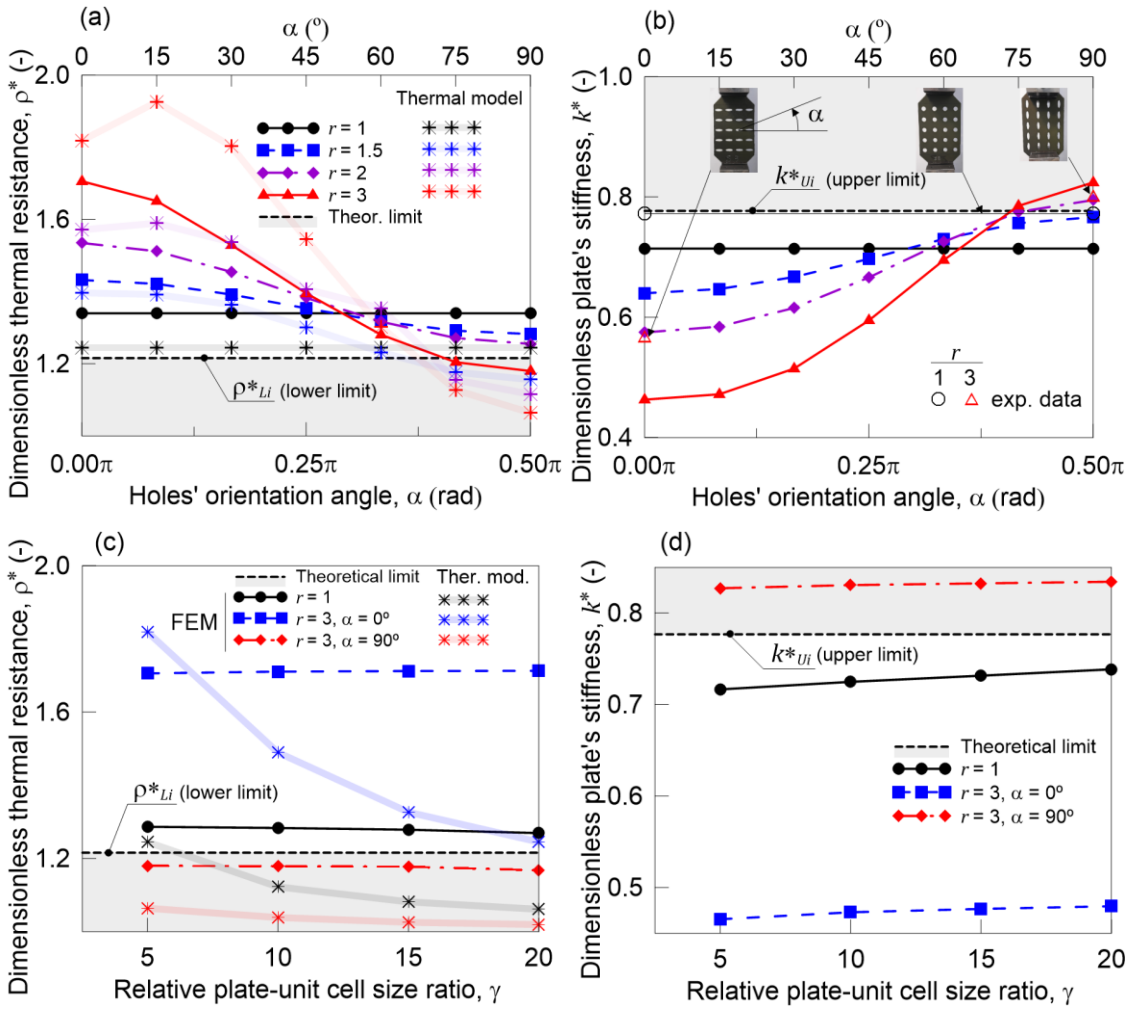

Figure 2-11. Dimensionless thermal resistance (a) and mechanical stiffness (b) vs holes' orientation α for different holes' aspect ratios r. Results provided by the theoretical model and by experimental mechanical tests. Dimensionless thermal resistance (c) and mechanical stiffness (d) vs relative plate-unit cell size ratio, γ, for some different hole's aspect ratios r and angle α. Reproduced under the terms of © 2022 Elsevier Ltd.

To examine the effect of hole size, various cases with different plate-to-unit cell size ratios γ are considered. The four selected values correspond to plates containing 20 ($\gamma = 5$), 80 ($\gamma = 10$), 180 ($\gamma = 15$), and 320 ($\gamma = 20$) holes, respectively, as shown in Figure 2-9.

The numerical results in Figure 2-11c show that thermal resistance is only slightly influenced by the parameter γ, while an increase in the number of holes leads to a moderate rise in stiffness (Figure 2-11d). This indicates that the combined thermo-mechanical performance of the plate improves when a larger number of smaller holes are used, rather than a few larger ones. This result is due to the slight increase in the stiffness of the plates when the number of holes increases while the thermal problem remains almost unchanged.

The theoretical lower limit of thermal resistance is satisfied in all cases except for $r = 3$ and $\alpha = \pi/2$. Similarly, the theoretical upper limit of stiffness is exceeded for $r = 3$ and $\alpha = \pi/2$.

Once the desired OF f is defined, the optimal void configuration can be identified using algorithms designed for solving unconstrained gradient-based optimization problems [94]. The minimum value of the OF Eq.(2-20) is determined using the modified Newton's method. For the combined thermo-mechanical response, an appropriate selection of the OF and its parameters is necessary.

The minimum or maximum of the OF can be determined using the modified Newton's method which employs a line search algorithm along the so-called Newton direction. Starting from an initial design vector, $\boldsymbol{\beta}_k = (r_k, \alpha_k)$, the method iteratively updates the design variables to improve the OF value.

The procedure requires the evaluation of the gradient vector $\boldsymbol{d}$ of the OF, $\boldsymbol{d}(\boldsymbol{\beta}_k) = \nabla f(\boldsymbol{\beta}_k)$, at the point $\boldsymbol{\beta}_k$ of the design space. The search direction $\boldsymbol{p}(\boldsymbol{\beta}_k)$ is calculated as:

$$\boldsymbol{p}(\boldsymbol{\beta}_k) = -\boldsymbol{H}^{-1}(\boldsymbol{\beta}_k)\, \boldsymbol{d}(\boldsymbol{\beta}_k) \tag{2-21}$$

where $\boldsymbol{H}(\boldsymbol{\beta}_k) = \nabla^2 f(\boldsymbol{\beta}_k)$ is the Hessian matrix of the OF. The design vector is updated using a step length χ_k as follows:

$$\boldsymbol{\beta}_{k+1} = \boldsymbol{\beta}_k + \chi_k\, \boldsymbol{p}(\boldsymbol{\beta}_k) \tag{2-22}$$

where χ_k is chosen to satisfy the condition:

$$\begin{aligned} &f\big(\boldsymbol{\beta}_k + \chi_k\, \boldsymbol{p}(\boldsymbol{\beta}_k)\big) < f(\boldsymbol{\beta}_k) \quad \text{(for minimization)} \\ &f\big(\boldsymbol{\beta}_k + \chi_k\, \boldsymbol{p}(\boldsymbol{\beta}_k)\big) > f(\boldsymbol{\beta}_k) \text{ (for maximization)} \end{aligned} \tag{2-23}$$

The process continues until the gradient norm satisfies the convergence criterion. If the OF is sufficiently regular and is characterized by a global minimum (or maximum), the vector $\boldsymbol{\beta}_k$ corresponding to the optimal condition is obtained when the norm of the gradient fulfills the convergence criterion, $\|\boldsymbol{d}(\boldsymbol{\beta}_k)\| \leq \epsilon$, being ϵ a sufficiently small tolerance. This algorithm is here applied to optimize the design of a metamaterial plate with a regular arrangement of holes, as detailed below.

In this context, mechanical compliance and thermal conductivity are used to define the combined OF of the FE results shown in Figure 2-11. Under this assumption, the optimal solution corresponds to minimizing the OF, achieving

maximum thermal insulation and maximum stiffness simultaneously. The combination coefficients in Eq.(2-20) are adjusted to balance the relative importance of these two physical requirements.

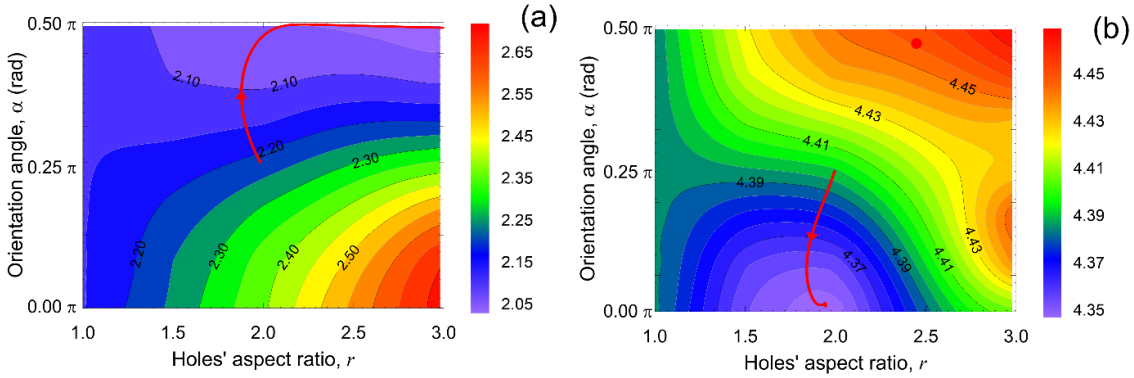

Figure 2-12. OF contours of the metamaterial plate with fixed porosity p containing a regular pattern of identical holes. Combined thermo-mechanical response OF $f(\beta)$ for different values of the coefficients a_1 and a_2: $a_1 = a_2 = 1$ (a), $a_1 = 1, a_2 = 4$ (b). The red line depicts the evolution of the design variables until the best configuration is attained [16]. Reproduced under the terms of © 2022 Elsevier Ltd.

As shown in Figure 2-12, the combination of thermal and mechanical responses significantly influences the OF. Specifically, when larger combination coefficients are applied to the thermal response compared to the mechanical one, the optimized hole configuration differs notably. For instance, when the thermal response is weighted more heavily than the mechanical one, the optimal configuration is $(r \cong 2, \alpha = 0)$ while for equal combination coefficients the configuration changes to $(r \cong 3, \alpha = \pi/2)$.

Figure 2-13 presents the numerical, experimental, and theoretical results for porous plates with randomly varying geometrical parameters, including hole positioning, orientation, and aspect ratio, Figure 2-10.

For the sake of comparison, results are also shown for two groups of plates with a fixed hole orientation $(\alpha = 0, \pi/2)$. The weight factor $W = 5$, determined through best fitting for the case $r = 1$, is considered across all the considered cases. As expected, the metaplates with fully random parameters exhibit thermal behavior intermediate to those with fixed orientations $(\alpha = 0, \pi/2)$.

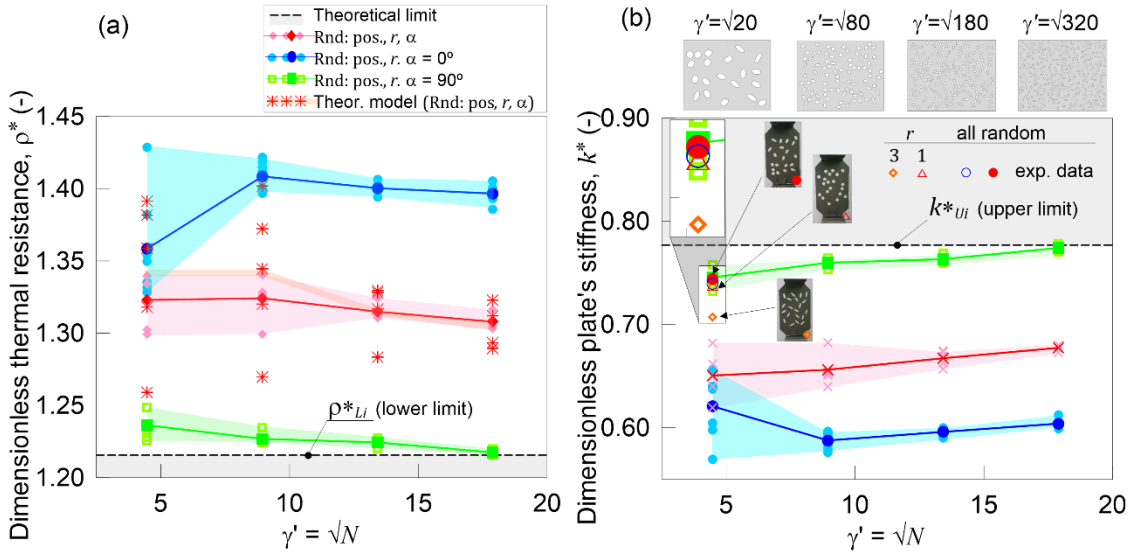

Figure 2-13. Dimensionless thermal resistance (a) and mechanical stiffness (b) vs conventional plate-unit cell ratio γ' for plates with random holes positioning, orientation and aspect ratio. Several cases related to the same γ' value have been considered (the continuous lines indicate the average value). Two cases with fixed orientation angle values are also reported while aspect ratio and position are randomized. The lower and upper limits of the relative thermal resistance (ρ^*_{Ui}) and mechanical stiffness (k^*_{Ui}), respectively, evaluated according to Eq. (2-11), are also indicated [16]. Reproduced under the terms of © 2022 Elsevier Ltd.

2.5 Conclusions

Multi-morphology TPMS scaffolds, with a focus on the impact of transition zone length in Gyroid and Diamond structures, using both numerical simulations and experimental tests, have been considered in the first part of this chapter. Scaffolds with varying transition zones were designed and fabricated via FDM AM, and single-cell structures like Diamond, I-WP, and Gyroid were used as references. Results show that Diamond scaffolds exhibited higher stiffness in compression tests, likely due to the porosity differences, as the Diamond structure is stretching-dominated, and its behavior is strongly influenced by porosity.

µCT analysis revealed imperfections inherent to the FDM process, such as geometrical inaccuracies, which impact the printed scaffold's structural quality. These imperfections highlight the importance of real geometry-based analyses. µCT imaging was instrumental in capturing deviations from the nominal design and understanding their effects on scaffold behavior. The FEM analysis, when applied to µCT-based geometries, provided more accurate predictions of scaffold performance compared to analyses performed using nominal geometries. This approach proved to be particularly effective in capturing the behavior of scaffolds under complex loading conditions.

The thermal and mechanical responses of metaplates considering the role of void geometry, orientation, and arrangement have also been considered in the present chapter. The results showed that elliptical voids with tailored aspect ratios and orientations can effectively balance thermal and mechanical performance, providing insight into how geometric parameters influence the overall behavior of porous metaplates.

2.6 Advancing TPMS and metaplate design

While the TPMS and metaplate studies offered valuable insights on how geometric features affect performance, they were inherently limited by their reliance on predefined shapes, topologies, and configurations. This restricts the ability to explore unconventional designs that might lead to superior performance. Furthermore, although parametric studies can optimize specific configurations, they do not provide a systematic framework for discovering novel material layouts that maximize efficiency, i.e., they lack to converge to the so-called global minimum considering the engineering limitations. These topological limitations underscore the need for more advanced computational methods capable of transcending the constraints of fixed geometries and/or topologies. Regardless of the beauty and the progression of continuum TO, discrete TO is still an active field of research because of its simplicity [95].

Following the mentioned limitation of parametric optimization techniques, the next chapter introduces mathematical-based TO as a promising approach to address these limitations. This technique allows for the exploration of material distributions unconstrained by predefined geometries, offering a more flexible and comprehensive design methodology. By leveraging the insights from TPMS and metaplate studies, TO can provide solutions that balance competing demands for thermal and mechanical performance, while uncovering innovative solutions for advanced designs.

The transition from porous and metamaterials to a continuum TO, represents an important step in advancing the functional design of structures and devices, enabling researchers to move beyond parametric studies to fully exploit the potential of porous and cellular structures. This progression not only enhances the design process but also broadens the scope of applications for functional materials and designs in engineering and biomedical fields. Through this systematic exploration, the goal is to create materials that excel in both performance and adaptability, meeting the demands of increasingly complex engineering challenges.

Chapter 3

TOPOLOGY OPTIMIZATION: A REVIEW ON APPROACHES AND NUMERICAL METHODS

3.1 Introduction

Optimization is a fundamental concept in engineering design, involving the systematic determination of the best design variables within a defined set, subjected to some constraints and objectives. At its core, optimization seeks to maximize performance metrics such as lifetime, efficiency, strength, or sustainability while minimizing undesirable factors such as cost and time, material usage, or energy consumption. The goal of optimization is simply to find the variables values that minimize the objectives. Modern computational tools have significantly advanced optimization methodologies, making it a central element in engineering design [96].

The general mathematical formulation of an optimization problem can be stated as follows:

$$\text{Find:} \quad \min_{x \epsilon R^n} f(\boldsymbol{x}) \qquad \text{Subjected to:} \quad \begin{cases} c_i(\boldsymbol{x}) = 0, & i \in \mathcal{E}, \\ c_i(\boldsymbol{x}) \leq 0, & i \in \mathcal{L} \end{cases} \tag{3-1}$$

Where c_i is the constraint function, $\mathcal{E}$ and $\mathcal{L}$ are the sets for equality and inequality constraints, respectively, $f(\boldsymbol{x})$ is the Objective Function (OF), and $\boldsymbol{x} \epsilon R^n$ is the vector of the design variables of the optimization problem [96].

Depending on the physical problem and the constraints adopted in structural optimization, each of the above terms takes a specific form. The process of defining and calculating these terms is referred to as *modeling*. A critical aspect of structural optimization methods is the *sensitivity analysis*, which involves determining how the OF and constraints change due to variations in the design variables; in other words, it corresponds to evaluating the solution's sensitivity to the chosen model [96].

Topology optimization (TO) is a computational design methodology that seeks to determine the optimal material distribution within a given design domain, to achieve predefined performance objectives under some equality or inequality constraints. Unlike traditional shape and size optimization, which modify predefined geometries, TO allows for the creation of entirely new designs by adding, removing, or redistributing material within the so-called design domain, see Figure 3-1. This flexibility enables designers to explore innovative and efficient structures that might not be achievable using conventional methods. Rooted in the principles of mathematical optimization and structural mechanics, TO has become an indispensable tool across diverse applications, from aerospace [97] and automotive engineering to biomedical devices and civil infrastructure in engineering to mention a few, facilitating lightweight, cost-effective, and high-performance solutions. Its capability to be seamlessly integrated with advanced

manufacturing technologies, such as additive manufacturing, has further expanded its potential for generating highly complex and functionally optimized designs.

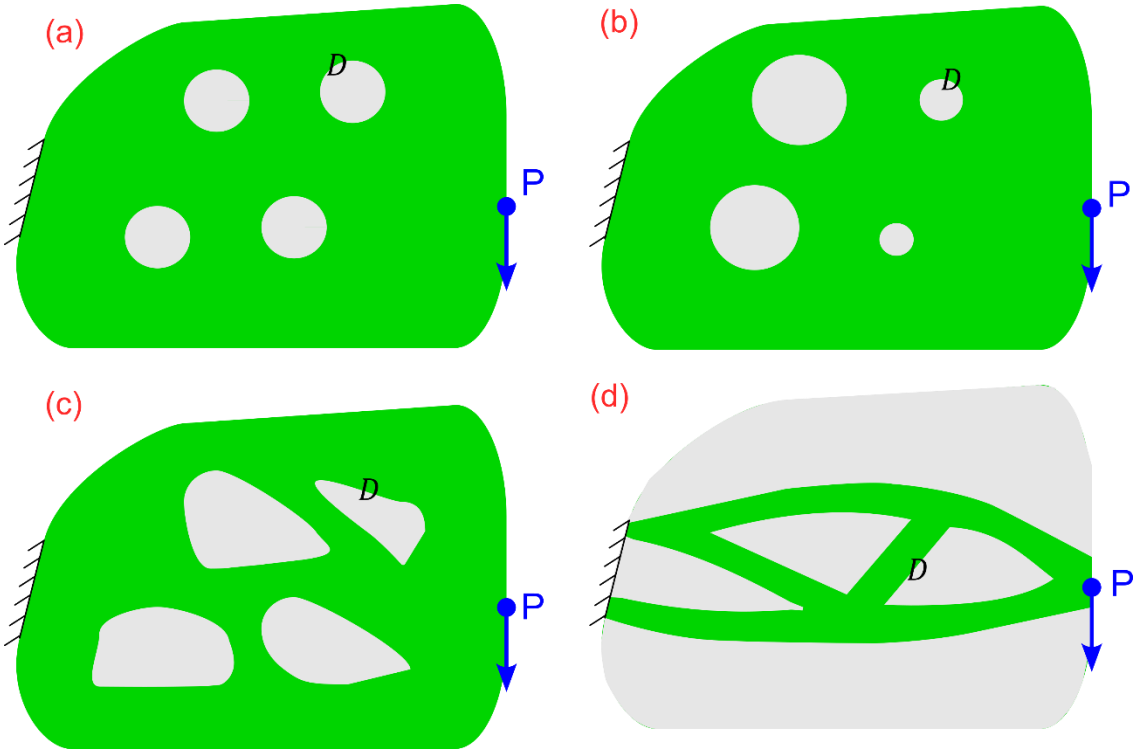

Figure 3-1. The design domain, D, subjected to load P illustrates qualitative outcomes considering an unconstrained optimization. Starting from an arbitrary initial domain (a), size optimization where only the size of each predefine hole can change (b), shape optimization (c), and TO (d) are applied. The green area denotes the material, whereas the grey area represents voids.

Thanks to advancements in numerical methods, optimization is commonly performed by iteratively adding or removing material from a predefined design space while minimizing the OF of the problem, such as the structural compliance of the system [98]. Consequently, this approach not only achieves significant weight reduction by eliminating useless material regions, but also enhances the structure's performance in relation to the physical problem being addressed [99]. The achievable improvements are nowadays vital in various applications, including aerospace [100], automotive [101, 102], and civil engineering [103], as well as biomedical engineering [104], to mention the main ones.

Efficient solutions and algorithms have been developed by combining TO with advanced computational frameworks and tools, such as machine learning [105-107], quantum computing [108], and parallel computing [109].

3.2 Structural and topology optimization

Structural optimization is a fascinating area of computer-aided engineering, whose roots trace back centuries ago to Galileo Galilei's efforts to determine the optimal design of structural elements [95]. The primary goal of structural optimization is to design the structure's geometry – encompassing its size, shape, and topology – to improve durability and performance by addressing one or more physical performance, such as controlling the deformation [110], stress concentration [111], heat transfer [77, 112-118], eigenfrequencies [119], electromagnetics [120], and biological functionality [121], among others [43, 122-136].

While size and shape optimization modify only the dimensions and/or reshape the initial domain, TO enables the creation of more intricate designs by introducing or merging void regions as needed. This capability has established TO as a robust tool for developing complex, high-performance structures tailored to specific desired responses. When combined with advanced manufacturing methods such as additive manufacturing, TO facilitates the production of realistic optimized components [43, 127, 137, 138]. The following sections present a concise overview on TO.

In Michel's foundation work, structural optimization was applied to derive the exact solution of truss structures accomplishing the minimum weight requirement [132, 139]. Numerical algorithms designed to converge to the optimal topology in continuum TO can be broadly categorized into three main approaches: 1) Solid Isotropic Material with Penalization (SIMP) [17, 133, 140], 2) Evolutionary Structural Optimization (ESO) [141, 142], and 3) Level-Set-based (LS) methods [143-149]. Additionally, other methods, such as topological derivatives (bubble method) [150], phase field [151], and bi-directional evolutionary structural optimization (BESO) [117, 141, 152], have also been developed. Notably, the LS method (LSM) and topological derivatives rely on shape derivatives to achieve the optimal design layout, whereas the other methods typically employ simple element- or nodal-based design variables. Due to this distinction, the LSM and topological derivatives are particularly effective for obtaining smooth boundaries and intricate topological features. However, in other approaches, similar accuracy can be achieved through post-processing at the expense of using finer discretized domains. Nevertheless, LSM and SIMP can be related each other to give effective and feasible optimal solutions through the CutFEM method [153].

In density-based TO methods, the problem is typically formulated with the design variable representing material density, whereas in Level-Set-based methods the design variable corresponds to the LS value. Based on these concepts, the following sections provide a concise overview of the predominant TO approaches.

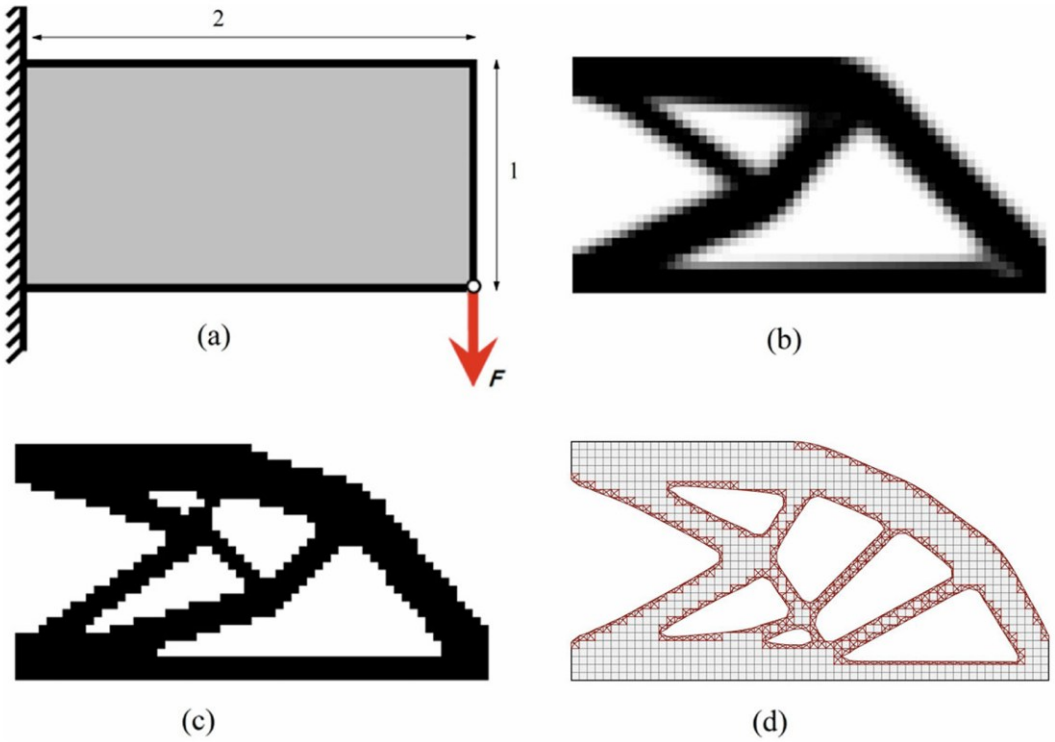

Figure 3-2. Comparison of different TO methods. The design domain with its dimensions (a). The optimal topology obtained using SIMP (b), the corresponding final topology using ESO (c), and the final topology using an implicit boundary representation (d). The figure was obtained directly from [154]. Reproduced under CC BY license. © 2018 The Author(s).

3.3 Solid isotropic material with penalization

Among the existing TO methods, the SIMP approach is the most widely recognized and straightforward to implement [155-157]. In the SIMP approach, the elastic modulus of each element is defined as:

$$E(x_i) = x_i^p E_0 \tag{3-2}$$

where p is the penalization factor to enforce x_i to take either '0' or '1' values, while E_0 is the elastic modulus of the solid material. Therefore, using Eq. (3-2) the element stiffness matrix can be identified as:

$$\boldsymbol{k}_i = E(x_i)\,\boldsymbol{k}^* = x_i^p E_0\,\boldsymbol{k}^* = x_i^p\,\boldsymbol{k}_0 \tag{3-3}$$

In the above equation, $\boldsymbol{k}^*$ is the element stiffness matrix divided by the elastic modulus, so $\boldsymbol{k}_0$ is the element stiffness matrix of the solid material. The OF for a compliance minimization problem is defined in the form of:

$$\begin{aligned} & f(\boldsymbol{x}) = \boldsymbol{U}^T\boldsymbol{K}\boldsymbol{U} = \textstyle\sum_{i=1}^{N} x_i^p\,\boldsymbol{u}_i^T\boldsymbol{k}_0\,\boldsymbol{u}_i \\ \text{fulfilling:} \quad & \boldsymbol{K}\boldsymbol{U} = \boldsymbol{F} \end{aligned} \tag{3-4}$$

$$\text{such that:} \qquad \sum_1^N V_i x_i - V^* = 0 \quad \varepsilon \le x_i \le 1$$

where $f(\boldsymbol{x})$ is the compliance, here assumed to be the OF to be minimized, $\boldsymbol{K}$, $\boldsymbol{U}$, and $\boldsymbol{F}$ are the global stiffness matrix, the global displacements vector, and the global force vector, respectively. The scalar V^* represents the prescribed volume, and $\sum_1^N V_i x_i - V^*$ is equivalent to the equality constraint $c_i(x)$ in Eq. (3-1).

In this method, the density of each element is updated based on the finite element (FE) results as well as the OF, with the density values constrained to be 0 (void) or 1 (solid) to achieve the optimal topology. While this simplification is advantageous, it introduces challenges, particularly due to checkerboard patterns that can emerge at boundaries [158]. Over the years, various techniques have been developed to address this issue and to improve the SIMP method. For instance, Rossow and Taylor proposed the first two-dimensional FE-based TO method [159]. However, since their approach did not incorporate penalization, the resulting topologies included many gray regions, which reduced the manufacturability of the optimal structures [132]. To address other challenges, such as corner contacts, techniques like filtering methods [140], perimeter constraints [160], and checkerboard-preventing constraints [161], have been introduced. Thanks to its easy implementation within the FEM, this approach has become a cornerstone in commercial software applications according to Figure 3-3, including SolidWorks, ABAQUS, and Siemens NX, among others [155, 162].

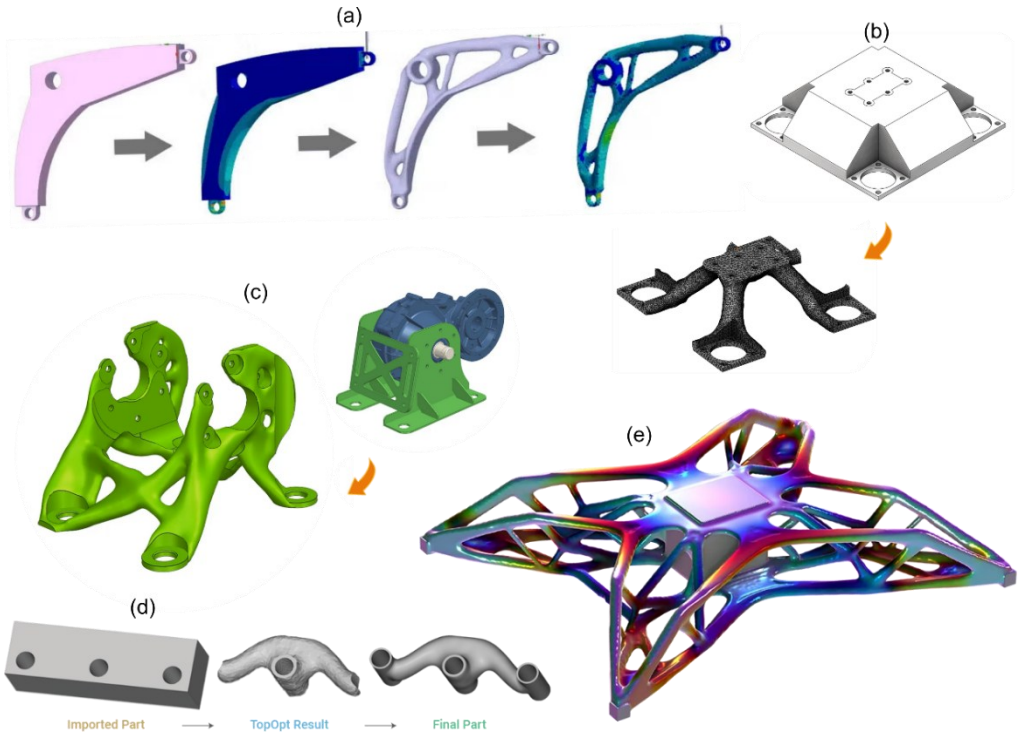

Figure 3-3. Some TO examples extracted from commercial software. Taken from the websites of Ansys (a), SOLIDWORKS (b), NX (c), nTop (d), and COMSOL Multiphysics (e) [163-167].

3.4 Evolutionary structural optimization

In ESO methods, firstly introduced by Xie and Steven, a rejection criterion typically based on von Mises (VM) stress is assessed for each element using FE results. The elements having the (usually normalized) VM stress lower than a specified Rejection Ratio (RR) are removed, while those with higher values are retained [132, 142]. In other terms, the method aims to gradually eliminate finite elements that are inefficient in carrying the applied loads. The sensitivity analysis is carried out by deactivating elements with normalized VM stress below the RR, which is initially set to $RR_1 = 0.01$, as described by the following inequality:

$$\frac{\sigma_i}{\sigma_{max}} < RR_i \tag{3-5}$$

where σ_i and σ_{max} represent the VM stress of the $i-th$ element and its corresponding maximum value in the entire structure at a specific time, respectively. RR_i is the rejection ratio, which is incremented by a small Evolutionary Rate (ER) when Eq. (3-5) reaches a steady-state situation. ER is adjusted based on the complexity of the structure or the desired level of topological detail [142].

3.4.1 Bi-directional evolutionary structural optimization

To address issues of long computational time and to avoid finding local minima, a method known as bi-directional ESO was introduced by Querin and Steven [141, 152]. In this approach, the algorithm not only removes elements, but also adds new ones when the normalized VM stress criterion exceeds a certain threshold. In this context, in addition to Eq. (3-5), the following update scheme enables the activation of elements:

$$\frac{\sigma_i}{\sigma_{max}} > IR_i \tag{3-6}$$

where IR_i is the Inclusion Ratio. The sensitivity analysis, which relates the density of each element to the OF, follows the SIMP strategy as indicated in Eq. (3-2).

3.5 Multi-scale TO

The scale of optimization is another concept used to categorize TO approaches, where algorithms aim to determine the optimal material distribution from either a microstructural or macrostructural perspective [95]. The microstructural approach is commonly known as the homogenization method [168-170]. Key works in this area include Optimal Microstructure with Penalization (OMP) [171] and Near-Optimal Microstructure (NOM) [172]. Optimization complexity can

also be increased by combining different scales, leading to Multi-Scale TO (MSTO).

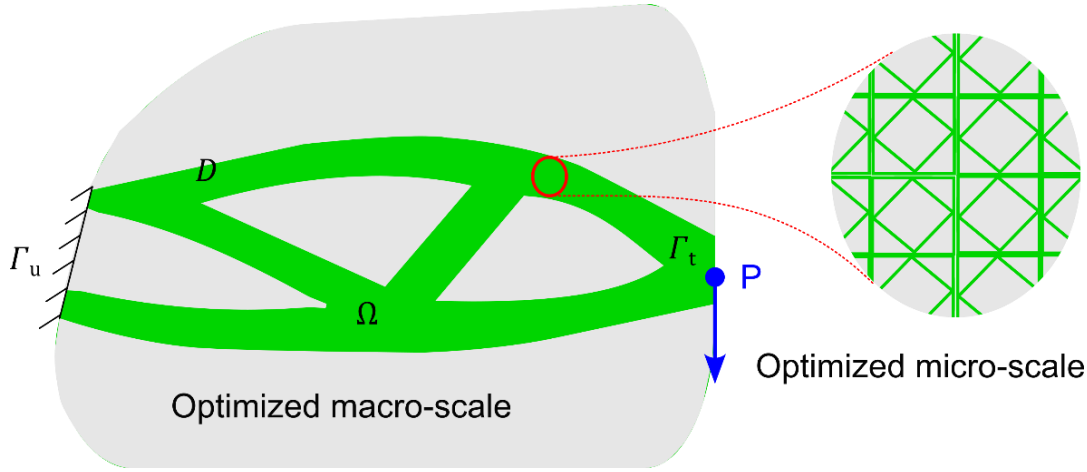

Figure 3-4. A qualitative schematic of a MSTO approach.

In MSTO, differently by single-scale TO, the geometric layout is optimized across more than one length scale. Interestingly, MSTO was used before mono-scale TO [170], but due to manufacturing challenges, researchers initially preferred mono-scale TO [173]. However, with the advent of advanced manufacturing techniques, such as additive manufacturing, the focus has shifted back to MSTO. This method primarily includes three approaches: homogenization-based TO, density-based methods (such as SIMP or the power-law approach) [174-176], and inverse homogenization methods [177]. In the latter, the microstructure of the design domain is adjusted to achieve specific physical performance at the macro-scale [173]. For example, to obtain materials with a global negative Poisson's ratio, a subset of mechanical metamaterials [16, 56, 87, 178] can be designed such that their optimized unit cells exhibit a negative Poisson's ratio, distinct from the regular unit cells used in lattice structures [179]. Additionally, this inverse TO method can be applied to tune other physical properties, such as thermal expansion, thermal and electrical conductivities, fluid permeability, and photonic behavior.

To optimize multi-scale materials, either a global or a local approach can be employed [173]. MSTO can be achieved through local control methods, such as pattern repetition or local volume constraints [173]. The pattern repetition approach involves replicating the same optimized unit cell in the required directions [180], while the local volume constraint method modifies each local geometry by introducing additional constraints, such as local porosity and the local radius of the neighborhood [173]. The local volume constraint approach has been applied not only for optimizing the mechanical compliance of structures but also for optimizing other physical problems, such as heat conduction [181], acoustics [182], and biomechanics [121]. Interestingly, Gao et al. combined the

variable thickness sheet method with PLSM to optimize a porous material at both macro and micro scales, respectively [183].

3.6 Level-set method and its application in TO

In this subsection, the general principles of the LS approach and its application for solving TO problems are reviewed. Specifically, the strategies for describing the design and physical domains, and evolving the LS equation aimed at minimizing the OF, are presented.

LSM is an efficient and versatile computational approach for tracking domain boundaries of arbitrary shapes [184-187]. Thanks to these advantages, it has become an emerging and widely adopted computational technique for the solution of a variety of problems characterized by propagating interfaces and multiple materials [184, 188]. As a representative example, in Figure 3-5 a 3D bridge is considered and topologically optimized using LSM.

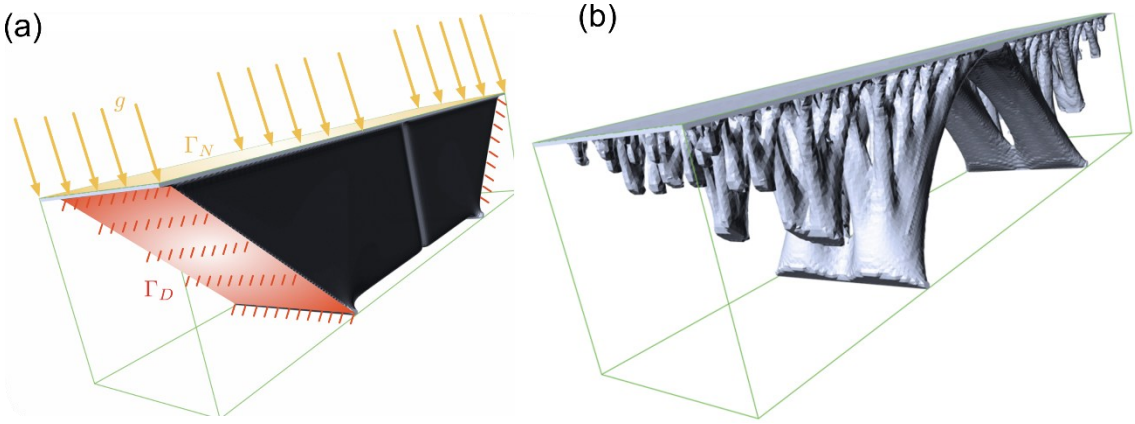

Figure 3-5. Topology optimization of a 3D bridge. The initial configuration with prescribed BCs (a), and the final configuration after 200 iterations (b) [122].

Applications of LSMs range from wave propagation [189], multi-phase motion of solids [190], liquids and grains [191], image processing [192], and computing minimal surfaces [193]. When implemented within a finite element (FE) framework, LSM smoothly describes boundaries and is computationally robust [122, 136, 194-197]. A key component of the method is the introduction of the topological derivative, which accounts for the effect on the OF of void nucleation within the material domain [150, 198]. Regarding educational implementations of the LS method in TO, several works are available in the literature [147, 153, 155, 199-205].

The method, introduced by Osher and Sethian [184], later extended by Osher and Santosa [185], combines LSM, the variational level set calculus, and the projected gradient method. Its flexibility allows for smooth, time-dependent

boundaries and topological changes, making it suitable for a wide range of TO problems [143, 206]. Additionally, educational implementations include Challis' *129-line MATLAB code*, which enables hole nucleation in design domains [147]. Allaire et al. provided numerical approaches integrating LSM into TO frameworks [144, 207, 208], while other significant contributions have explored connecting material derivatives to velocity fields derived from the Hamilton-Jacobi equation [209].

To simplify its implementation, Parameterized LSM (PLSM) uses Radial Basis Functions (RBFs) for parameterization [199, 210, 211]. Recent developments address multi-load problems [212], improve computational speed using compact supported RBFs [213], and propose reaction-diffusion equations as alternatives to the Hamilton-Jacobi equation [201, 214, 215]. Wang et al. incorporated B-spline functions for implicit boundary definitions and solved reaction-diffusion equations [216]. Dunning and Kim's algorithm, which uses sequential linear programming to address multi-constraint problems [217], is also one of the leading works in LSM.

3.6.1 Level-set applications in different fields

LSM has been applied across diverse fields, highlighting its versatility. Bujny et al. optimized the crashworthiness of lattice structures [218] and implemented machine learning algorithms for the same problem [125]. Wu et al. used LSM for optimizing auxetic metamaterials under hybrid uncertainties [219]. Using parameterized LSM, multi-scale TO has been employed to solve inverse problems, such as identifying microstructures based on required global behavior [211]. For load-carrying heat exchangers and battery packs in electric vehicles, LSM has been used to optimize layouts for minimal compliance and maximal heat dissipation [116, 220, 221]. In the context of additive manufacturing, LSM has enabled the design of lightweight structures with high stiffness [43]. Salazar de Troya et al. used LSM to define two-phase fluid boundaries, optimizing heat exchange and pressure drop in heat exchangers [222]. Luo et al. optimized thermal cloaks, a category of thermal metamaterials [223], while Ogawa and Yamada addressed transient thermomechanical problems [129].

Despite its strengths, the standard LS method in structural optimization often results in ill-posed problems [123]. This issue arises due to its reliance on the Hamilton-Jacobi PDE [209]. To address this drawback, PLSM has been introduced, where the LS function is parameterized using techniques such as RBFs or Non-Uniform Rational B-Splines (NURBS) [199, 210-212]. This approach simplifies the optimization process by converting the PDE into an ordinary differential equation, enhancing numerical stability and ease of implementation. One notable advancement in PLSM is Li et al.'s use of compactly

supported RBFs to improve computational efficiency [137]. Methods incorporating the extended finite element method (XFEM) [118] or NURBS-based parameterizations [134] have also shown promise in handling complex geometries and material nonlinearities.

3.7 Multi-objective and multidisciplinary TO

Modern engineering often requires balancing multiple, conflicting objectives across disciplines, necessitating Multi-Disciplinary Optimization (MDO). MDO integrates criteria from distinct physical phenomena, such as mechanical, thermal, and aerodynamic performance, into a unified framework, enabling systematic trade-off management. This is particularly crucial in industries like aerospace and biomedical engineering, where interconnected design criteria drive success.

In contrast, multi-objective TO focuses on optimizing conflicting goals, such as stiffness and weight, often requiring strategies to combine OFs. For instance, mechanical compliance and heat conduction can be merged into a single OF, but introducing conflicting objectives typically transforms the problem into a nonconvex one [181].

In numerical optimization, problems are classified as convex or nonconvex based on their mathematical properties. Convex problems have a well-defined global minimum, with any local minimum also being the global minimum, making them computationally more straightforward and predictable. Conversely, nonconvex problems, which are common in TO, involve multiple local minima, making it challenging to identify the global minimum. Nonconvexity often arises due to complex, nonlinear design spaces or practical considerations, such as multimaterial configurations, nonlinear material behavior, or interactions between multiple physical phenomena like thermo-mechanical optimization [224].

Conflicting objectives, such as minimizing weight while maximizing stiffness or natural frequencies, frequently lead to nonconvex formulations. To be more specific, in most real-world applications TO problems are inherently nonconvex. Addressing these challenges often requires advanced strategies. Gradient-based optimization combined with regularization can help smoothing the problem landscape, allowing the algorithm to escape local minima [225]. Relaxation techniques, such as decomposing the nonconvex problem into multiple convex subproblems, also simplify the solution process [226].

Chapter 4

TOPOLOGY OPTIMIZATION THROUGH THE LEVEL SET METHOD

4.1 Introduction to Level-Set methods

Level-Set Methods (LSMs) provide a mathematical framework for implicitly representing and evolving boundaries within a higher-dimensional scalar field [184]. In numerical computations, boundaries definition is fundamental for precisely describing the geometry of the objects domain in problems such as topology optimization (TO) [18], Finite Element Analysis (FEM) [227, 228], and image processing [192]. These boundaries can be represented using explicit or implicit techniques [136]. Explicit methods, such as boundary representation, define boundaries through vertices, edges, and faces. In explicit methods, the boundary can be also described directly using the density of each element, see for example [17, 95]. In these methods, the void space is determined if the density falls within a specific range of the lowest possible density representing regions where no material exists.

Differently from explicit methods, in implicit methods the boundary is parametrized using another scalar filed, allowing to handle effectively the topological changes [136]. The material interface between phases or void regions of the design space is defined using iso-contours, typically the zero level of a scalar field (the LS Function (LSF)), enabling to obtain high flexibility in evolving and manipulating complex topologies [143-145, 207, 229, 230].

In this chapter, the general aspects of the LS approach for TO problems will be discussed. To be more specific, the physical domain description, the evolution of the interface, the LS interpolation, the mechanical compliance minimization, and thermal conduction optimization will be presented. In the final sections, the methodology for handling the constraint using Lagrange multipliers method as well as some remarks about the use of immersed methods is presented.

4.2 Definition of interfaces using LSFs

The implicit representation of the material boundary Γ within the design domain D of the considered problem is obtained through the level set (LS) of a Lipschitz-continuous scalar function $\varphi(\boldsymbol{x}(t))$:

$$\Gamma(t) = \{\boldsymbol{x}(t): \varphi(\boldsymbol{x}(t)) = C\} \tag{4-1}$$

where $\boldsymbol{x} \in \mathbb{R}^d$ represents the vector representing a generic point within a domain of dimension $d \in \{2,3\}$, while C denotes the iso-value of the function $\varphi(\boldsymbol{x}(t))$ that defines the current boundary Γ. This boundary has a geometrical dimension $d - 1$ and lies within the physical domain Ω. Additionally, the void region is denoted as $D \backslash \Omega$, with $D(\supseteq \Omega)$, representing the design domain of the problem. The boundary Γ is assumed to evolve over a fictitious time scale as the boundary changes.

In many cases, the classical LS-based boundary representation is based on the zero iso-value of the LSF, i.e. C =0; this assumption will be followed in this study. When the zero iso-value of $\boldsymbol{\varphi(x)}$ is determined, the state of the material at a generic point $\boldsymbol{x}$ belonging to the physical domain Ω is identified using the following conditions Figure 4-1:

$$\begin{aligned} \boldsymbol{x} &\in \Omega \quad && \text{if } \varphi\big(\boldsymbol{x}(t)\big) > 0 \\ \boldsymbol{x} &\in D\backslash\Omega \quad && \text{if } \varphi\big(\boldsymbol{x}(t)\big) < 0 \\ \boldsymbol{x} &\in \Gamma = \partial\Omega \quad && \text{if } \varphi\big(\boldsymbol{x}(t)\big) = 0 \end{aligned} \tag{4-2}$$

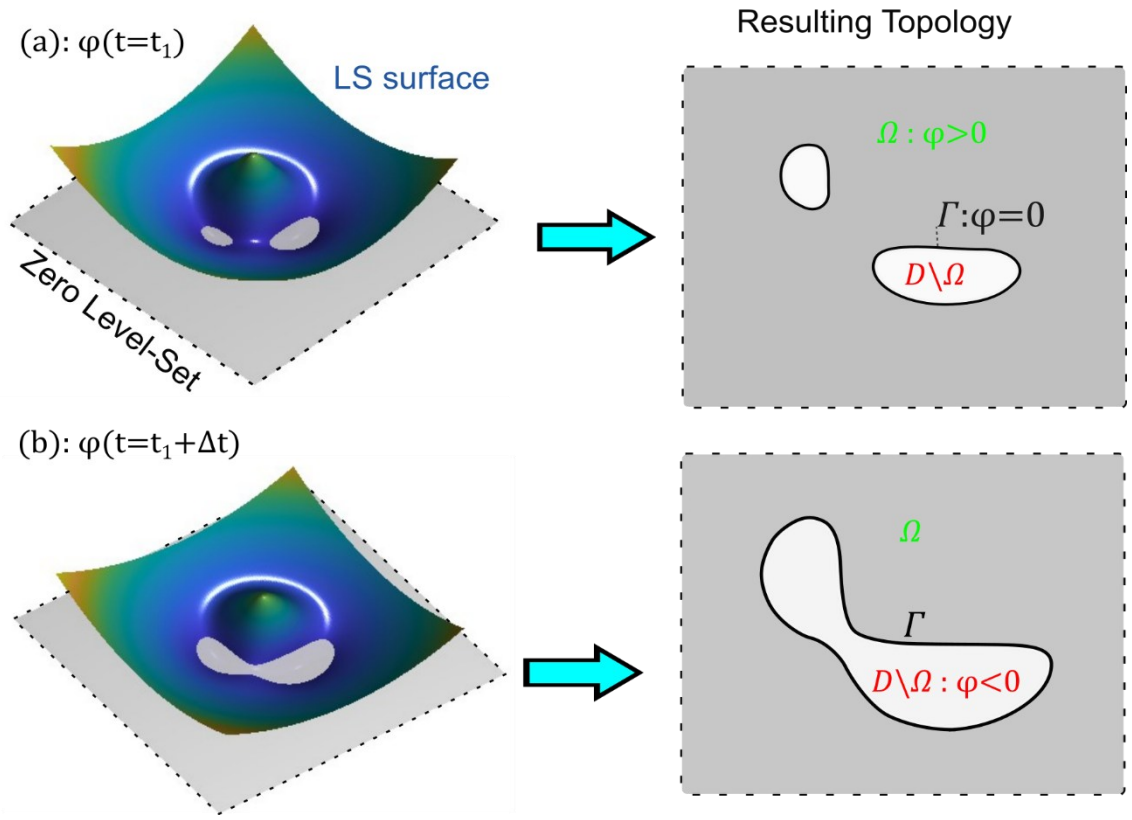

Figure 4-1. Diagram illustrating the LS surface and the associated boundaries Γ. The physical domain Ω is defined by the level set $\boldsymbol{\varphi(x)} = 0$ at $t = t_1$(a) and $t = t_1 + \Delta t$ (b), showing the updated material configuration after evolving the boundaries by a fictitious time increment. The material is assumed to exist at any point $\boldsymbol{x}$ where $\boldsymbol{\varphi(x)} > 0$.

Based on the definition of the actual physical domain given in Eq.(4-2), the physical properties (such as the elastic modulus, the thermal conductivity, etc.) can be determined by applying the Ersatz material model by introducing the Heaviside (step function) $H(\boldsymbol{\varphi})$ at an arbitrary location $\boldsymbol{x}$ within the design space; $H(\boldsymbol{\varphi})$ is defined by the following step function [207, 231]:

$$H\big(\boldsymbol{\varphi(x,t)}\big) = \begin{cases} 1 & \text{if } \boldsymbol{\varphi(x,t)} \geq 0 \quad \text{(material)} \\ 0 & \text{if } \boldsymbol{\varphi(x,t)} < 0 \quad \text{(void)} \end{cases} \tag{4-3}$$

This approach allows integrating any function $f(\boldsymbol{x})$ over the actual material domain Ω by performing direct integration over the design domain D, without the need to know the exact position of the current boundary:

$$\int_{\Omega} f(\boldsymbol{x})\ dV = \int_{D} f(\boldsymbol{x})\, H\big(\varphi(\boldsymbol{x})\big)\, dV \tag{4-4}$$

As a matter of fact, when $f(\boldsymbol{x}) = 1$ Eq.(4-4) provides the volume (in 3D settings) or the area (in 2D settings) of the physical domain:

$$V(\varphi) = \int_{D} H\big(\varphi(\boldsymbol{x})\big)\, dV = \int_{\Omega} dV\,, \quad A(\varphi) = \int_{D} H\big(\varphi(\boldsymbol{x})\big)\, dA = \int_{\Omega} dA \tag{4-5}$$

4.3 Evolution of the LS surface

Following Eq. (4-1), the LS method identifies the physical boundary through the constant value of the LSF. This means that $\varphi(\boldsymbol{x}, \mathrm{t})$ does not change along the boundary, even if the boundary evolves over time. Mathematically this condition is provided by:

$$\frac{d\varphi}{dt} = 0 \tag{4-6}$$

Harnessing the definition of the material derivative of a function we have:

$$\frac{d\varphi}{dt} = \frac{\partial \varphi}{\partial t} + \nabla_{\boldsymbol{x}}\varphi(\boldsymbol{x}, t)\, \dot{\boldsymbol{x}} = 0 \tag{4-7}$$

This is the key equation that describes the evolution of the LSF, ensuring that the boundary Γ consistently evolves based on the LSF and correspondingly does the Objective Function(s) (OF(s)).

4.3.1 Shape derivative and normal velocity

In LSM, the velocity vector $\boldsymbol{v}(\boldsymbol{x}, t)$ is decomposed into the normal and tangential components to the boundary. Only the normal velocity is effective in defining the boundary evolution, and it is typically expressed as follows:

$$\boldsymbol{v}(\boldsymbol{x}, t) = -v_n(\boldsymbol{x}, t)\frac{\nabla_{\boldsymbol{x}}\varphi}{|\nabla_{\boldsymbol{x}}\varphi|} \tag{4-8}$$

where $v_n(\boldsymbol{x}, t)$ is the normal velocity to the LS surface, while $\frac{\nabla_{\boldsymbol{x}}\varphi}{|\nabla_{\boldsymbol{x}}\varphi|}$ is the unit normal vector to the LS surface at a generic location $\boldsymbol{x}$. Substituting the last equation into Eq. (4-7), the material derivative can be found to be:

$$\frac{d\varphi}{dt} = \frac{\partial \varphi}{\partial t} - v_n(\boldsymbol{x}, t)|\nabla_{\boldsymbol{x}}\varphi(\boldsymbol{x}, t)| = 0 \tag{4-9}$$

The latter relationship represents the Hamilton-Jacobi (H-J) equation which constitutes the foundation for the LS evolution. This equation governs the update of the LS function which can be expressed as:

$$\varphi_t = \varphi_0 + \int_0^t v_n |\nabla_x \varphi| dt \tag{4-10}$$

where φ_0 is the LS function at $t = 0$, corresponding to the initial configuration of the physical domain Ω_0. After discretizing the time axis in steps of finite size Δt, the above equation enables obtaining the updated LS function starting from the one known at the previous step:

$$\varphi_{i+1} = \varphi_i + \Delta t |\nabla_x \varphi| v_n \tag{4-11}$$

It is worth mentioning that the time step size is fundamental for the convergence in LS-based optimization approaches; being the solution of Eq. (4-11) is explicit in time, the time step must obey the Courant-Friedrichs-Lewy (CFL) condition [231]. This condition requires that the largest time step cannot overcome the minimum grid spacing to the velocity magnitude ratio, i.e. $\Delta t \leq \frac{ds}{max|v_n(x)|}$, being ds the minimum grid size used for discretizing the LSF.

Finally, it is fundamental to underline that in the LS method, normal velocity is assumed to be driven by the OF adopted for the optimization problem in turn.

4.4 Radial basis function interpolation and LS function initialization

The LSF plays a pivotal role in structural TO since it represents the material domain boundaries implicitly. It is convenient to express the LS function in a parameterized form based on the LS values assumed at specific points. In particular, a local interpolation approach is typically adopted for such a purpose [232].

4.4.1 Initialization of the LSF

In order to perform the TO of a physical problem, the LSF $\varphi(\boldsymbol{x}, t)$ requires to be initialized over the design domain D. A typical initialization strategy involves setting $\varphi_0 = \varphi(\boldsymbol{x}, t = 0)$ as the Signed Distance (SD) from the initial material boundary:

$$\varphi_0 = \varphi(\boldsymbol{x}, t = 0) = \begin{cases} d(x), & \text{if } \varphi(\boldsymbol{x}, t) \geq 0 \quad \text{(material)} \\ -d(x), & \text{if } \varphi(\boldsymbol{x}, t) < 0 \quad \text{(void)} \end{cases} \tag{4-12}$$

Here, $d(x)$ is the Euclidean distance from a generic point $\boldsymbol{x}$ to the nearest physical boundary. The initialization ensures that the LSF is smooth and satisfies the unit norm condition $|\nabla \varphi(\boldsymbol{x}, 0)| = 1$, making it suitable for numerical methods. Further, the SD formulation ensures a well-defined interface at the beginning of the optimization procedure (Figure 4-2).

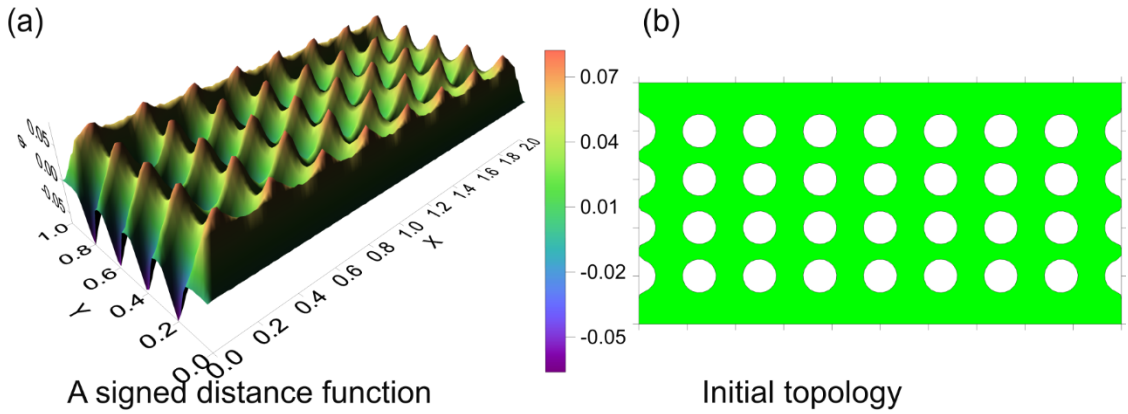

Figure 4-2. An initial rectangular design domain containing regularly arranged holes. SD function defining the initial LS function (a), and its corresponding topology in 2D (b) are shown.

4.4.2 Radial basis function parameterization

In the present section, the Radial Basis Function (RBF)-based parametrization of the LSF is introduced. Once initialized, the LSF evolves during the optimization process. Being known at discrete points corresponding to the LS grid knots, the LSF must be interpolated over the entire problem domain in order to calculate all the related quantities, such as the LS gradient, etc. To this end, a suitable local interpolation can be introduced; the parameterized LS function is defined as follows:

$$\varphi(\boldsymbol{x},t) = w_i(t)\, R_i(\|\boldsymbol{x}-\boldsymbol{x}_i\|), \quad R_i = \sqrt{\left|\left|\boldsymbol{x}-\boldsymbol{x}_i\right|\right|^2 + c^2} \tag{4-13}$$

where R_i represents the Euclidean radial distance between the generic point $\boldsymbol{x} = (x_1, x_2)$ and the grid node $\boldsymbol{x}_i = (x_{i1}, x_{i2})$, while c is a small positive constant. The time-dependent weights $w_i(t)$ correspond to the LSF values at the grid nodes $\boldsymbol{x}_i$ and are the key parameters to be determined for the interpolation.

The LS function values at the grid knots, $\tilde{\varphi}_j$, are organized into the vector $\tilde{\boldsymbol{\varphi}}$, the weights w_i are assembled into the vector $\boldsymbol{w}$, and the radial function values $R_{ji} = R_{ij} = \|\boldsymbol{x}_j - \boldsymbol{x}_i\|$ are gathered into a square symmetric matrix $\boldsymbol{R}$. Using these assumptions, the weights can be computed solving the following system of linear equations:

$$\boldsymbol{w}(t) = \boldsymbol{R}^{-1}\, \tilde{\boldsymbol{\varphi}}(t) \tag{4-14}$$

However, the RBF interpolation suffers from ill-conditioning of the linear system if the knots are not properly arranged in the domain or if their number is not large enough. In other words, the MultiQuadric Radial Basis Function (MQRBF) systems are conditionally positive definite. To alleviate this drawback and to compute the weights $\boldsymbol{w}_i(t)$ efficiently, the system in Eq. (4-14) is reformulated as:

$$\boldsymbol{A}\boldsymbol{w}(t) = \tilde{\boldsymbol{\varphi}}(t) \tag{4-15}$$

being the matrix $\boldsymbol{A}$ is defined as:

$$\boldsymbol{A} = \begin{bmatrix} \boldsymbol{R} & \boldsymbol{P} \\ \boldsymbol{P}^T & \boldsymbol{0} \end{bmatrix} \tag{4-16}$$

where $\boldsymbol{R}$ is the $N \times N$ symmetric RBF matrix defined in Eq. (4-13), and N is the total number of LS knots in the LS grid. On the other hand, $\boldsymbol{P} = [\boldsymbol{1} \quad \boldsymbol{x}_1 \quad \boldsymbol{x}_2]$ is an $N \times 3$ matrix containing polynomial terms. The constraints required by the conditional positive definiteness of MQRBFs are:

$$\sum_{i=1}^{N} \boldsymbol{w}_i(t) = 0, \quad \sum_{i=1}^{N} \boldsymbol{w}_i(t)\boldsymbol{x}_{1i} = 0, \quad \sum_{i=1}^{N} \boldsymbol{w}_i(t)\boldsymbol{x}_{2i} = 0 \tag{4-17}$$

The solution of this augmented system is expressed as:

$$\boldsymbol{w}(t) = \boldsymbol{A}^{-1}\, \tilde{\boldsymbol{\varphi}}(t) \tag{4-18}$$

It is important to note that the matrix $\boldsymbol{A}^{-1}$, used to update the LS interpolation weights, needs to be computed only once since the LS grid remains constant throughout the entire optimization process. Further, since the weights are assumed to be a function of time only, the gradient of $\boldsymbol{\varphi}(\boldsymbol{x}, t)$ is given by:

$$\nabla_{\boldsymbol{x}} \boldsymbol{\varphi}(\boldsymbol{x}, t) = \boldsymbol{w}_i(t)\, \nabla_{\boldsymbol{x}} R(\|\boldsymbol{x} - \boldsymbol{x}_i\|) \tag{4-19}$$

whose components along the x_1, x_2 directions assume the following expressions:

$$\nabla_{x_1} \boldsymbol{\varphi}(\boldsymbol{x}, t) = \boldsymbol{w}_i(t) \frac{(x_1 - x_{i1})}{R(\|\boldsymbol{x} - \boldsymbol{x}_i\|)}, \quad \nabla_{x_2} \boldsymbol{\varphi}(\boldsymbol{x}, t) = \boldsymbol{w}_i(t) \frac{(x_2 - x_{i2})}{R(\|\boldsymbol{x} - \boldsymbol{x}_i\|)} \tag{4-20}$$

As explained in the next section, reinitialization of the LS function needs to be periodically performed to maintain the SD property. The SD property corresponds mathematically to $|\nabla \boldsymbol{\varphi}(\boldsymbol{x}, 0)| = 1$. In order to avoid unbounded growth of the LS function, a distribution function can be introduced to approximate the gradient, i.e.:

$$|\nabla_{\boldsymbol{x}} \boldsymbol{\varphi}(\boldsymbol{x}, t)| := \bar{\delta}(\boldsymbol{\varphi}(\boldsymbol{x}, t)) = \begin{cases} 0 & \text{if } |\boldsymbol{\varphi}(\boldsymbol{x}, t)| > \Delta \\ \frac{3}{4\Delta}\left(1 - \frac{\varphi^2}{\Delta^2}\right) & \text{if } |\boldsymbol{\varphi}(\boldsymbol{x}, t)| \leq \Delta \end{cases} \tag{4-21}$$

where Δ is a parameter used for controlling the magnitude to the gradient as it will not update the LS surface if its value exceeds Δ. Its value is suggested to be a multiple of the mesh size of the discretized domain [199].

4.5 LS reinitialization

As described in prior studies, the initialization of the LSF is usually performed with the aim of maintaining the SD property of $\boldsymbol{\varphi}(\boldsymbol{x})$ [186]. In fact, during the LS evolution, numerical instabilities and variations in the velocity extension field can disrupt this property, necessitating periodic reinitialization to maintain the SD nature of the function.

Reinitialization aimed at enforcing the condition $|\nabla\varphi(\boldsymbol{x})| = 1$ commonly involves solving the so-called Eikonal equation [186] corresponding to:

$$\frac{\partial\varphi}{\partial t} + \text{sign}\,(\varphi_0)\,(|\nabla\varphi(\boldsymbol{x})| - 1) = 0 \tag{4-22}$$

with the initial condition $\varphi_0(\boldsymbol{x}) = \varphi(\boldsymbol{x}, t = 0)$ [207].

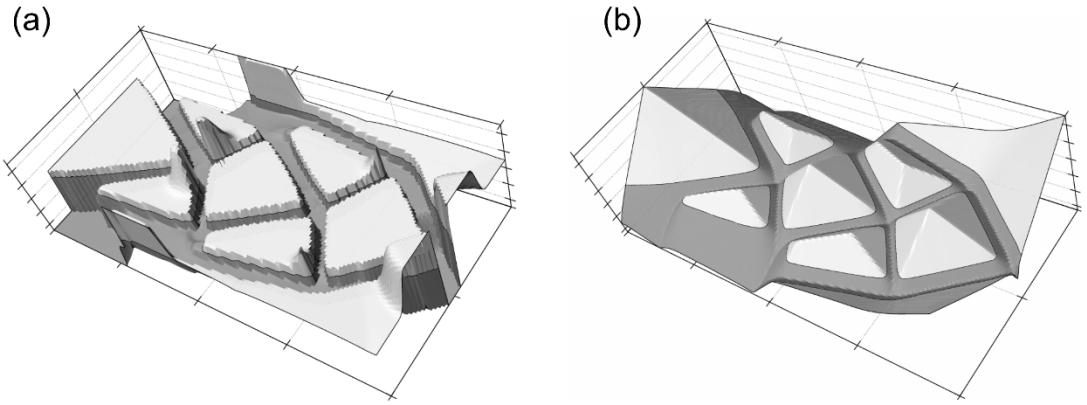

Figure 4-3. Eikonal-based reinitialization approach. The example of an optimized 2D cantilever beam before (a) and after (b) reinitialization. The figures are extracted from [207].

Even though this method guarantees high accuracy, it is computationally expensive. Therefore, other strategies have been proposed when the domains are not geometrically complex, and the computation time has to be contained. A simpler alternative to the Eikonal-based PDE for reinitialization involves reinitializing the LSF using a direct gradient normalization approach according to the following relationship:

$$\varphi_{app}(\boldsymbol{x}) := \frac{\varphi(\boldsymbol{x})}{\overline{|\nabla\varphi(\boldsymbol{x})|}} \tag{4-23}$$

where $\overline{|\nabla\varphi(\boldsymbol{x})|}$ represents the average of the LS gradient calculated along the current LS boundary, and $\varphi_{app}(\boldsymbol{x})$ is the approximated reinitialized value corresponding to $\boldsymbol{\varphi(x)}$ that will be introduced as the new value of $\varphi(\boldsymbol{x})$[199]. It should be noted that this method, also depicted in Figure 4-4, is less accurate in comparison to Eq.(4-22). An illustration of the LSF before and after this reinitialization is provided in Figure 4-5.

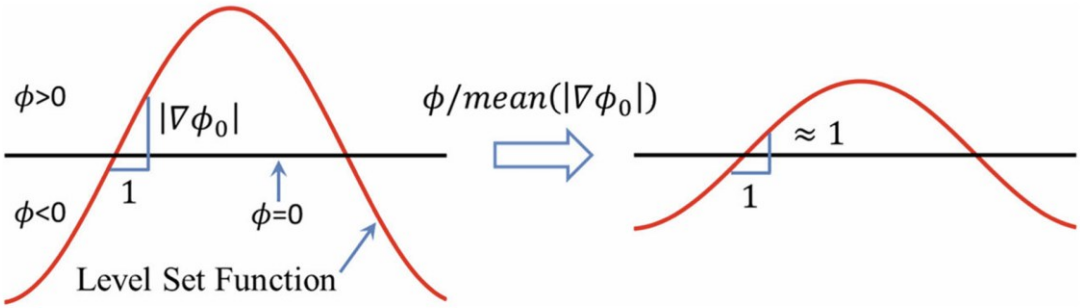

Figure 4-4. Reinitialization of the LSF using the direct gradient normalization approach [199]. Reproduced in accordance with Copyright © 2018, Springer-

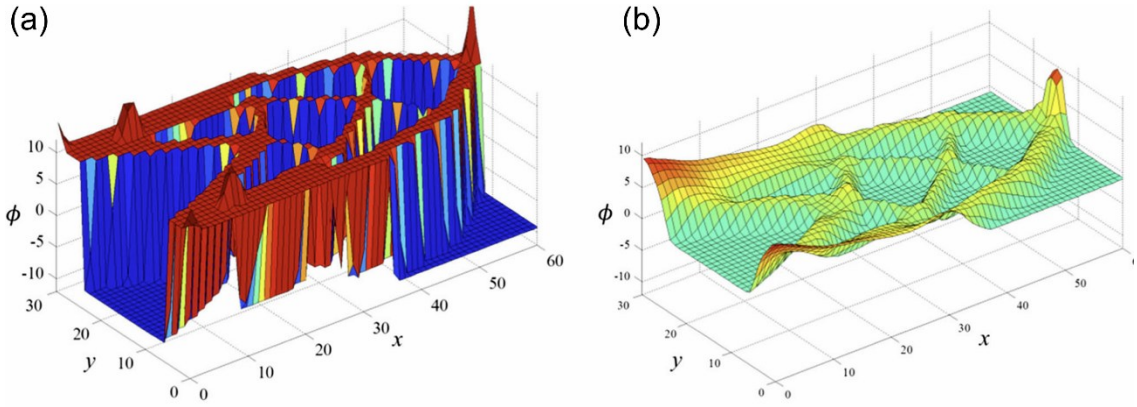

Figure 4-5. Approximate reinitialization approach to maintain SD feature of the LSF. LS before (a) and after (b) the reinitialization [199]. Reproduced in accordance with Copyright © 2018, Springer-

4.6 Optimization of a mechanical problem based on the LS approach

A topology optimization problem involves identifying the subdomain Ω with a constrained volume $\bar{V}$ (or area in 2D cases), contained within a predefined design domain D, that maximizes (or minimizes) a specified OF, $J(\boldsymbol{u}, \Omega)$, such as the structural compliance [95]. It is also possible to consider other constraints such as stress or any other resource limitation required in the design [220].

In mechanical optimization, objective functions to be minimized, such as compliance, strain energy density, or von Mises stress, are commonly employed [124, 142, 171]. For a structural problem, the mathematical formulation of the compliance minimization can be expressed as follows [145]:

$$\text{Find the minimum of } J(\boldsymbol{u}, \Omega) = \int_D H(\varphi)\psi_{st}(\boldsymbol{u})dV$$
$$\text{such that: } \int_D H(\varphi)\,\delta\psi_{st}(\boldsymbol{u}, \boldsymbol{w})dV - \int_D H(\varphi)\boldsymbol{B}\cdot\delta\boldsymbol{w}dV - \int_\Gamma \boldsymbol{t}\cdot\delta\boldsymbol{w}\,ds = 0 \tag{4-24}$$

$$\text{with} \quad c\big(\Omega(\varphi)\big) = \int_D H(\varphi) dV - \bar{V} = 0$$

Here $J(\boldsymbol{u}, \Omega)$ represents the OF, $\psi_{st}(\boldsymbol{u}) = ½\, \boldsymbol{\varepsilon}: \boldsymbol{C\varepsilon}$ denotes the elastic energy density of the material, $\boldsymbol{u}$ **is** the displacements field, and $\boldsymbol{w}$ is an arbitrary virtual displacement field. In addition, $\boldsymbol{B}$ corresponds to the external body forces, while $\boldsymbol{u_0}$ and $\boldsymbol{t}$ are the prescribed displacements and surface tractions imposed on the corresponding boundary portions of the domain Γ_u and Γ_t, respectively, with $\Gamma = \Gamma_u \cup \Gamma_t$.

The displacement field $\boldsymbol{u}$ is determined by solving the governing equilibrium equation in its weak form:

$$\int_D \boldsymbol{C\varepsilon} : \delta\boldsymbol{\varepsilon}\, dV = \int_D \boldsymbol{B} \cdot \delta\boldsymbol{w} d\mathrm{V} + \int_{\Gamma_t} \boldsymbol{t} \cdot \delta\boldsymbol{w}\, ds \tag{4-25}$$

subject to the boundary conditions $\boldsymbol{u} = \boldsymbol{u_0}$ on Γ_u and $\boldsymbol{\sigma} \cdot \boldsymbol{n} = \boldsymbol{t}$ on Γ_t. Using standard FE interpolation, the displacement and strain fields are discretized as:

$$u(\boldsymbol{x}) = \boldsymbol{N}(\boldsymbol{x})\, \boldsymbol{u_n}, \qquad \varepsilon(\boldsymbol{x}) = \boldsymbol{B}(\boldsymbol{x})\, \boldsymbol{u_n} \tag{4-26}$$

where $\boldsymbol{N}(\boldsymbol{x})$ is the shape function matrix, $\boldsymbol{B}(\boldsymbol{x})$ is the strain-displacement matrix, and $\boldsymbol{u_n}$ is the vector of nodal displacements. Substituting these into the weak form yields the system of linear equations which could be represented as:

$$\boldsymbol{K}\, \boldsymbol{u}_n = \boldsymbol{f} \tag{4-27}$$

where $\boldsymbol{K} = \int_D H(\varphi)\, \boldsymbol{B^T C B} dV$ is the global stiffness matrix, and $\boldsymbol{f}$ is the vector of applied forces. Solving this system provides the displacement field $\boldsymbol{u_n}$, from which $\boldsymbol{\varepsilon}(\boldsymbol{x})$ and $\psi_{st}(\boldsymbol{u})$ can be computed at each point in the domain. The strain energy density then guides material distribution updates during the TO process.

In typical 3D TO problems (volume can be replaced by the area in case of 2D), the optimal solution often necessitates a predefined maximum amount of material, $\bar{V}$, which is specified as $\bar{V} = \xi\, V_D$, where $0 \leq \xi \leq 1$ represents the volume fraction relative to the total volume of the design domain, V_D. To account for this volume constraint, the optimization problem in Eq. (4-24) is reformulated using the Lagrange multiplier method as follows:

$$\bar{J}(\boldsymbol{u}, \varphi, t) = \underbrace{\int_D H\big(\varphi(\boldsymbol{x}, t)\big)\psi_{st}(\boldsymbol{u}) dV}_{J(\boldsymbol{u}, \Omega)} - \lambda\, (\Omega(\varphi), t) \tag{4-28}$$

where function λ is the constraint term in Augmented Lagrange Multiplier (ALM) method which will be discussed in section 4.8, and the constraint function, $c(\varphi, t)$, has been defined using Eq. (4-5) as:

$$c(\varphi, t) = \int_D H\big(\varphi(\boldsymbol{x}, t)\big)\, dV - \xi\, V_D \tag{4-29}$$

Based on the topological derivative of the OF [122, 144, 145, 150, 198, 233], by setting $v_n = \bar{J}(\boldsymbol{u}, \varphi, t)$ the steepest descent velocity field that drives the boundaries toward minimizing the OF is expressed as:

$$v_n = J(\boldsymbol{u}, T, \Omega, t) - \lambda \tag{4-30}$$

where v_n is the normal velocity to the boundary which replaces its relevant term in Eq.(4-11). It can be observed that the evolution of the boundary slows down as the OF approaches either a local or global minimum state.

4.7 Optimization of a thermal conduction problem based on the LS approach

The TO of a thermal problem is conceptually similar to that of structural problems; however, a proper OF is required to be defined. For thermal optimization, various OFs have been explored depending on the specific physics and goals of the problem. In the heat transfer field, the requirement of minimizing the thermal energy dissipation or the entropy production often guide the optimization process [234].

In practical applications, researchers have introduced OFs aimed at maximizing the thermal conductivity, minimizing the thermal compliance, or optimizing the average diagonal components of the thermal conductivity tensor [115, 181, 235]. In this study, the minimization of heat transport capacity is adopted as the OF for the thermal optimization problem.

4.7.1 FEM in heat conduction problems

Before introducing the OFs for thermal problems it is worth providing the basics of the FEM approach in thermal conduction problems. The steady-state heat conduction problem is considered in its strong form:

$$\nabla \cdot \boldsymbol{k}\, \nabla T + \boldsymbol{Q} = 0 \tag{4-31}$$

where $\boldsymbol{T}$ is the temperature field, $\boldsymbol{k}$ is the thermal conductivity tensor (in the case of an isotropic material, $\boldsymbol{k} = \boldsymbol{I}\,\kappa$, where κ is the thermal conductivity), and $\boldsymbol{Q}$ the heat source/sink. The boundary conditions (BCs) are presented by Dirichlet BCs: $= \bar{T}$ on Γ_T and Neumann BCs: $\boldsymbol{k}\,\nabla T \cdot \boldsymbol{n} = \bar{\boldsymbol{q}}$ on Γ_q. In the previous expressions, $\boldsymbol{n}$ is the unit normal to the boundary, and $\bar{\boldsymbol{q}}$ is the known heat flux across the boundary.

The weak form of Eq. (4-31) is obtained by multiplying the governing equation by a test function δT and integrating over the problem domain.

$$\int_{\Gamma} (\boldsymbol{k}\,\nabla T) \cdot \boldsymbol{n}\, \delta T\, d\Gamma - \int_{\Omega} (\boldsymbol{k}\,\nabla T)\, \nabla \delta T\, d\Omega + \int_{\Omega} \boldsymbol{Q}\, \delta T\, d\Omega = 0 \tag{4-32}$$

Using standard FE approximations, we express the temperature field $\boldsymbol{T(x)}$ and its gradients by using the nodal temperature values collected in the vector $\boldsymbol{T}_n$ and proper shape functions $\boldsymbol{N(x)}$ and their derivatives:

$$T(\boldsymbol{x}) = \boldsymbol{N(x)}\boldsymbol{T}_n, \qquad \nabla T(\boldsymbol{x}) = \boldsymbol{B(x)}\,\boldsymbol{T}_n \tag{4-33}$$

The temperature gradient is approximated using the compatibility matrix $\boldsymbol{B(x)} = \frac{\partial \boldsymbol{N(x)}}{\partial \boldsymbol{x}}$. Substituting the approximated quantities into the weak form leads to the following system:

$$\left[\int_{\Omega} \boldsymbol{B}^T \boldsymbol{k}\, \boldsymbol{B}\, d\Omega\right] \boldsymbol{T}_n = \int_{\Omega} \boldsymbol{N}^T \boldsymbol{Q}\, d\Omega + \int_{\Gamma_q} \boldsymbol{N}^T \boldsymbol{q}_n\, d\Gamma \tag{4-34}$$

or, in matrix form:

$$\boldsymbol{K}\,\boldsymbol{T}_n = \boldsymbol{R}_Q + \boldsymbol{R}_q \tag{4-35}$$

where $\boldsymbol{K}$, $\boldsymbol{R}_Q$ and $\boldsymbol{R}_q$ represent the thermal conductivity matrix, the heat source, and the boundary heat flux, respectively.

Once the temperature field and its gradient are calculated, we can introduce different OFs to be minimized in thermal TO problems. In practical applications, researchers have introduced OFs aimed at maximizing the thermal conductivity, minimizing the thermal compliance, or optimizing the average diagonal components of the thermal conductivity tensor [115, 181, 235]. It is also possible to consider other OFs like thermal compliance, effective conductivity, and uniform temperature distribution.

In some cases, the average temperature or the maximum temperature over the design domain are the OF of the thermal conduction problem as follows [115]:

$$f(\boldsymbol{x}) = \frac{1}{|\Omega|}\int_{\Omega} T d\Omega \tag{4-36}$$

By keeping the same physical meaning, an alternative of this equation can be found in [19, 236] where the OF is defined as

$$f(\boldsymbol{x}) = \int_{\Omega} \nabla T \cdot (\kappa \nabla T) d\Omega \tag{4-37}$$

4.7.2 Thermal Compliance Minimization

Thermal compliance measures the integral of the heat source term multiplied by the temperature field across the domain:

$$f(\boldsymbol{x}) = \int_{\Omega} Q\, T d\Omega \tag{4-38}$$

where Q is the volumetric heat generation. This OF could also be found in [237] where the OF for heat sinks is presented. Minimizing this term reduces the overall

thermal energy in the system, optimizing material positioning to enhance heat conduction efficiency. This OF is common when improving heat sinks, where rapid heat transfer away from sources is desired.

4.7.3 Heat transport capacity

In our study, the minimization of heat transport capacity is adopted as the OF for the thermal optimization problem. This approach considers the integral of the dissipation function ψ_{th} evaluated across the design domain. The dissipation function quantifies the heat transport potential capacity of the material, representing the thermal conductivity potential capacitance density [234].

The dissipation function ψ_{th}, representing the thermal energy dissipated in the material, is given by:

$$\psi_{th} = \frac{1}{2}\kappa\,|\nabla T|^2 = \frac{1}{2}\frac{q^2}{\kappa} \tag{4-39}$$

Minimizing the total dissipation ψ_{th} over the design domain reduces the thermal energy dissipation, effectively improving the material's heat transport capacity.

To gain a clearer understanding of the optimization problem and connect the mathematical formulation to a physical principle, the optimization can be interpreted based on the right-hand side of Eq. (4-36). Minimizing this equation implies that material is added in regions with high heat flux. This addition enhances conductivity, thereby reducing the heat flux and smoothing out its peaks. From a physical perspective, the aim of optimization is to redistribute the conductive material in a way that the temperature gradient field becomes as uniform as possible across the design domain. Should this OF be used in Eq. (4-28), the constrained thermal TO problem is solved.

4.8 Augmented Lagrange multiplier method in TO

In optimization problems constraints are often essential to ensure that the solution satisfies certain physical or design limitations, such as material volume usage, stress limits, or energy consumption. These constraints are typically managed by introducing Lagrange multipliers, which allow the constrained problem to be transformed into an unconstrained one by incorporating penalty terms into the OF.

In the case of an optimization problem with constraints, recalling from Eq. (3-1), such as minimizing an OF, $f(\boldsymbol{x})$, subject to constraint $c(\boldsymbol{x}) = 0$, the

Lagrange Multiplier Method introduces a Lagrange multiplier λ such that the Lagrangian function $\mathcal{L}(\boldsymbol{x}, \lambda)$ is obtained:

$$\mathcal{L}(\boldsymbol{x}, \lambda) = f(\boldsymbol{x}) + \lambda c(\boldsymbol{x}) \tag{4-40}$$

The goal of the optimization problem is to find the stationary points of the Lagrangian function, which are determined by solving the following system of equations:

$$\nabla f(\boldsymbol{x}) + \lambda \nabla c(\boldsymbol{x}) = 0, \qquad c(\boldsymbol{x}) = 0 \tag{4-41}$$

This approach directly integrates the constraints into the optimization process by penalizing any violation of the condition $c(\boldsymbol{x}) = 0$. However, it often requires iterative adjustments of λ to maintain feasibility and to refine the solution toward optimality.

4.8.1 Augmented Lagrange multiplier method

The ALM method improves upon the classical Lagrange Multiplier approach by adding a quadratic penalty term to the Lagrangian. This enhancement helps to handle the constraints more effectively, especially in cases where the initial guess is far from the optimal feasible region. The augmented Lagrangian for a constraint $c(x) = 0$ is given by:

$$\mathcal{L}(\boldsymbol{x}, \lambda) = f(\boldsymbol{x}) - \lambda c(\boldsymbol{x}) + \frac{\mu}{2} c^2(\boldsymbol{x}) \tag{4-42}$$

The Lagrange multiplier is updated according to:

$$\lambda^{n+1} = \lambda^n + \gamma^n c^n(\boldsymbol{x}) \tag{4-43}$$

This equation ensures that λ moves toward the values that enforce the constraint more strictly as the iterations number n progresses. The penalty parameter γ^n is also updated to tighten the constraint, typically by incrementing it with each step:

$$\gamma^{n+1} = \min(\gamma^n + \Delta\gamma, \gamma_{\max}) \tag{4-44}$$

where $\Delta\gamma$ and $\gamma_{\max}$ are controlling parameters for the growth of the penalty parameter. This incremental update of γ ensures that the penalty grows gradually, improving the convergence of the optimization algorithm without causing excessive perturbations in the solution at early stages [96].

4.8.2 Gradual imposition of constraints in TO using ALM

To account for the volume constraint in our TO problem, using Eqs (4-28) and (4-29), the new updated Lagrange multiplier can be obtained. The Lagrange multiplier term is updated iteratively to enforce constraints effectively [199]. At the $(n+1) - th$ time step, the penalty parameter is adjusted incrementally to refine the solution and ensure convergence toward the target condition.

$$\lambda^{(n+1)} = \begin{cases} \mu\, c & n \le n_r \\ \lambda^{(n)} + \gamma^{(n+1)} c & n > n_r \end{cases} \tag{4-45}$$

where μ is the Lagrange multiplier used in the initial relaxation phase taking place while $n \le n_r$, while $\gamma^{(n+1)}$ is a penalty term to be updated at each time step according to Eq. (4-44). To gradually impose the volume or area constraint over the iterative TO procedure, a gradual relaxation algorithm is applied during the initial iterations to obtain a smooth transition of the physical domain volume in its initial state, V_0, to the desired target volume $\xi\, V_D$:

$$V_n = \begin{cases} V_0 + \frac{\xi\, V_D - V_0}{n_r}(n-1) & n \le n_r \\ \xi\, V_D & n > n_r \end{cases} \tag{4-46}$$

then Eq. (4-29) is rewritten in the following form:

$$c(\varphi, t) = \int_D H\big(\varphi(\boldsymbol{x}, t)\big)\, dV - V_n \tag{4-47}$$

In this form, the constraint function is used for both phases of the problem, including the initial relaxation of the constraint.

4.9 Immersed LSM as a tool for handling contradicting objectives

As mentioned in the previous chapter, handling multi-objective TO problems is challenging because of the non-convex nature of their problem. Expanding TO capabilities to manage multiple loads and constraints further broadens its applicability, as demonstrated by Deng and Suresh [238]. Updating existing numerical methods to better align with current manufacturing and engineering challenges is essential. In this regard, advancements in CAD and FEA applications have significantly improved the automation of TO, making it more effective and feasible. Nowadays, some commercial software packages can perform TO designs [155]; most of them require filtration and post-processing to achieve smooth boundaries, alternatively achieved at the cost of using a dense mesh.

When using LSMs, adaptive meshing is critical to accurately capture the crisp physical boundaries, as it aligns the FE discretization with the evolving LS interface [239]. However, adaptive meshing significantly increases computational costs, especially for complex geometries and fine grids. Without adaptive mesh refinement, alternative approaches such as XFEM or CutFEM are required to handle discontinuities and irregular boundaries effectively.

The immersed LSM overcomes these limitations by decoupling the LS grid from the FE mesh, enabling precise boundary representation without the need for adaptive remeshing. This approach maintains computational efficiency while

leveraging the advantages of LSM for TO [239]. Thus, unlike most TO methods, which typically use the average value of the quantity of interest in each finite element, this approach utilizes the information at the GP that is subsequently mapped, through an appropriate local interpolation, to the LS discretization domain.

Considering the issues mentioned above, the Immersed Level Set Topology Optimization (ILSTO) presented in Chapter 5 is a promising and efficient approach in TO. It considers an LS grid independent of the FE mesh, while the definition of several OFs is established. The LS grid-related values enable evolving the design variables based on the selected OF(s).

Chapter 5

A NEW IMMERSED LS-FEM APPROACH FOR COMBINED THERMO-MECHANICAL OPTIMIZATION PROBLEMS

5.1 Why immersed Level-Set (LS) method?

Advancements in numerical methods, along with shape and Topology Optimization (TO) techniques, have significantly improved reverse engineering and manufacturing processes. These developments demand continuous updates in providing solutions enabling us to address new challenges in engineering and production effectively. However, some notable issues have not yet received sufficient attention in the research community.

While modern CAD software excels in representing physical and geometric details, and FEM provides robust tools for analyzing these designs, integrating FEM outputs into iterative TO platforms remains a challenge. One of these challenges is to accurately track the boundaries provided by FEM modeling so that the final CAD model could be produced. The LS Method (LSM) offers a promising solution for tracking boundaries with precision comparable to CAD-generated designs, especially when paired with remeshing strategies. Tools like adaptive meshing and Gauss Point (GP)-based interpolation schemes ensure more accurate boundary representation during evolution, making them essential for successful integration. As mentioned previously, since dealing with adaptive algorithms is computationally and mathematically time consuming, immersed GP-based interpolation algorithms offer a simple but robust solution to the problems dealing with LS-based Topology Optimization (LSTO) problems.

This chapter presents an approach designed to construct independently a LS grid over the FE mesh, enabling the evolution of design variables according to a specific OF. The approach is demonstrated through its application to steady-state thermal conduction problems and/or a structural optimization problem, illustrating its versatility and effectiveness in addressing these challenges when Multiphysics problems must be considered. In this line of thought, this chapter covers the explanation of the proposed Immersed LSTO (ILSTO) features, multi objective TO, different regularization and mapping strategies, and the definition of suitable convergence criteria. Finally, the structure of the developed FE code and its related subroutines and modules are explained at the end of the chapter.

The proposed formulation has been limited to the study of 2D problems, even though the extension to 3D cases is straightforward. Accordingly, all equations from the previous chapter are reformulated for 2D analysis, primarily by converting volume integrals into area integrals.

5.2 ILSTO method

Since parametrizing the LSF is an efficient way of numerically tracking the boundary of the design domain, we separate the LS discretization from the FE

one used to represent the physical domain; in particular, the LS discretized domain embeds entirely the FE mesh. To this end, the ILSTO method makes use of a LS grid, L, overlapped to the FE mesh, see Figure 5-1. The material boundary Γ, identified by the zero LS of the function $\boldsymbol{\varphi(x)}$, is illustrated in Figure 5-1(c). The material is allowed to be present only in design domain D, where only temporary voids (light gray filled regions) introduced for enriching the TO solution can exist. In addition, because of manufacturing-related or design requirements, the problem can be also characterized by permanent empty regions (red circle in Figure 5-1a). In synthesis, the LS domain may contain:

Permanent voids: regions with a fixed geometry that remain empty throughout the process, ensuring that no material is added to the design domain *D*.

Temporary voids: regions that can evolve during the optimization process as dictated by the LS evolution. The initialization procedure sets all these types of voids in the design domain.

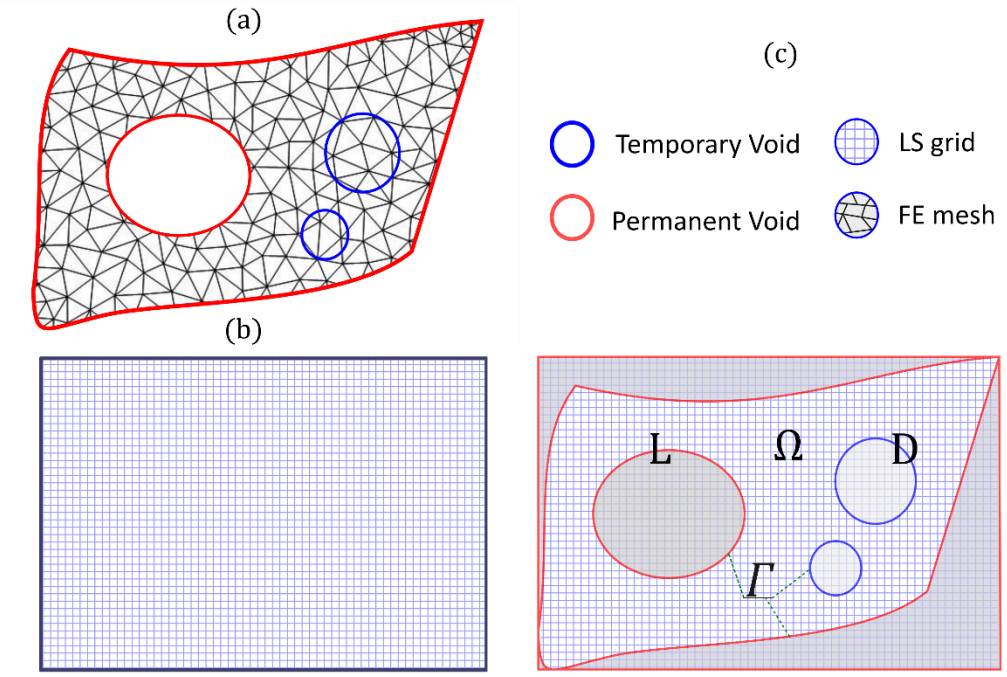

Figure 5-1 Schematic of the Immersed LS domain. An arbitrary domain including permanent and temporary void regions (a). The LS function $\boldsymbol{\varphi(x)}$ is defined at the knots of a regular rectangular grid (thin blue lines, b). LS domain L (b), problem design domain D (FE discretized region), and physical domain $\boldsymbol{\Omega}$ are outlined as well as the material boundary $\boldsymbol{\Gamma}$ (c).

The connection between the LS grid knots, on which the LSF is built, and the FE mesh is achieved through a robust interpolation algorithm, see section 5.5.2. It allows us to transfer physical quantities – such as the strain energy density and the thermal potential capacity – between the GPs and the LS grid knots. The LS

grid-FE mesh mapping also plays a pivotal role in controlling the final topology. As a matter of fact, adjusting the interpolation parameters, the degree of locality and the smoothness of the mapped quantities can be tuned at will by properly setting the interpolation parameters such as interpolation window and the interpolation kernel itself. These parameters directly influence the precision of the boundary evolution and the optimization results, allowing for greater flexibility in shaping the topology to meet specific design criteria. The interplay between the interpolation parameters and the final topology underscores the significance of the algorithm in achieving stable and accurate results in Multiphysics TO.

5.3 Thermal and mechanical TO

In Multiphysics problems, the choice of a suitable OF depends on the underlying physics and on the goal of the optimization task. For structural and thermal conduction problems, it is essential to define two appropriate OFs. In structural optimization, common OFs include the minimization of compliance, strain energy density, and von Mises stress, to mention a few [124, 142, 152, 171]. Similarly, thermal optimization can be performed by adopting various OFs. For instance, the least thermal energy dissipation principle and the minimum entropy production are frequently used to optimize heat transfer across a solid domain [234].

In the context of TO, specific thermal-related OFs have been explored. Some researchers introduced the thermal conductivity capacity [115, 181, 235] or the thermal compliance [240], while others focus on the average of the diagonal components of the thermal conductivity tensor [241]. In this work, as OF we adopt the minimization of the heat transport capacity of the thermal problem [234].

5.3.1 Thermal OF

In thermal optimization, where the material is typically assumed to be isotropic with constant thermal conductivity, the dissipation function Ψ_{th}, defined at each FE GP as stated in Eq. (4-36), represents the heat transport potential capacity of the domain and serves as the quantity to be minimized. The thermal conductivity potential capacitance density of the material is expressed as:

$$\psi_{th}(\boldsymbol{x}) = \frac{1}{2} \nabla T \cdot \boldsymbol{C}_t \nabla T \tag{5-1}$$

where ∇T represents the temperature gradient vector while $\boldsymbol{C}_t$ is the material's thermal conductivity matrix.

When the overall heat transport potential capacity of the physical domain, $\Psi_{th} = \int_D \psi_{th}(\boldsymbol{x}, T) dA$, reaches a minimum, the design achieves the optimal dissipation capacity. This implies that the material layout maximizes the thermal conductivity, thereby minimizing the heat transport potential capacity to its lowest possible value.

The optimization problem aims to achieve a physically meaningful criterion: minimizing OF in Eq. (5-1) ensures that enough material is present in regions with high heat flux, enhancing conductivity and reducing flux peaks. This redistribution of thermally conductive material leads to a more uniform temperature gradient across the design domain [234].

5.3.2 Mechanical OF

In mechanical problems, the material is typically modeled as linearly elastic and isotropic. After solving the governing PDEs, whose solution depends on the actual physical domain described by the current LS function, the stress and strain states are obtained. The mechanics related OF, which is typically the strain energy of the system, is computed at the LS grid points by interpolating the strain energy density values

$$\psi_{st} = \frac{1}{2}\, \boldsymbol{\varepsilon} : \boldsymbol{C}_e\, \boldsymbol{\varepsilon} \tag{5-2}$$

evaluated at the finite element GPs. Since the Ersatz material model is implemented, the elasticity tensor $\boldsymbol{C}_e(\varphi(\boldsymbol{x}))$ is made to vanish at GPs where $\varphi(\boldsymbol{x}) \leq 0$, so the strain energy becomes zero accordingly.

5.3.3 Thermo-mechanical combined OFs

Based on the OFs outlined in Eqs (5-1) and (5-2), the combined thermo-mechanical optimization problem, whose aim is to minimize both the mechanical compliance and the heat transport potential capacity at the same time, can be formulated by introducing a new OF, $J(\boldsymbol{u}, T, \Omega)$, as follows:

Find the minimum of:

$$J(\boldsymbol{u}, T, \Omega) = \beta \int_D H(\varphi)\, \psi_{st}(\boldsymbol{u}) dA + (1-\beta) \int_D H(\varphi)\, \psi_{th}(T) dA$$

with: (5-3)

$$\boldsymbol{u} = \boldsymbol{u}_0 \text{ on } \Gamma_u, \quad T = \bar{T} \text{ on } \Gamma_T$$

$$\boldsymbol{\sigma} \cdot \boldsymbol{n} = \boldsymbol{t} \text{ on } \Gamma_t, \quad \text{and} \quad \int_D H(\varphi) dA - \bar{A} \leq 0$$

In Eq. (5-13), the problem's BCs include displacement ($\boldsymbol{u} = \boldsymbol{u}_0$ on Γ_u, where $\boldsymbol{u}_0$ represents the prescribed displacement), thermal ($T = \bar{T}$ on Γ_T, where $\bar{T}$ denotes the prescribed temperature on the boundary Γ_T), and traction boundary condition ($\boldsymbol{\sigma} \cdot \boldsymbol{n} = \boldsymbol{t}$ on Γ_t, where $\boldsymbol{\sigma}$ is the stress tensor, $\boldsymbol{n}$ is the outward unit

normal vector on the boundary Γ_t, and $\boldsymbol{t}$ is the prescribed surface traction). Furthermore, the area constraint requires that $\int_D H(\varphi)dA - \bar{A} \leq 0$, where $H(\varphi)$ is the Heaviside function applied to the LS function φ, and $\bar{A}$ is the target area required. As it has been explained in Chapter 4, the target constraint is made to vary along the iteration process for numerical stability purpose.

In a numerical setup, once the weight parameter β is defined the OF is computed based on the contributions of the mechanical and thermal problems. When $\beta = 0$, the TO problem focuses only on the thermal minimization requirements, while $\beta = 1$ optimizes the topology for the mechanical problem alone. Intermediate values $0 \leq \beta \leq 1$ allow the formulation of a topology that optimizes both physical problems according to their respective contributions.

5.4 Velocity field update and constraints

The constraint on the maximum material domain in the TO problem is introduced through the target area $\bar{A} = \xi\, A_D$, where ξ represents the fraction of the total design domain area A_D allowed to be occupied by the material. To address this constrained optimization problem, the OF is modified using the Augmented Lagrange Multiplier (ALM) [96] approach as follows:

$$\bar{J}(\boldsymbol{u}, T, \Omega, t) = J(\boldsymbol{u}, T, \Omega, t) - \lambda\,(\Omega(\varphi), t) \tag{5-4}$$

where λ is the constraint term in the ALM method, defined as the product of the Lagrange multiplier and the dimensionless constraint function (as described in Section 4.1). It is important to note that the physical domain Ω is determined once the LS function is known across the entire design domain.

To be more specific, the ALM method proposed by Wei et. al. [199], is formulated with the following modifications. The Lagrange multiplier term at the $(n+1)$-th time step, $\lambda^{(n+1)}$, is updated as given in Eq. (4-45), based on the following conditions:

$$\lambda^{(n+1)} = \begin{cases} \mu\, c & n \leq n_r \\ \lambda^{(n)} + \gamma^{(n+1)} c & n > n_r \end{cases} \tag{4-45}$$

where μ represented the Lagrange multiplier which is active during the relaxation phase ($n \leq n_r$), while $\gamma^{(n+1)}$ is the penalty term updated iteratively using Eq.(4-44). Further, $\Delta\gamma$ and γ_{max} are input parameters required for increasing the penalty terms gradually as the constraints approach the target area. Except otherwise specified in the numerical simulations presented in the following n_r is set to 30. It can be observed that a proper selection of these parameters depends on the user's experience and the physics of the problem. However, preliminary investigations were carried out for the cases studied during the development phase of the LS method to explore the influence of these parameters.

Through these tests, we observed that very small values of μ or γ_{max}, especially μ (which governs the optimization during the relaxation phase) led to slow convergence or insufficient enforcement of the constraints; on the other hand, excessively large values could lead to numerical instability. Similarly, $\Delta\gamma$ had to be carefully balanced to avoid overly aggressive updates after the relaxation phase. Based on these practical observations, we adopted the values $\mu = 40$, $\Delta\gamma = 0.05$, and γ_{max} =5.0, which provide a consistent and stable performance across all thermo-mechanical cases. In addition, for only mechanical cases, the following set of parameters provided a better convergence: $\gamma_{max} = 50, \Delta\gamma = 3, \mu = 50$.

For sake of numerical stability, the area constraint $\int_D H\big(\varphi(\boldsymbol{x},t)\big)\,dA - \xi\,A_D = 0$ in Eq. (5-3) is reformulated in dimensionless form:

$$c(\varphi,t) = \frac{\int_D H\big(\varphi(\boldsymbol{x},t)\big)\,dA - A_n}{A_D} \tag{5-5}$$

Since the initial area $A_0 = A(\varphi_0)$ may differ from the target area $\bar{A} = \xi\,A_D$, the relaxation algorithm is introduced to gradually transition A_n from A_0 to $\bar{A}$ over the first n_r iterations. The area constraint is thus expressed as:

$$A_n = \begin{cases} A_0 + \dfrac{\xi\,A_D - A_0}{n_r}(n-1) & n \le n_r + 1 \\ \bar{A} & n > n_r + 1 \end{cases} \tag{5-6}$$

This approach ensures a smooth evolution of the physical domain while maintaining stability throughout the optimization process.

5.5 Regularization and mapping requirements for ILSTO

The following subsections outline the numerical regularization techniques essential for the stability and effectiveness of the proposed multi-physics ILSTO method. Specifically, these include time step tuning, which controls the evolution speed of the boundaries; reinitialization, which ensures numerical stability for the LS function; proper interpolation of the OF from the FE mesh to the LS grid knots.

In addition to the topics covered in the next subsections, to ensure stability in the evolution of the LS function, proper normalization strategies are also considered. This strategy aims at balancing the contributions of the mechanical and thermal OFs, preventing numerical instabilities, see Eq. (5-3). Normalization with respect to the initial average value of the OF has proven to be effective in maintaining a stable LS evolution, even when combining thermal and mechanical optimization OFs whose single values differ significantly over the iterative procedure.

5.5.1 Time-step calculations

Following the discussion introduced in section 4.3, since an explicit time scheme is adopted for H-J equation, to ensure numerical stability during time integration a CFL-related strategy is adopted [231]; it requires to limit the time step amplitude to prevent, within a single time step, the transmission of information beyond the grid size. Since in the proposed ILSTO method the physical information governing the LS evolution comes from the FE results, and the FE and LS grids are distinct, the time increment is calculated as:

$$\Delta t \leq c_t \frac{L_e}{v_{n,max}} \tag{5-7}$$

where c_t is a scaling coefficient, L_e is the characteristic length of the elements, and $v_{n,max}$ is the maximum velocity at the current step. The FE characteristic length is calculated according to:

$$L_e = \sqrt{A_{FE,max}} \tag{5-8}$$

$A_{FE,max}$ being the area of the largest finite element in the domain.

The above relationship for Δt arises from the correlation between the discretized domains and the evolution of the zero level of the LSF. Specifically, the evolution of the LS boundaries is influenced by how the $\bar{\delta}$ function interacts with the discretization.

The time step is therefore continuously updated during iterations and is influenced by the width of the approximating $\bar{\delta}$ function in Eq.(4-21). In the mentioned equation, $\bar{\delta}$ affects the cells falling within a distance proportional to Δ, where Δ represents a multiple of the problem's characteristic length.

According to Figure 5-2, the distance Δ determines the farthest affected GP with respect to the target knot of the LS grid. Consequently, the evolution of physical boundaries can be accelerated beyond the constraints of a standard CFL condition. Instead of being limited to a single cell size per time step, the evolution is governed by the distance Δ defined by the distribution function. In this study, Δ is defined as $\Delta = f\, L_e$, where L_e is calculated using Eq.(5-8), where the parameter f is a scaling factor, in the following assumed to be equal to $f = 15$. Accordingly, the time step Δt is calculated as:

$$\Delta t = \frac{\Delta}{v_{n,max}} \tag{5-9}$$

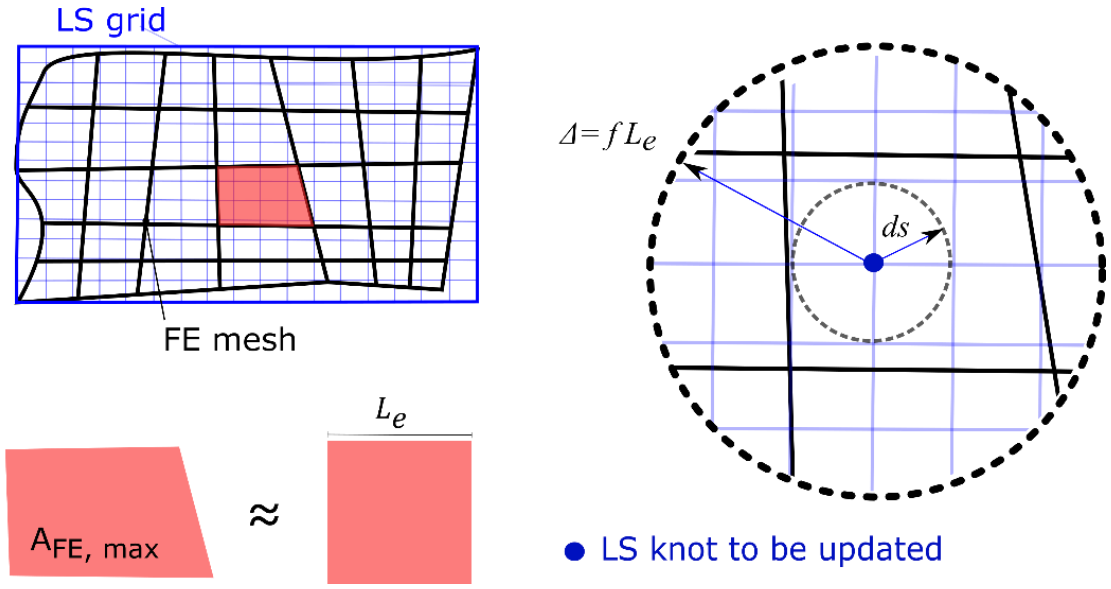

Figure 5-2. The proposed CFL-related time-step scheme. ds is the LS grid size and Δ is the length of the effective region in approximation function $\bar{\delta}$

This formulation ensures that the LS function evolves at a rate controlled by both the maximum velocity, $v_{n,max}$, and the effective width of the $\bar{\delta}$ function. By allowing the boundaries to move faster than traditional CFL limits, this approach enables efficient and stable updates of the LS function while maintaining accuracy in capturing the zero LS contours.

Substituting the $\bar{\delta}$ function from Eq.(4-21) into Eq.(4-11), and using Eq. (5-9), the LS function update becomes:

$$\varphi(\boldsymbol{x}, t+1) = \begin{cases} 0 & \text{if } |\varphi| > \Delta \\ \varphi(\boldsymbol{x}, t) + v_n(\boldsymbol{x}, t)\ \dfrac{3}{4\Delta}\left(1 - \dfrac{\varphi^2}{\Delta^2}\right)\dfrac{\Delta}{v_{n,max}} & \text{if } |\varphi| \le \Delta \end{cases} \tag{5-10}$$

which can also be written as:

$$\varphi(\boldsymbol{x}, t+1) = \begin{cases} 0 & \text{if } |\varphi| > \Delta \\ \varphi(\boldsymbol{x}, t) + \dfrac{3}{4}\left(1 - \dfrac{\varphi^2}{\Delta^2}\right)\bar{v}_n(x, t) & \text{if } |\varphi| \le \Delta \end{cases} \tag{5-11}$$

where $\bar{v}_n(x,t) = \frac{v_n(x,t)}{v_{n,max}}$ is the normalized velocity field. Eq. (5-11) highlights that the LSF is updated only close to the zero-value contours of φ, as dictated by the term $\frac{3}{4}\left(1 - \frac{\varphi^2}{\Delta^2}\right)\bar{v}_n$. Thus, both proximity to the zero LS contours and a sufficiently large $\bar{v}_n(x,t)$ values are necessary for the boundary evolution to occur. In other words, the evolution of the LS function requires two key conditions: the velocity extension field, $\bar{v}_n(x,t)$, must have a relatively large value, and the LS knot of interest must lie close to the zero LS contours. It is important to mention that the use of the approximated function $\bar{\delta}$ to represent the gradients of the

LSF, operates as a regularization procedure for the numerical setup since it controls the bounds of the LSF based on the value of Δ.

Peaks in the OF often caused by geometric features such as geometric discontinuities, may destabilize this update process. To address such an issue, the velocity field is smoothed using values from neighbouring knots to ensure a stable and consistent evolution of the LS boundaries.

5.5.2 Interpolation

To evaluate the evolution of the LS function it is essential to determine the value of the OF, $J(\boldsymbol{u}, T, \Omega)$, at each LS grid knot. For this purpose, interpolation techniques are employed to transfer the information from the FE mesh (from GPs) to the LS grid. Specifically, the thermal potential capacity, ψ_{th}, which is a scalar function evaluated from the thermal conductivity and the temperature gradient at GPs, must be interpolated onto the LS grid, see Eq. (5-1). Similarly, for the structural problem the strain energy density, ψ_{st}, requires a comparable interpolation approach starting from the GPs values, see Eq. (5-2).

An Inverse Distance Weighted (IDW) kernel, also known as the modified Shepard's method, is used for the interpolation. This method provides a weighted average of values, ensuring a smooth transfer of data from GPs to the LS grid. The interpolated value of an arbitrary function B known at the $j-th$ position related to the FE mesh, at the $i-th$ LS grid knot is given by:

$$B_i = \frac{\sum_{j=1}^{n_{GP}} w_{ij}\, B_j}{\sum_{j=1}^{n_{GP}} w_{ij}} \tag{5-12}$$

Here, n_{GP} represents the total number of GPs, and w_{ij} is the weight defined through the inverse distance between the $i-th$ LS grid knot and the $j-th$ GP, for instance. The weight is defined as:

$$w_{ij} = [\max\left(0, \frac{1}{d_{ij}+e} - \frac{1}{\overline{R}}\right)]^p, \qquad \text{where } d_{ij} = |\boldsymbol{x}_i - \boldsymbol{x}_j| \tag{5-13}$$

In the above expression, $\overline{R}$ represents the support radius of the local interpolation domain that controls the locality of the interpolation. The weight w_{ij} is non-zero only if $d_{ij} < \overline{R}$. In addition, e is a small constant added to avoid a division by zero when the LS knot and the GP coincide, with we assume $e = 10^{-8}$. Finally, p is an exponent used to penalize the weight, with $p = 0.5$ in this study, and the support radius $\overline{R}$ is defined as $\overline{R} = g \cdot L_e$ where L_e is the characteristic length of the FE discretization, and g is a scaling coefficient.

Figure 5-3 illustrates the interpolation window and the associated parameters that affect the interpolation algorithm. For both the mechanical and thermal TO here considered, the scaling factor g is set to 1, ensuring consistent locality across

both problems' domains. The locality parameter g significantly impacts the interpolation behavior and the solution of the optimization problem, as will be further discussed in the next chapter.

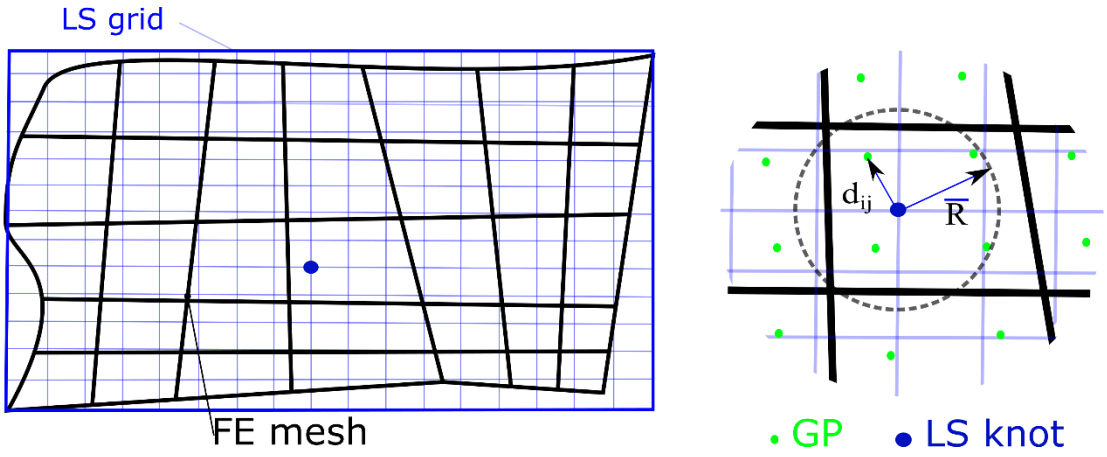

Figure 5-3. LS mapping scheme. The local interpolation kernels enable mapping the FE (black lines) quantities to the LS grid (blue lines) knots.

5.5.3 Reinitialization

As discussed in the previous chapter, it is common practice to periodically reinitialize the LS function to preserve its SD property. This is achieved by solving Eq.(4-22), which ensures the following condition is met [186]:

$$|\nabla\varphi(\boldsymbol{x})| = 1 \tag{5-14}$$

Despite its important role, solving this PDE can introduce numerical challenges, particularly when working with two independent discretized domains. A simplified reinitialization scheme was introduced in the previous chapter which replaces each LS value with a new one according to Eq. (4-23).

Using this equation requires to localize the actual zero LS and to calculate the norm of the gradients on the boundary using Eq.(4-20). The first requirement is not difficult to deal with, while relying on the gradients is computationally challenging. Having obtained the average of the gradient's norm on the LS boundary, we will be able to have an approximate reinitialization.

To mitigate these issues, a direct reinitialization algorithm, see Eq. (4-12), is employed in this study to maintain the SD property of the LS function. This straightforward approach identifies and locates the $\varphi(\boldsymbol{x}) = 0$ iso-contours, subsequently reinitializing all LS knots based on their distance to the nearest zero iso-contour [45]. It is worth mentioning that, during reinitialization, the physical domain boundaries remain static, as indicated by the blue dots in Figure 5-4.

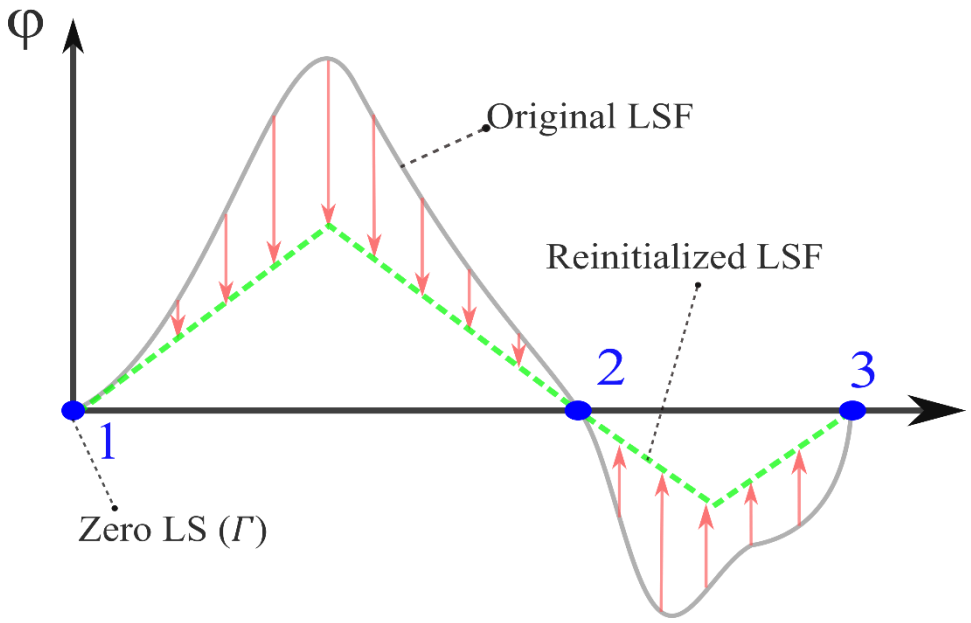

Figure 5-4. Schematic of the reinitialization strategy. At each LS knot the LS function is redefined as the SD to the closest zero LS boundary here indicated with blue dots. The gray solid line indicates the original LS function while the green dashed line indicates the reinitialized LS function

It is worth highlighting that, according to this strategy, both the distribution function and the reinitialization processes are independent of spatial gradients. Consequently, the ILSTO method eliminates the need for spatial gradient calculations, making it computationally efficient.

5.6 Convergence strategy

In structural optimization problems, the convergence assessment is typically performed by monitoring the compliance variation over time steps. However, in Multiphysics problems the convergence can be conveniently evaluated by monitoring the total thermo-mechanical energy, $J(\boldsymbol{u}, T, \Omega, t)$ as shown in Eq. (5-3), stored in the structure.

To improve computational efficiency, the convergence evaluation algorithm begins only after the relaxation phase taking place at the $n_r - th$ time step. The convergence is achieved when two conditions are fulfilled:

1) the dimensionless area (or volume in 3D problems) increment, $\frac{A_n - A_{n-1}}{A_D}$ is within a specified tolerance, and

2) the change in the total stored thermo-mechanical energy is lower than a given small value; both conditions must be verified for at least an assumed number of iterations. In the present study, we adopt 3×10^{-3} for both

tolerances, while a minimum of 20 consecutive time steps is required for satisfying the two above conditions.

Another strategy to assess convergence is to monitor whether the OF decreases as the time steps progress. If the OF increases, the LS evolution and thus the topology update are reversed, and the FE problem is solved again using half of the previous time step [231]. It is worth mentioning that this method is not always suitable because the combination of various algorithms – such as the interpolation and the ALM method – induces fluctuations of the OF values. Consequently, it cannot be distinguished if an increase of the OF comes from the natural LS evolution required for updating the boundaries of the domain, or if it is simply due to numerical oscillations.

5.7 Code structure and implementation

The ILSTO framework has been implemented in a well-structured computational FE code aimed at solving the TO problem for structural and thermal problems, see the flowchart in Figure 5-5. Its modular and efficient structure integrates preprocessing, linear system solving, and postprocessing stages, streamlining the optimization process for diverse applications.

In the preprocessing phase, the LS grid is constructed over the imported FE mesh. The initialization and parametrization of the LS function using RBF are performed, and the initial area is calculated to ensure compliance with constraints. These steps establish the foundation for the iterative-based optimization process.

The solving phase performs FE analysis to compute strain energy density and thermal capacitance at GP, using LAPACK libraries for solving linear systems. The interpolation routines map the mechanical and thermal data onto the LS grid knots through an IDW kernel. The velocity extension field is then calculated based on the interpolated data and constraints. If LS reinitialization is required, the velocity extension calculation is deferred to the next iteration, as the reinitialization already has updated the LSF.

In postprocessing, convergence criteria are evaluated, and the extracted data is prepared for monitoring with Python's Matplotlib library, enabling effective visualization and tracking of LS evolution. This enhances the interpretability of the framework's outputs and provides a robust platform for parametric studies.

The implementation leverages Modern Fortran programming language, chosen for its computational efficiency and speed of computation. Its modular capabilities and seamless integration with Visual Studio (VS) enable efficient

debugging and code management. Python complements the workflow with advanced data visualization tools, ensuring simple and smooth user handling and adaptability for real-world applications. By adopting this structured approach, the ILSTO framework provides a robust, user-friendly, and computationally efficient solution for addressing complex multi-physics TO problems.

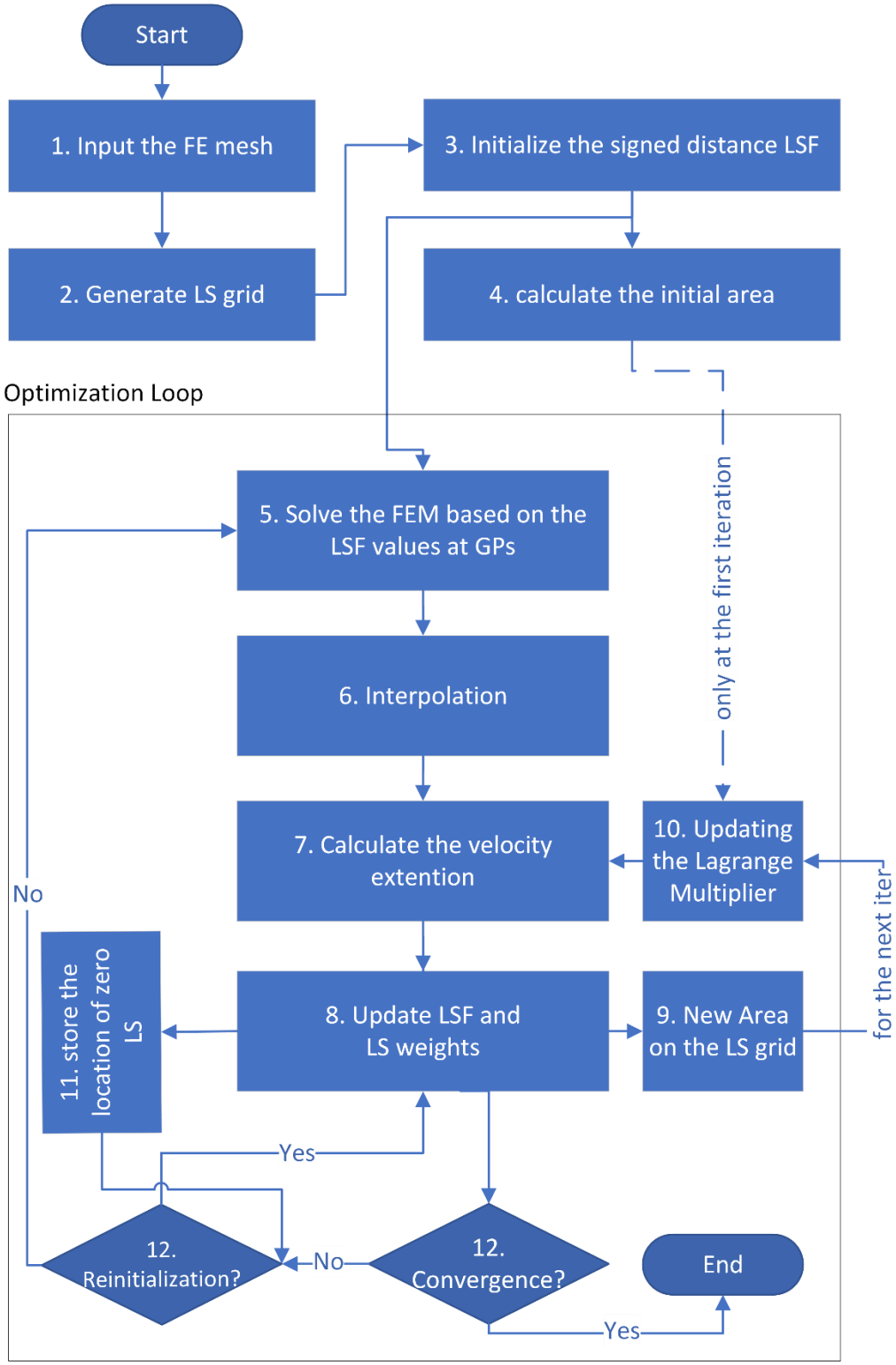

Figure 5-5. Flowchart of the proposed ILSTO approach in TO.

5.8 Conclusions

The ILSTO framework is based on a combination of computational methodologies designed to integrate the LS method with FE analysis. This integration facilitates a seamless and accurate representation of the evolving topology within the design domain. The ILSTO is particularly attractive in multi-physics problems, such as those involving structural and thermal aspects, where design constraints are required to be fulfilled.

The LSM is used to implicitly represent the topology of the design domain. The LSF, defined over a structured LS grid, characterizes the material distribution, where the zero LS contour delineates the boundary of the physical domain. To ensure numerical stability during the evolution of the LSF, reinitialization techniques are periodically employed to maintain the SD property of the LSF.

The physical domain is discretized using an arbitrary FE mesh that does not need to conform to the boundaries of the topology defined by the LSF. The LS grid and FE mesh decoupling simplifies the mesh generation and allows for high-resolution analysis of structural and thermal behaviors. The FE analysis enables us to quantify the OFs, such as strain energy and thermal gradients, which drive the optimization process using the velocity extension field.

A key aspect of the Immersed LSTO framework is the interpolation algorithm that transfers data from the FE mesh to the LS grid. Using an IDW kernel, physical quantities computed at FE GPs level are mapped onto the LS grid. The interpolation parameters – such as the support radius $\overline{R}$ and penalization exponent p – play a crucial role in controlling the locality and smoothness of the mapped quantities, as well as the topological details of the result.

To balance the contributions of multiple OFs in Multiphysics TO problems, such as compliance minimization and thermal performance optimization, a normalization strategy is adopted. Normalizing the OFs with respect to their initial average values ensures stability to the LS evolution and prevents the problem from being dominated by any single OF.

The ALM method is employed to manage the volume or area constraints during the optimization process. The method introduces penalty terms and updates the Lagrange multipliers iteratively to enforce the maximum use of material requirement, while ensuring numerical stability. The formulation of constraints by using normalized quantities further aids in achieving a smooth convergence necessary for the reliable solution of multi objective TO problems.

The convergence of the ILSTO framework is monitored through various criteria, including the minimization of the OF and the stabilization of the dimensionless area changes. The algorithm evaluates these metrics after an initial relaxation phase (which is used for relaxing the problem from values related to the constraints at the beginning of the solution) of the ALM method. In this way, the topology evolves toward an optimal state without premature termination.

Chapter 6

NUMERICAL EXAMPLES

6.1 Introduction

This chapter presents the numerical results achieved using the proposed Immersed Level-Set Topology Optimization (ILSTO) method. The results are categorized into three main sections.

First, mechanical optimization problems are analyzed, corresponding to setting to $\beta = 1$ the parameter of the combined thermo-mechanical optimization problem. This section demonstrates the capability of the proposed method to address geometric constraints while achieving optimal topologies for structural applications. Specific cases are provided to validate the robustness and efficiency of the method in handling complex design scenarios. In this section, results regarding the relationship between the density of the LS grid and the FE mesh are also presented.

The second section focuses on thermal optimization problems, corresponding to setting to $\beta = 0$ the parameter of the combined thermo-mechanical optimization problem. The examined cases illustrate the performance of the Immersed LSTO in managing heat conduction problems and optimizing thermal energy dissipation. The examples are tailored to highlight how the method adapts to purely thermal design objectives under different Boundary Conditions (BCs).

The third section presents results from combined thermo-mechanical optimization, showcasing the interplay between structural and thermal optimal requirements. These cases emphasize the versatility of the method in addressing multi-physics problems, where material distribution is optimized to satisfy both thermal and mechanical performance criteria simultaneously.

Additionally, in each of the above sections, at least one subsection explores the influence of the interpolation parameters and time-step size on the LS evolution as formulated in Eqs (5-7) and (5-13). These analyses provide insights into the sensitivity of the optimization results to the above-mentioned parameters and demonstrate the stability and convergence characteristics of the method.

The chapter closes by summarizing the key findings and emphasizing the unique advantages of the ILSTO approach. The presented results collectively validate the method's effectiveness and efficiency in addressing complex topology optimization challenges across a range of applications.

6.2 Mechanical TO

The proposed ILSTO approach is employed to optimize structural components by minimizing their compliance, defined here as the ratio of the displacement to the applied force evaluated at a representative point of the structure. It should

be mentioned that the thermal OF is neglected for all the simulations in this section, i.e., the combination parameter β is set to 1.0. Various physical domains are investigated (Figure 6-1), highlighting the impact of the Initial Topology (IT) on the optimization results. The benchmark examples include a cantilever beam and an MBB beam (named after the company Messerschmitt-Bölkow-Blohm), which are benchmark problems widely recognized in the TO community.

Additional parameters involved in the LS procedure, such as the maximum interpolation distance $\overline{R}$, are examined to evaluate their effects on the final optimized topology. Unless otherwise specified, the following parameter values are used for all analyses: $f = 10$, $g = 1$, and $\xi = 0.5$, see Eqs (5-3), (5-13) , (4-46), and (4-44).

The energy density required to evolve the LSF, that identifies the physical domain throughout the fictitious time steps, is evaluated at four GPs within each finite element. For evolving the LSF we use the approximated function together with the CFL related time step considerations relevant to the ILST.

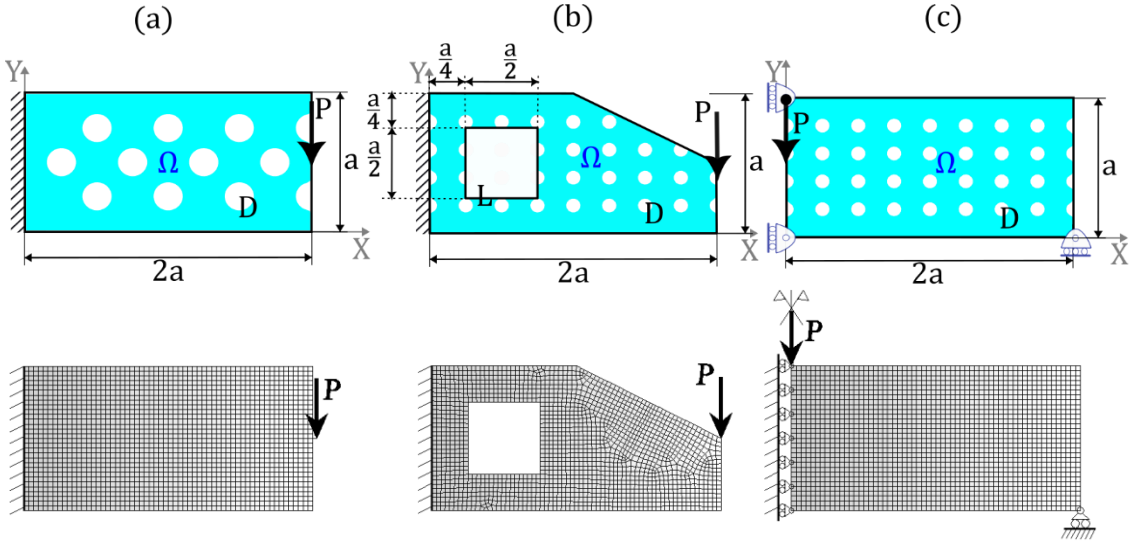

Figure 6-1. Three different design domains to be optimized by adopting the ILSTO approach. Cantilever beam in a rectangular design domain (a, discretized with 60×30=1800 finite elements), Cantilever beam in a skew rectangular design domain containing a permanent square hole (b, discretized with 1658 FEs), MBB beam (only half is considered due to the symmetry if the problem) in a rectangular design domain (c, discretized with 60×30=1800 FEs). The corresponding FE mesh is illustrated below each subfigure.

6.2.1 Cantilever beam

This section examines the TO of a cantilever beam subjected to a concentrated force (P *applied at* $(x_p, y_p) = (2a, \frac{a}{2})$); two design domains are considered: a simple rectangular domain with size $2a \times a$ (Figure 6-1a) and a more complex skew rectangular domain as shown in Figure 6-1b. The material is assumed to be

linear elastic, characterized by a Young's modulus $E = 1\,Pa$ and Poisson's ratio $\nu = 0.3$, and under plane stress conditions. The geometrical dimensions are adopted to be $a = 1m$ with a thickness of $0.1m$.

In the first structural TO considering a rectangular design domain (Figure 6-1a), TO is performed using a simple rectangular LS grid characterized by four different densities. The initial topology is adopted to start from a domain containing several regularly distributed holes. In all the following examples, the compliance is quantified through the ratio of the vertical displacement of the loaded point of the structure to the value of the applied force.

As one of the main features of ILSTO method is the separation of the LS grid and FE mesh, different densities of the LS grid are combined with the same FE mesh. It is observed that the LS grid density primarily influences the early stages of the optimization process, while the final converged shapes remain largely unaffected by the grid density. However, when using a coarse LS grid, the boundaries of the optimized shapes tend to exhibit reduced smoothness, Figure 6-1(b3). This waviness in the optimized topology boundaries indicates that coarse grids may lead to convergence to a local minimum or, in some cases even to divergence (these cases where not reported).

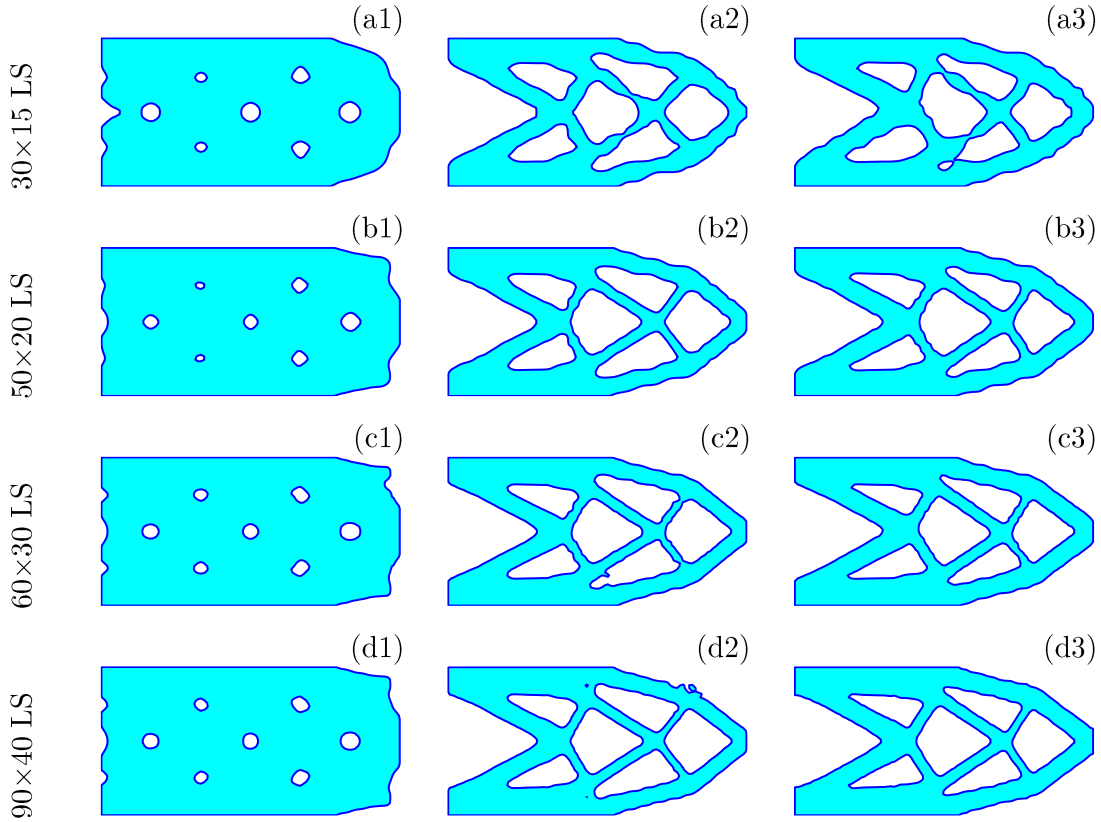

Figure 6-2. Optimized topologies for the cantilever beam problem with a rectangular design domain (Figure 6-1a, IT) are presented for different LS grid densities: 30×15 (Figs. a1–a3), 50×20 (Figs. b1–b3), 60×30 (Figs. c1–c3), and

90×40 (Figs. d1–d3) cells. The results are shown after 100, 200, and 1500 iterations in the first, second, and third columns from left, respectively.

Figure 6-3 illustrates the convergence behavior of the optimization process in terms of the physical domain area (Figure 6-3a) and of the corresponding compliance of the cantilever beam (Figure 6-3b). The convergence of the physical domain area is effectively achieved across all LS grid densities, with fluctuations primarily driven by the reinitialization process. Compliance convergence, however, demonstrates a waviness pattern as iterations progress, particularly with coarser LS grids. This behavior arises from the dependency of LS function interpolation on the FE mesh, where coarser grids lead to less precise boundary definitions, amplifying fluctuations in compliance and area.

Notably, as shown in the magnified section of Figure 6-3, finer LS grids significantly mitigate these disruptions, ensuring smoother compliance and area profiles after each reinitialization step. This indicates that finer LS grids contribute to improved numerical stability and consistency during the optimization process, despite slightly higher computational costs. Therefore, achieving the optimal trade-off between computational efficiency and result accuracy requires to carefully balance the FE mesh density and the LS grid refinement, tailored to the simulation's specific objectives and constraints.

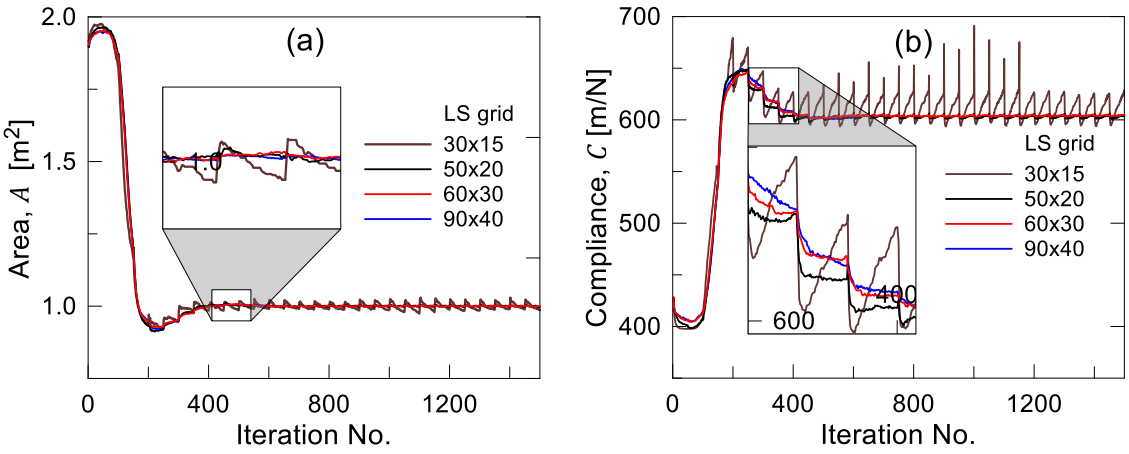

Figure 6-3. Convergence of the TO problem for the cantilever beam with a rectangular design domain (Figure 6-1a) for four different LS grids: 30×15, 50×20, 60×30, and 90×40. The convergence results are presented in terms of the area of the physical domain (a) and the evolving compliance of the structure (b).

6.2.2 Optimization of a cantilever beam with an IT without holes

The problem is now revisited with an initial design domain lacking temporary holes. The dependency of the optimized solution on the initial LS function – defined as the SD from the physical boundaries – and the influence of the effective

local interpolation radius on the Final Topology (FT) are investigated. The energy density field is interpolated over the LS grid based on FE Gauss point values, with variations in the parameter g determining $\overline{R}$ Eq.(5-13).

Figure 6-4 (b) and (c) illustrate that a more non-local interpolation ($g = 3$ vs. $g = 2$) leads to different optimized topologies, although convergence in terms of area and compliance shows a slight sensitivity to g (*Figure 6-5*). This observation again highlights that compliance is governed predominantly by the global topology of the design domain, with local boundary features having a lower impact on the OF.

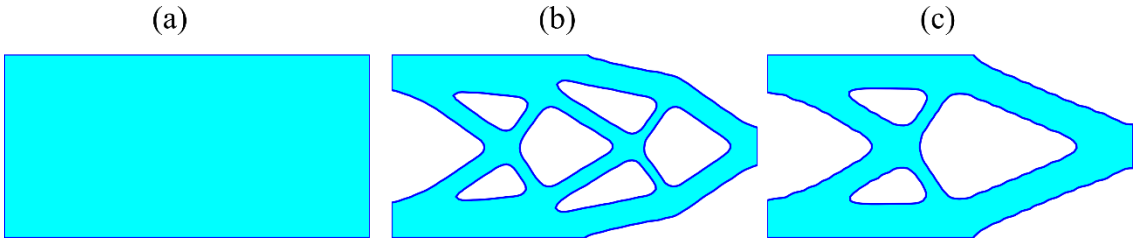

Figure 6-4. Optimized topologies of the cantilever beam with a rectangular design domain (Figure 6-1a, IT) using a 60x30 LS grid. Converged results for $g = 3$ (b) and $g = 2$ (c) in the energy density interpolation.

It can be noticed that the influence of the assumed IT on the final optimized configuration is minimal, as observed through comparisons of the solutions obtained from different starting conditions (e.g., Figure 6-2(e3) and Figure 6-4b). Regardless of whether the design domain begins as fully filled or includes temporary holes, the optimized topology converges to a similar global structure, demonstrating the robustness of the optimization process. This behavior suggests that the global compliance objective primarily governs the optimization trajectory, while local details of the initial LS configuration, such as the presence or absence of holes, have a negligible effect on the FT. This insensitivity can be attributed to the fact that the ILSTO approach effectively evolves the domain boundaries based on the compliance and volume constraints, overriding minor variations in the starting configuration. However, initial topologies with high irregularity might introduce local numerical artifacts, which could marginally impact boundary smoothness rather than structural performance.

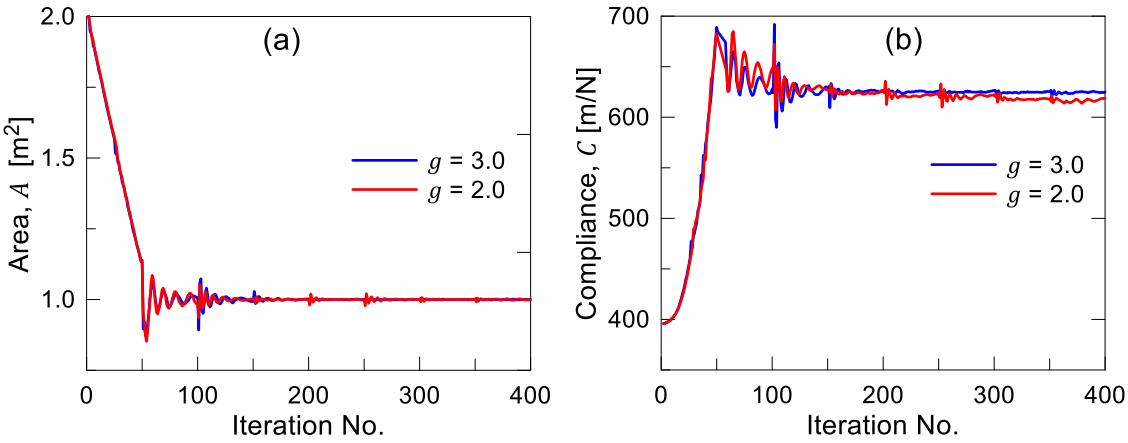

Figure 6-5. Convergence of the TO problem (cantilever beam with a rectangular design domain, Figure 6-1a) for an IT without holes: convergence in terms of area (a) and compliance (b) using $g = 2.0$ and $g = 3.0$ for energy density interpolation.

6.2.2.1 Parametric study on the time step effect on TO

The effect of the time step on the optimization process is analyzed in this section. The time step serves as a coefficient that scales the CFL-related time step according to Eq. (5-7). In this parametric study, it is observed that, for a wide range of time step values, the final optimized topologies are nearly identical, differing primarily in the evolution speed. This highlights the influence of the time step on computational efficiency: a properly chosen value can accelerate convergence without altering the final solution. Consequently, for sake of brevity, the final topologies are not presented here given their minimal variations under typical conditions.

However, it must be noticed that when the evolution speed during the relaxation phase is too slow, the optimization process may fail to achieve the global minimum topology. This limitation arises because significant topological changes occur predominantly during the relaxation phase, driven by the velocity extension field. A slow evolution during this phase can prevent the boundaries from fully adapting to the optimal configuration. As a result, the process may converge prematurely to a local minimum, failing to exploit the full potential of the relaxation phase to refine the topology toward the global optimum. This finding underscores the importance of carefully balancing the time step to ensure efficient and effective boundary evolution.

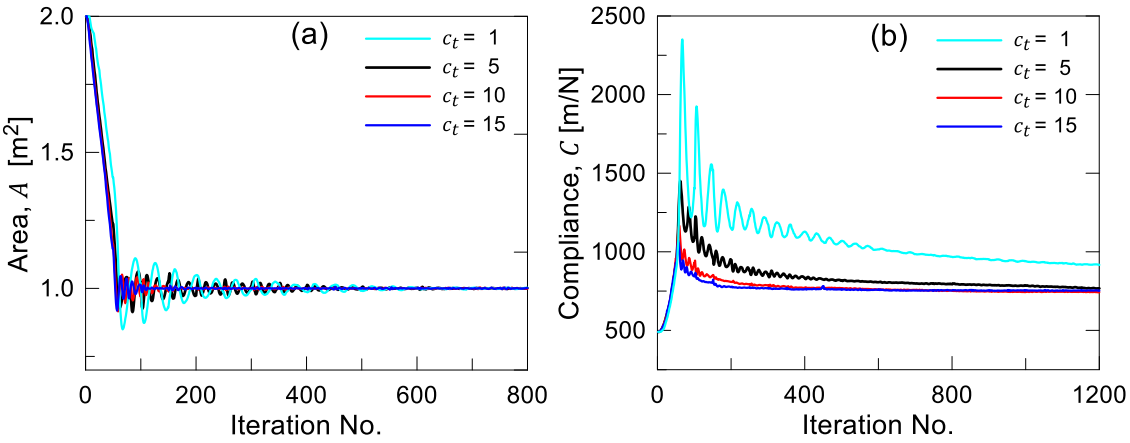

Figure 6-6. CFL-related time-step coefficient effect on TO convergence. According to Eq. (5-7), time step coefficients equal to $C_t = 1, 5, 10, 15$ *are used.*

6.2.3 Optimization of a cantilever beam with a complex design domain

The optimization of a cantilever beam with a more complex design domain, namely a skew rectangular domain with a permanent internal square hole subjected to a concentrated force, is analyzed hereafter (Figure 6-1b). The material and geometric parameters are kept identical to those used in the rectangular design domain example. In addition, to investigate the influence of the IT, two cases for the IT are considered:

Case 1: Initial domain without temporary holes (Figure 6-7a).

Case 2: Initial domain containing temporary holes (Figure 6-7b).

The resulting optimized topologies for each case are shown in Figure 6-7c and Figure 6-7d, respectively. It can be observed that in both cases, optimization successfully satisfies the constraints imposed by the external and internal fixed boundaries of the design domain, resulting in consistent topologies.

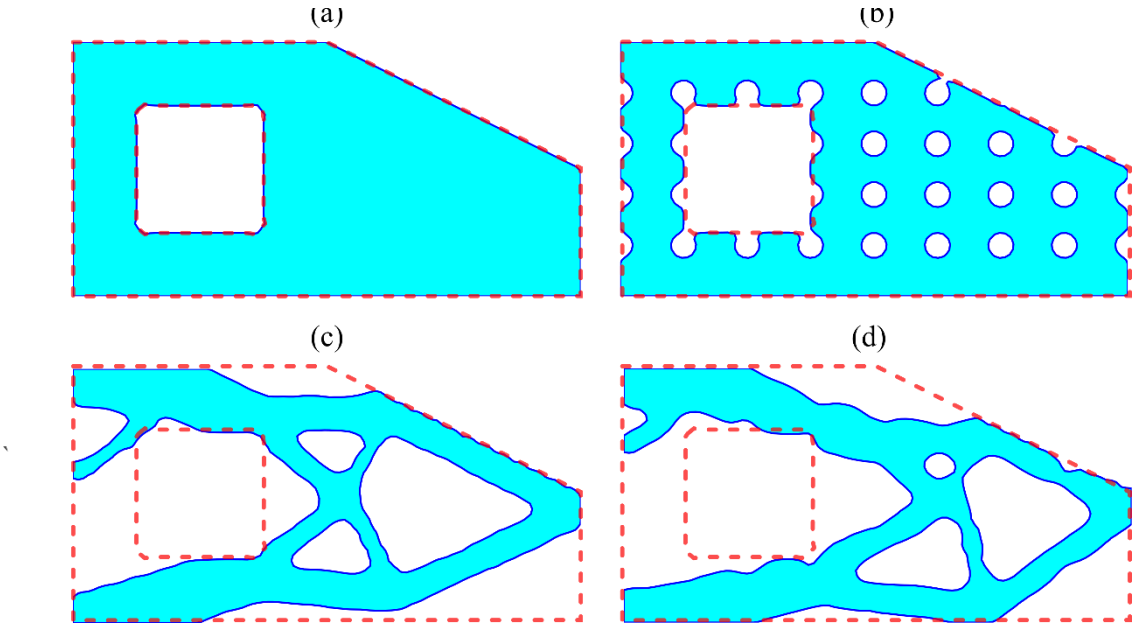

Figure 6-7. Optimized topologies for cantilever beam with a generic design domain containing a permanent square void: IT without (a) and with (b) temporary holes. The optimized configurations are obtained using a 60×30 LS grid. The corresponding optimized topologies are illustrated in (c) and (d), respectively. In all the layouts, the material distribution is contained within the design domain marked by dashed red lines.

Convergence in terms of the area of the physical domain and compliance is depicted in Figure 6-8a, and Figure 6-8b, respectively. Despite the substantial differences in the initial area and compliance values due to the completely different initial domains, the results (area and compliance) converge to similar values. Notably, starting with an initial domain containing multiple temporary holes results in final solutions with less smooth boundaries compared to those derived from a holes-free IT. This discrepancy arises because boundary smoothing does not significantly influence the numerical objective of compliance reduction or the satisfaction of the volume constraint. From the perspective of TO, see Eq. (4-30), the OF prioritizes minimizing structural compliance (a measure of deformation under loading) while maintaining a specified material volume. The roughness or waviness of the boundaries, particularly in designs with temporary holes, has little effect on these global performance metrics. This happens because the compliance is primarily governed by the internal material distribution and stiffness, not by minor variations in boundary shape. Similarly, the volume constraint is concerned with the total amount of material used, not on how the material is distributed within the physical boundaries.

However, smooth boundaries may be desirable in practice for manufacturing feasibility or aesthetic reasons, which is why penalization constraints targeting

boundary smoothness can be introduced without drastically altering the OF's outcomes.

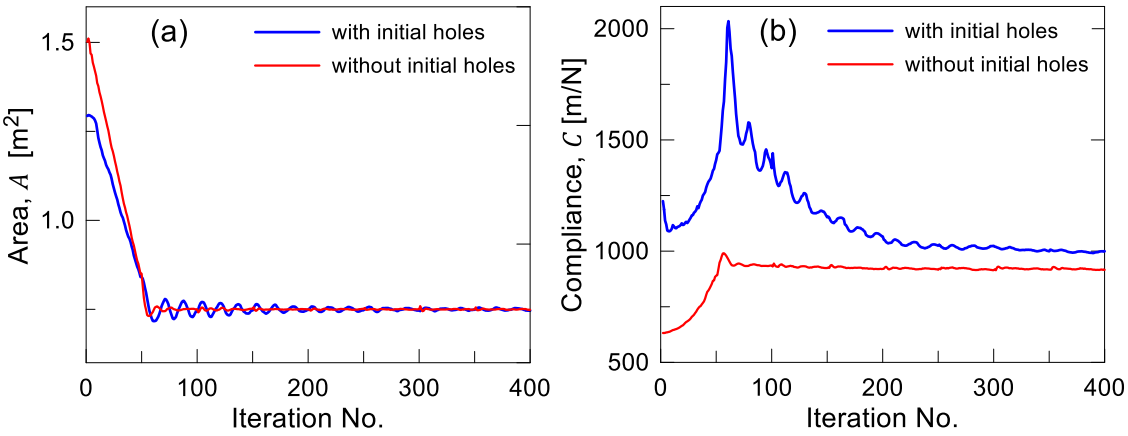

Figure 6-8 Convergence of the TO problem (cantilever beam with a skew rectangular design domain with a permanent void) for initial topologies with and without initial temporary holes. Convergence is presented in terms of the physical domain area (a) and compliance (b).

The target area is determined based on the physical domain where the material can be present, rather than over the entire LS domain. This distinction is significant since the LS domain measures $2\,m^2$ while the physical domain is only $1.5\,m^2$. Consequently, achieving $50\,\%$ of the area corresponds to obtaining $0.75\,m^2$ within the physical domain, a value that is efficiently reached in this TO solution.

6.2.4 MBB beam

The last example for mechanical compliance minimization considers the optimization of an MBB-beam (Figure 6-1c). Due to the symmetry of the problem with respect to the Y axis, only half of the beam is considered. The material properties and the FE discretization are the same used for the case shown in Figure 6-1a. In this case, in addition to the application of the proposed ILSTO method, the interpolation effect when mapping the data from the FE domain to LS domain has also been studied. In a different set of examples, the effectiveness of the initial design is studied for the MBB beam.

Regarding the interpolation radius, it can be observed that employing a smaller support domain – effectively resulting in a more localized interpolation of strain energy density – produces optimized topologies with an increasing number of finer details (Figure 6-9). This is because a smaller support domain allows the algorithm to capture and resolve higher spatial frequencies in the material distribution, leading to intricate patterns and features in the design. It should also be mentioned that while these details may enhance the mechanical

performance, they might also pose challenges for practical implementation and manufacturing.

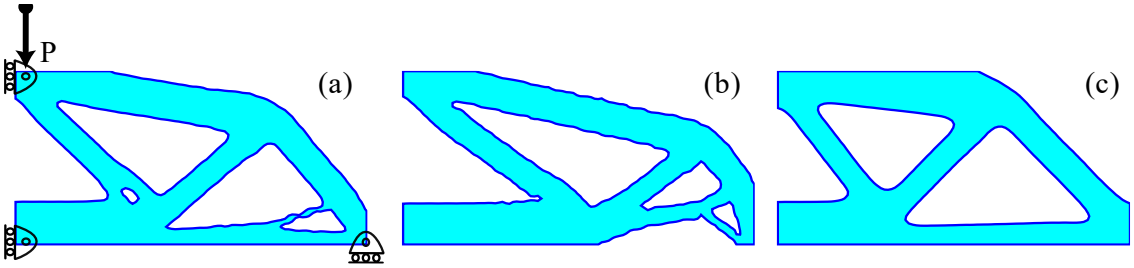

Figure 6-9. Optimized topologies of an MBB beam: result obtained starting from an initial fully filled domain using a 60x30 LS grid with various values of the interpolation parameter g: g = 0.5 (a), g = 1.0 (b), and g = 3.0 (c).

The mechanical response of the three distinct optimized topologies is largely similar, indicating that the overall structural behavior is governed by the global configuration rather than by minor variations in topology details. This suggests that, while intricate features may refine the design, their contribution to the overall performance is minimal compared to the role of the broader structural layout.

The convergence behavior illustrated in Figure 6-10 demonstrates the progressive fulfilment of the area constraint and the attainment of the minimum compliance objective as the iterations advance. This highlights the optimization method's efficiency in redistributing material to meet design goals (OFs and constraints) while maintaining computational stability.

The similarity in performance across the optimized topologies reinforces the idea that global design features are the primary determinants of mechanical effectiveness, with localized details having a secondary impact. This understanding is valuable for balancing design complexity with practical considerations such as computational cost and manufacturability.

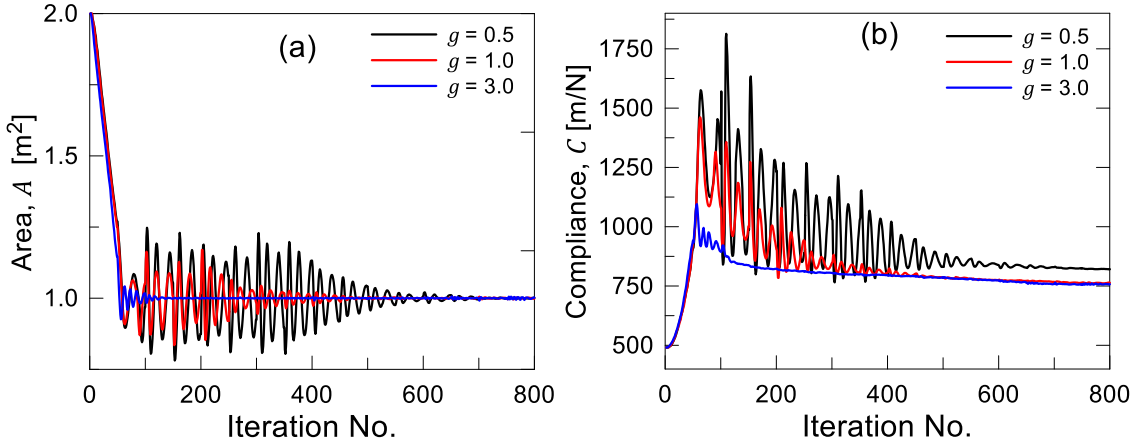

Figure 6-10. Convergence of the TO for an MBB beam (Figure 6-1c) with an IT without holes; convergence in terms of area (a) and compliance (b) for three

different values of the interpolation parameter, namely $g = 0.5$, $g = 1.0$ *and* $g = 3.0$.

6.2.4.1 The effect of initial configuration on the MBB beam

In a complementary case study, the effect of the initial distribution of voids on the optimization process is evaluated for the MBB beam. It is observed that smaller values of g, defining the effective support domain of the local interpolation, result in intricate geometrical details and local variations along the physical boundary. Although these finer features have negligible influence on overall compliance, they introduce local irregularities in the topology. Consequently, this leads to slight oscillations in the convergence curves, as shown in Figure 6-12, indicating a minor sensitivity of the optimization process to these local boundary variations.

The above results demonstrate the influence of the initial domain on the FT, suggesting that the optimization process may converge to a local minimum instead of a global one. Despite differences in the FT, the area constraint is consistently satisfied, and the compliance values asymptotically approach a stable value as the number of iterations increases. This highlights the fact that, although the final configuration may slightly vary based on IT, the solution remains within the established design constraints.

Furthermore, the degree of local interpolation, controlled by the parameter $\overline{R}$, plays a crucial role in determining the smoothness of the boundary of the physical domain. A smaller $\overline{R}$ allows for more detailed topological features, thus leading to a finer representation of the optimized structure. In contrast, larger values of $\overline{R}$ filter out these finer details, resulting in smoother boundaries for the physical domain. This behavior is analogous to techniques used in the SIMP (Solid Isotropic Material with Penalization) approach, where smoothing strategies are introduced to prevent issues like checkerboarding and mesh dependence, which can otherwise lead to unrealistic or inefficient designs [124, 140]. These methods ensure that the optimization process leads to stable, physically realizable solutions, while mitigating the risk of spurious local minima and undesirable artifacts.

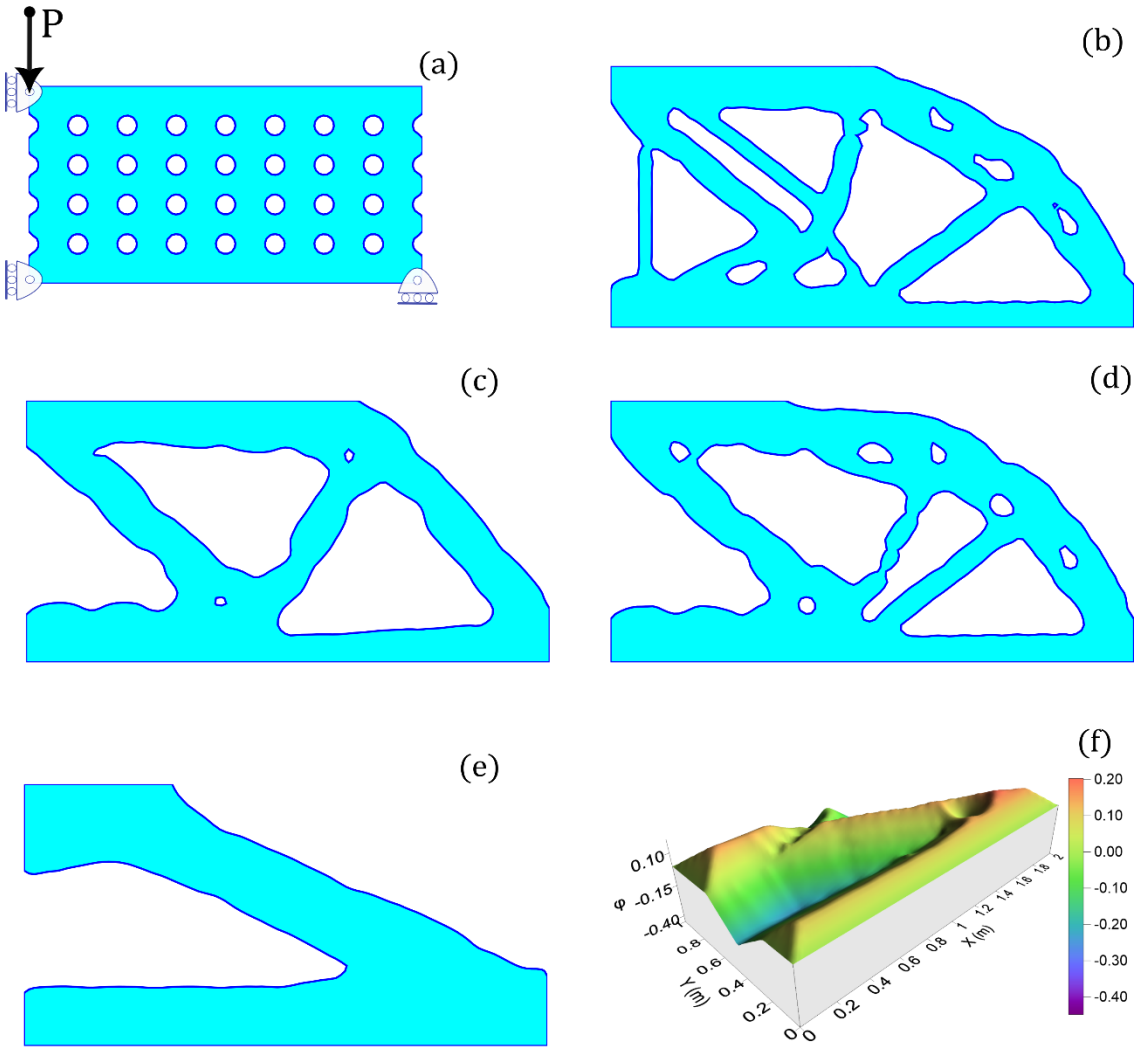

Figure 6-11. Optimized topologies of an MBB beam (Figure 6-1c): IT with several small holes (a). Optimized shapes obtained by adopting a 60x30 LS grid and different values of the parameter g: $g = 1$ (b), $g = 1.5$ (c), $g = 2.0$ (d), and $g = 6$ (e). LSF plot at convergence when $g = 6$ (f).

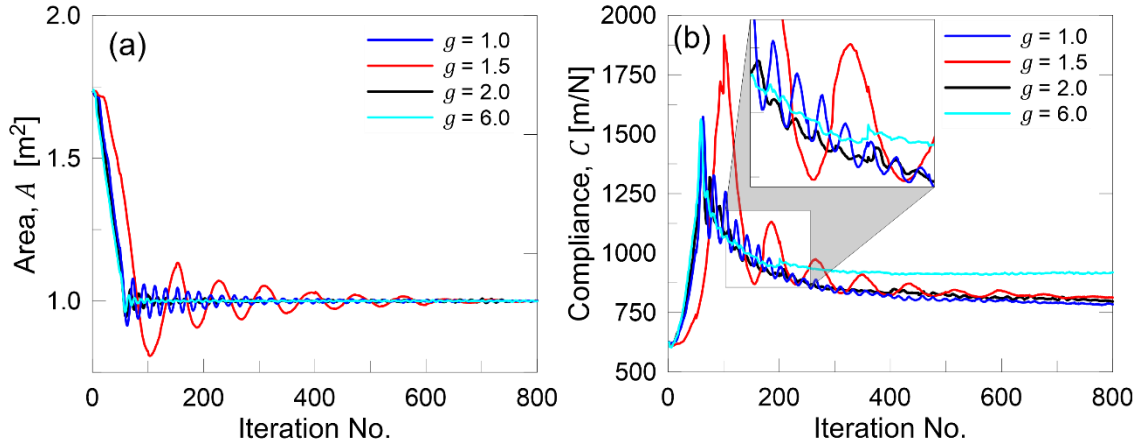

Figure 6-12. Convergence of the TO of an MBB beam shown in Figure 6-1c for an IT with several small holes. Convergence in term of area (a), and of the

compliance (b) by adopting the following values of the parameter g*:* $g = 1.0$, $g = 1.5$, $g = 2.0$, *and* $g = 6.0$.

6.3 Thermal TO

In this section, the proposed ILSTO method is applied to determine the optimal topology of a cantilever beam structure undergoing a purely thermal conduction problem ($\beta = 0$).The beam is characterized by a design domain with dimensions of $2.0 \times 1.0\,\mathrm{m}^2$ and a thickness of $0.1\,m$, and is discretized using 60×30 4-noded rectangular finite elements according to Figure 6-1. The LS grid is composed of 90×50 rectangular cells. The material is homogeneous, isotropic, and linear elastic, with a Young's modulus $E = 1\,\mathrm{Pa}$ and Poisson's ratio $\nu = 0.3$, under plane stress conditions. Additionally, for thermal conduction purposes, the material is assumed to be thermaly isotropic with conductivity $\kappa = 1\,\mathrm{W/(mK)}$. These settings are consistent with typical assumptions used in TO [241].

6.3.1 Assuming different BCs for thermal problem alone

Different boundary conditions are adopted as illustrated in Figure 6-13. Specifically, fixed temperatures T_1 and T_2 are prescribed on distinct portions of the boundary. The optimization aims to minimize the total heat transfer capacitance by redistributing material within the design domain to achieve efficient thermal performance.

The heat transfer capacitance density (as defined in Eq. (5-1)) typically exhibits higher values near boundary regions where temperatures are prescribed. This phenomenon arises because the temperature gradient is most pronounced near these boundaries, leading to higher rates of heat transfer. Consequently, the resulting optimal topologies tend to allocate the material strategically to manage these thermal gradients effectively.

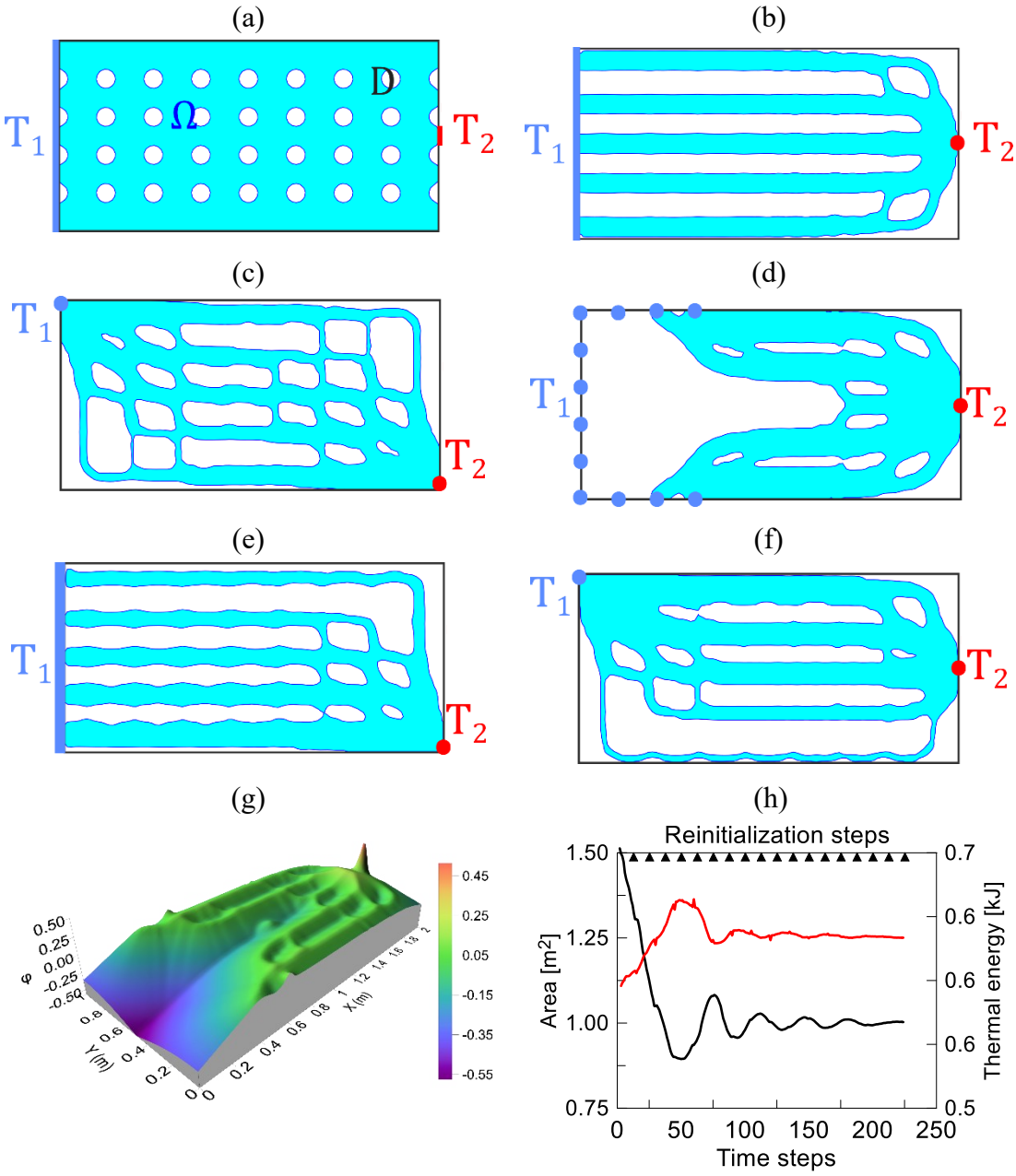

Figure 6-13. Optimized topologies for $\beta = 0$ (purely thermal TO) under various BCs: initial configuration (a); optimized topologies for BCs (b)-(f); optimized LSF (g) for the case having the BCs shown in (d); convergence curves of area and thermal energy for case shown in (f), $T_1 = 293°C,\ T_2 = 403°C$ (h).

The results indicate that the optimization algorithm effectively distributes material in regions with high-temperature gradients based on the prescribed boundary conditions. This material layout ensures that the optimized topology addresses the thermal demands of the system while adhering to the constraint on the amount of material available ($\xi = 0.5$ *in Eq.* (5-6)). On each sub-figure, the corresponding BCs are shown illustrating how the material is allocated depending

on the assumed BC. This clearly demonstrates the algorithm's ability to balance thermal performance and material usage.

A notable observation arises when the temperatures T_1 and T_2 are applied uniformly along the entire left and right vertical boundaries of the design domain. In this scenario, a uniform temperature gradient is established across the material along the x −direction, leading to the absence of an optimal solution [122]. This result highlights the limitations of the algorithm under certain boundary conditions that fail to introduce localized thermal variations, a critical factor in driving meaningful topological changes.

Moreover, the optimization minimizes the heat transport potential capacity by strategically distributing high-conductivity material within the design domain. This targeted allocation ensures that the topology fulfills the prescribed material constraints while enhancing thermal performance. The results underscore the importance of boundary condition configuration and material constraints in achieving efficient and practical solutions in thermal TO problems.

6.3.2 Effect of the initial domain topology

A critical aspect in TO is the dependency of the optimized topology on the initial material distribution. This sensitivity is particularly evident in the LSM approach, where IT plays a significant role in determining the evolution of material boundaries. However, in the previous sections it has been shown that with the proposed ILSTO the dependency on the IT could be avoided, though slight dependency was observed for the purely mechanical case.

The present sub-section considers the optimal thermal conduction problem starting from various initial domains, each one defined by different numbers and sizes of voids. These configurations range from fully solid domains to those with multiple predefined holes and enable assessing how the optimization algorithm responds to these variations. This study highlights the influence of IT on the robustness and reliability of the solution, offering insights into its practical implications.

In the considered cases, the initial configurations are designed with varying numbers and sizes of holes, ensuring that the total initial area remains constant. This choice is made on purpose, as the area constraint significantly influences the Lagrange multiplier (Eq. (4-30)) which in turn affects the LS evolution during the early stages of the numerical process.

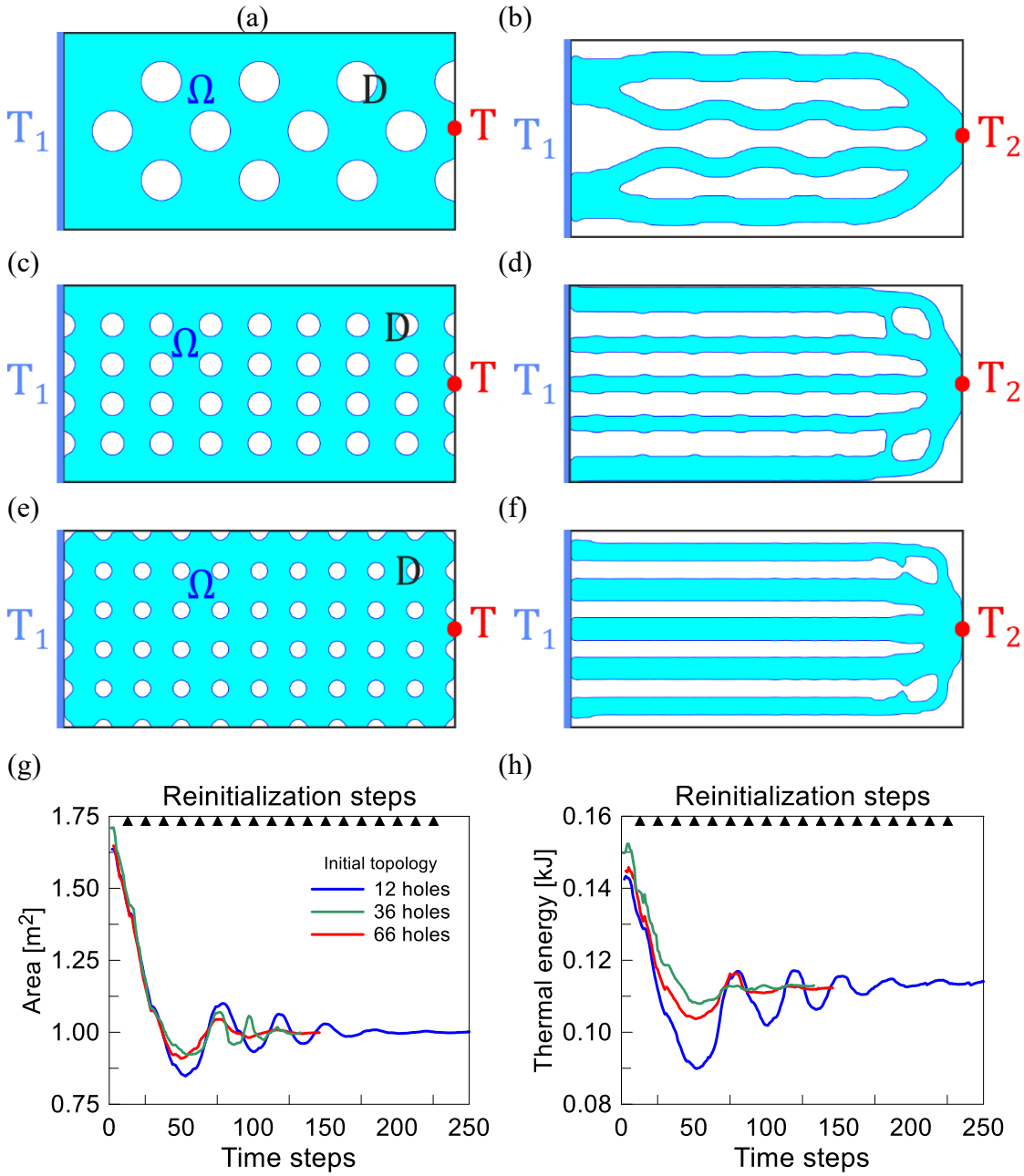

Figure 6-14. Optimal topologies derived from different initial domains: (a), (c), and (e), with their corresponding final configurations shown in (b), (d), and (f). Convergence of area and thermal energy for the three cases is depicted in (g) and (h).

The obtained results reveal that initial domains with fewer, larger holes are less likely to converge to a global minimum. Conversely, configurations with numerous smaller holes provide greater flexibility for material redistribution, facilitating the evolution toward a global minimum. Beyond LS evolution, convergence behavior is also influenced by the ALM method, where slight adjustments to the penalty parameters in Eq. (4-30) can cause the solution to deviate from the global minimum.

Despite variations in the final topological details (Figure 6-14b, d, f), all cases successfully satisfy the area constraint and minimize heat capacitance, achieving similar values at convergence. This indicates that, while an arbitrary initial configuration may hinder achieving a global minimum, the OF is still minimized, and the area constraint is fulfilled. The total energy for the different cases is shown in Figure 6-14h, highlighting these outcomes.

6.4 Combined thermo-mechanical TO

This section addresses the integration of thermal and mechanical optimization under combined objectives constraints to determine FTs. For the FEM, the same mesh used in Figure 6-1a with 1800 regular 4-noded finite elements was adopted. The resulting configurations are analyzed and discussed, highlighting the interplay between thermal and mechanical requirements in shaping the final topologies. Particular attention is paid to the role of the interpolation schemes of the fields involved and how they influence the outcomes. This dependency is explored in the subsequent subsection, where variations in interpolation parameters are systematically examined to assess their effects on the combined optimization process.

The optimal topologies for the cantilever beam considered earlier are further examined in this section by incorporating various values of the OF combination parameter β. This approach enables the integration of the thermal optimization problem, exemplified by the topology shown in Figure 6-13f, with the mechanical optimization problem corresponding to the cantilever beam configuration.

By systematically adjusting β, the balance between thermal and mechanical objectives is investigated. The results provide insights into how varying this parameter influences the final topology and the trade-offs achieved between these two competing OFs.

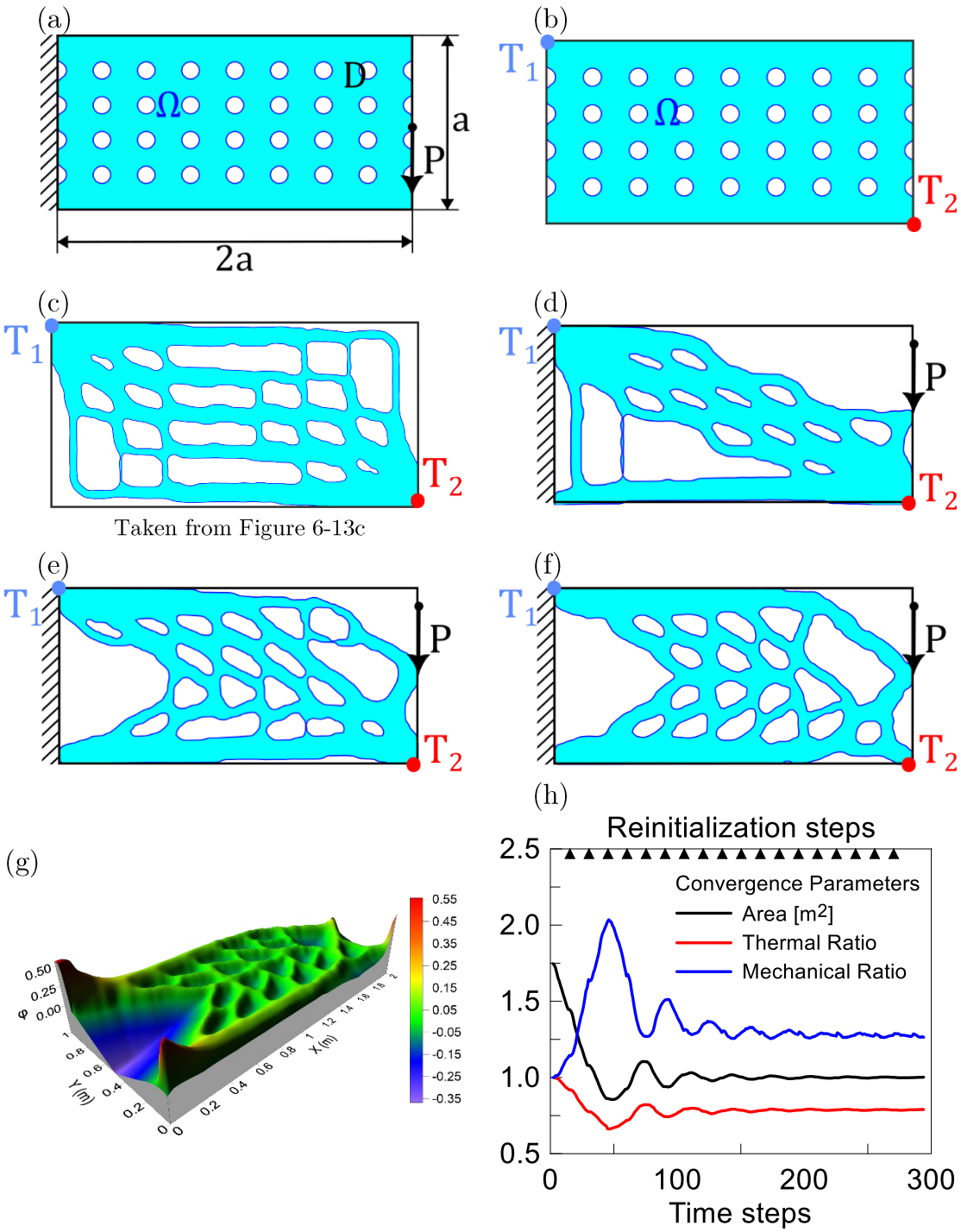

Figure 6-15. Combined thermo-mechanical TO of a cantilever beam: BCs and design domain for the structural (a) and thermal (b) problem. Optimized topologies for $\beta = 0.0$, 0.1, 0.5, and 0.9 are shown in (c)–(f). The optimized LSF for case (f) is depicted in (g). Convergence of area, mechanical, and thermal ratios for $\beta = 0.5$ is depicted in (h).

The combined thermo-mechanical TO problem demonstrates the critical influence of the combination parameter β on the resulting material distribution. When β takes small values, such as 0.1, the thermal conductivity objective dominates the optimization process. In such cases, the material is preferentially

distributed in alignment with the thermal boundary conditions, which typically direct the material toward a diagonal arrangement within the design space where the temperature gradient is maximum. This behavior aligns with the OF of the thermal problem, which consists of minimizing the thermal resistance, where the material layout reflects the path of heat flow.

As the value of β increases, the structural aspect of the optimization problem gains prominence. In the case of β approaching 1, the material distribution starts to favor structural performance, leading to a more truss-like configuration that maximizes load-bearing capacity while minimizing structural compliance. These results highlight the flexibility of the combined optimization approach, as the value of β offers a smooth transition between the thermal and structural performance objectives. The intermediate cases, where β is neither too small nor too large, allow for a balanced material distribution, optimizing both the mechanical and thermal OFs in a way that reflects the relative importance of each OF. By adjusting β, the designer can control the trade-off between thermal conductivity and structural compliance, offering a versatile framework for optimizing Multi-Disciplinary Topology Optimization (MDTO) problems.

The convergence curves shown in Figure 6-15(h) reveal a consistent progression towards the desired material usage, with both the mechanical and thermal ratios – defined as the current OF value divided by its initial counterpart – displaying a steady tendency toward stabilization as iterations increase. This suggests a well-controlled convergence process. However, the dimensionless convergence curves also highlight a fundamental characteristic of the combined thermo-mechanical optimization problem: the opposing nature of the thermal and mechanical objectives. Regardless of the boundary conditions applied, the thermal and structural objectives exhibit contrasting material distribution requirements. Specifically, the thermal convergence curve tends to attain peak when the structural convergence curve reaches its minimum, illustrating the inherent conflict between optimizing for thermal conductivity and mechanical performance. This phenomenon underscores the trade-off in MDTO problems, where simultaneous improvements in both objectives can be difficult to achieve without compromises.

The intermediate LS contours provide valuable insights into the optimization dynamics of the thermo-mechanical problem. The gradual evolution of the topology highlights the stable convergence behavior achieved during iterations. From the initial topology at time step 1 (Figure 6-16a) to the final converged topology at step 248 (Figure 6-16f), the progression showcases a smooth transition characterized by material redistribution in response to the thermal and mechanical OFs minimization.

The ILSTO method effectively balances the competing objectives of thermal conductivity and mechanical compliance. Notably, the absence of erratic oscillations or abrupt shifts in the boundaries reflects the robust interpolation and mapping strategies employed in the algorithm.

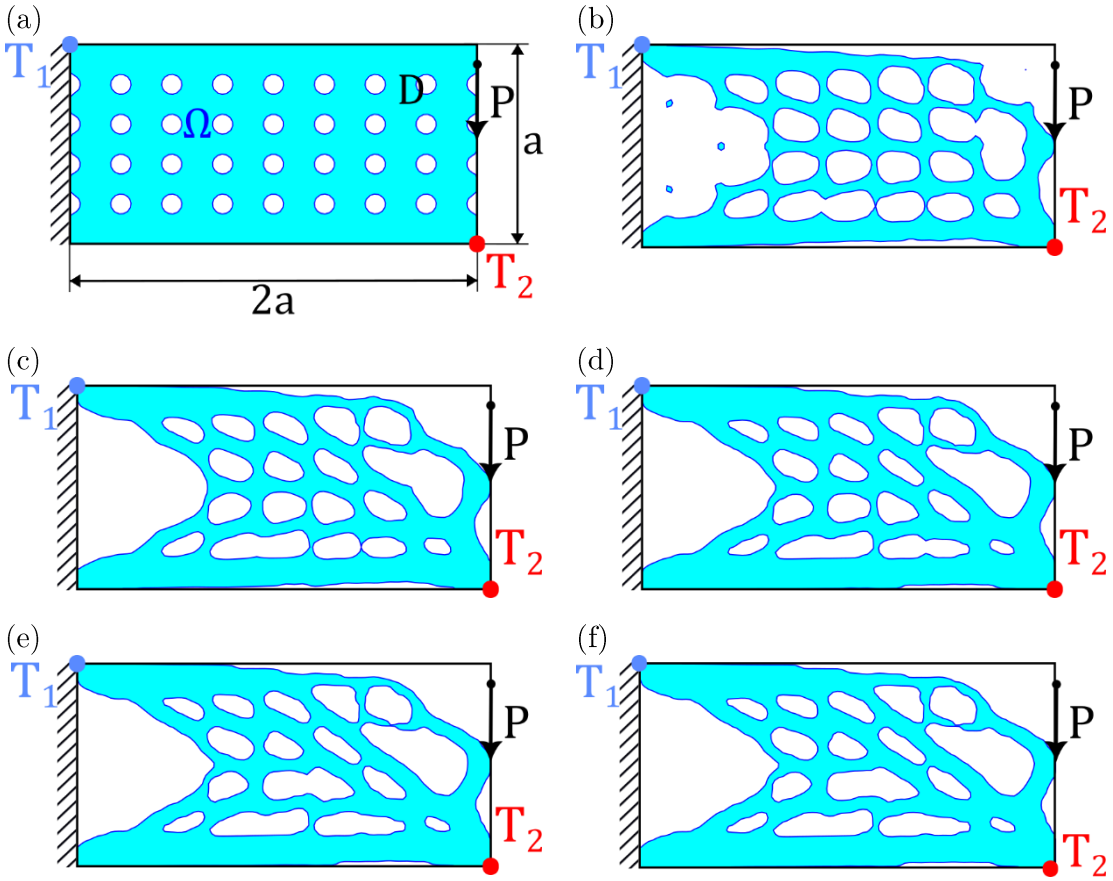

Figure 6-16. Evolution of a thermo-mechanical TO problem for $\beta = 0.5$ using the ILSTO method. Topology obtained at different iteration steps: 1 (a), 50 (b), 100 (c), 150 (d) , 200 (e), and 248 (f, final convergence). The zero-LS contours illustrate the gradual evolution of the topology toward the optimal one.

We can also observe that the majority of the evolution occurs during the relaxation phase (see Eqs (4-46) and (4-45)), as can be appreciated from the significant changes in topology observed approximately between time steps 1 and 100 according to Figure 6-16 (a to c). Beyond this iteration number, only minor topology changes occur, as reflected in the relatively stable contour shapes from iterations 150 to 248 according to Figure 6-16 (d to f). According to the mentioned equations, both μ and A_n play an important role in determining the constraint term in the velocity extension field Eq. (4-30), by properly tuning μ, users can precisely control the balance between the energy of the actual physical domain $J(\boldsymbol{u}, T, \Omega, t)$ and the constraint term λ, tailoring the optimization dynamics to achieve more precise and efficient results. This insight is critical for

enhancing the robustness of ILSTO in addressing complex multi-physics problems with different BCs.

An important consideration in the optimization process is the impact on the overall mechanical performance, which is typically quantified through the total compliance of the structure. In Figure 6-17, a noticeable trend is the decrease in compliance and mechanical ratio as the value of β increases. This trend highlights the shift in the material distribution as the weighting factor between the thermal and mechanical objectives is altered. To better capture the behavior of these quantities, two additional cases with β values of 0.3 and 0.7 have been considered. These cases offer further insight into the gradual transition between purely thermal and purely mechanical optimization, shedding light on how varying β influences both the mechanical and thermal performance of the optimized structure.

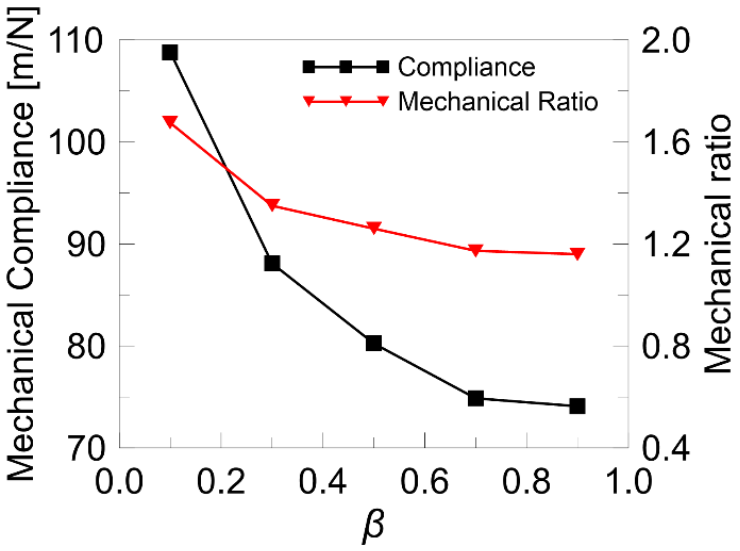

Figure 6-17. Mechanical compliance and mechanical ratios vs β for the optimization problem shown in Figure 6-15. Higher β values lead to better structural performance.

6.4.1 Effect of interpolation radii on thermo-mechanical optimization

In this section, we investigate the effect of varying the interpolation radii values, g, on the optimal topology of a cantilever beam in a combined thermo-mechanical optimization problem. As discussed in 5.5.2, the interpolation radius plays a critical role in defining the level of detail the LS-based optimization achieved in the FT. For clarity, the coefficients that determine the extent of the interpolation domain for the mechanical and thermal problems are varied independently, with g_{st} and g_{th} taking values of 1, 2, and 4. The combinations of these parameters are applied to solve the combined problem with the BCs shown in Figure 6-15 (a, b) with a weight combination parameter $\beta = 0.5$. This approach helps to explore how the interpolation radius influences the

optimization results and allows us to assess the trade-off between boundary details and the computational efficiency in achieving the desired performance.

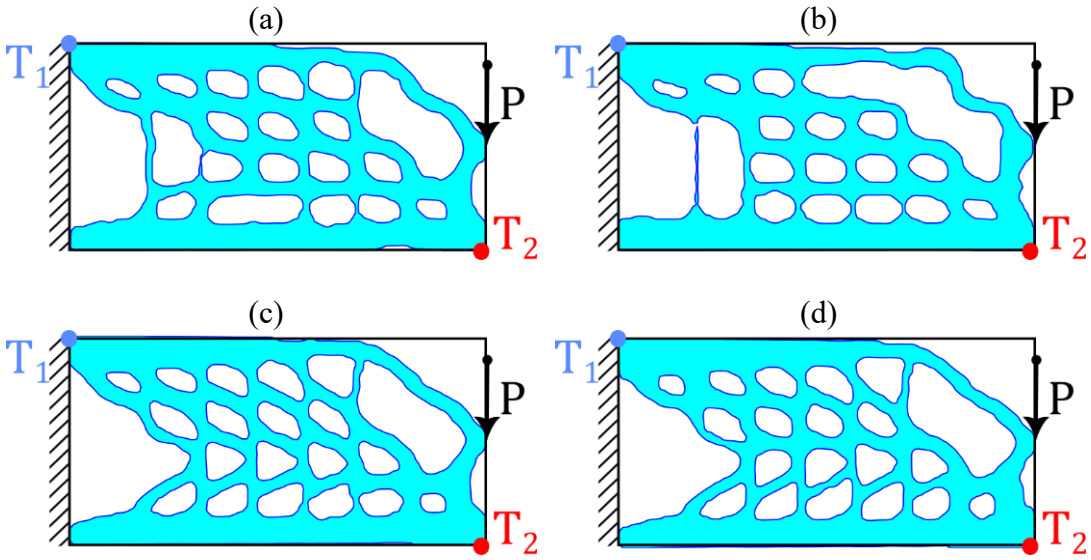

Figure 6-18. Optimized topologies for the combined thermal and mechanical TO problem with $\beta = 0.5$, considering various effective interpolation coefficients: $g_{st} = 2, g_{th} = 1$ (a); $g_{st} = 4, g_{th} = 1$ (b); $g_{st} = 1, g_{th} = 2$ (c); and $g_{st} = 1, g_{th} = 4$ (d). The subscripts 'st' and 'th' represent the structural and thermal interpolation radii, respectively.

The FTs show some variation in the material distribution details depending on the interpolation radius, but the overall shape remains consistent across different cases. This indicates that while finer details are sensitive to the interpolation radius, the broader structural and thermal characteristics are not significantly altered.

As seen in Figure 6-18, modifying the interpolation radius affects the mechanical TO more than the thermal one. The strain energy density, which governs the mechanical response, shows more localized variations compared to the heat transfer potential capacitance. Therefore, the mechanical OF is more sensitive to changes in the interpolation radius, while the thermal OF remains relatively unaffected.

6.5 Concluding remarks

The present chapter has presented the application of the proposed ILSTO method for combined thermo-mechanical TO problems. The approach decouples the FE discretization from the LS grid used to describe the physical boundaries of the design domain. This methodology introduces the flexibility to independently define the FE mesh and the LS grid, enabling efficient handling of complex boundary conditions and design domain shapes, and multi-physics

optimization problems. The mapping between the FE domain and the LS grid is performed using a local interpolation technique that maps the strain energy density and thermal capacitance values, providing a more accurate and flexible solution to the optimization problem.

The combined thermo-mechanical TO considers the simultaneous minimization of mechanical compliance and thermal capacitance, two OFs that often conflict with each other. The results reveal that the FT for the mechanical problem, which favors a truss-like structure, contrasts with the topology for the thermal problem, which tends to distribute material more evenly to minimize heat conduction. The study shows that multiple local minima exist, where the mechanical and thermal objectives reach comparable values of compliance and thermal capacitance. Despite variations in the initial design domain, the performance of the optimal solutions remains similar across different configurations.

Additionally, the studies highlight the flexibility and robustness of the proposed method. By allowing different discretization for the physical domain and LS grid, the approach can easily handle problems with varying boundary conditions and geometries. The method does not require using LS gradient information for velocity field updates or reinitialization, streamlining the computational process.

Moreover, it has been demonstrated that with proper tuning of the interpolation parameters, the need for additional filtration of the LS surface can be avoided. The results showcase the versatility of the ILSTO approach, making it suitable for a wide range of MDTO and complex engineering applications.

Chapter 7

CONCLUSION AND FUTURE RESEARCH DIRECTIONS

7.1 Overview of contributions

This thesis provides a comprehensive exploration of mechanical and thermal topology optimization (TO), addressing its theoretical foundations, computational innovations, and diverse applications to complex engineering challenges. It begins with a novel piece of research on multi-morphology Triply Periodic Minimal Surfaces (TPMS) and porous metamaterials, extending the possibilities of lightweight and efficient structural designs. These early studies highlight how TPMS-based designs can achieve precise tailored multi-functional properties, while metaplates here constituted by advanced porous metamaterials, allow us to exceed the classical limits such as those defined by Ashby-Gibson models, offering new paradigms for structural and thermal efficiency.

Building on this foundation, the research considers significant advancements in computational methods with the development of the new Immersed Level-Set Topology Optimization (ILSTO) framework. By decoupling the finite element (FE) mesh from the level set (LS) grid, this approach introduces greater flexibility and computational efficiency, facilitating the optimization of complex domains characterized by intricate boundary evolutions.

Finally, the thesis shows the application of the proposed computational approach to solve the optimization of multi-physics problems. The integration of structural and thermal optimization within the ILSTO framework demonstrates its robustness in balancing competing objectives, providing insights into systems design possessing optimal thermo-mechanical performance. These contributions collectively advance TO's capacity to address modern engineering challenges, bridging theoretical innovations with practical applications.

7.2 Summary of the main results

In the following subsections we summarize the key findings of the thesis, highlighting the main novelties of the conducted research activities performed during the 3-year long doctorate. The following papers are extracted from the doctorate research activities:

Published papers:

- Roberto Brighenti, **Farzad Tatar**, *Thermo-mechanical performance of two-dimensional porous metamaterial plates*, International Journal of Mechanical Sciences, 238, 107854 (2023).
- Noroozi, R., **Farzad Tatar**, A. Zolfagharian, et al. *Additively Manufactured Multi-Morphology Bone-like Porous Scaffolds: Experiments and Micro-Computed Tomography-Based Finite Element Modeling Approaches*. International Journal of Bioprinting, 8(3) (2022).

Under-review papers:

- **Farzad Tatar**, Roberto Brighenti. *Immersed structural topology optimization based on Level-set methods*, Structural and Multidisciplinary Optimization (Submission date: August 2024)
- **Farzad Tatar**, Roberto Brighenti. *Immersed FEM Level-Set Method for combined Thermo-Mechanical Topology Optimization Problems*. Computer Methods in Applied Mechanics and Engineering (submission date: November 2024)

7.2.1 Multi-morphology TPMS structures and metaplates

Chapter 2 presents novel contributions to the design of lightweight, porous structures. TPMS-based lattice structures are shown to achieve multi-morphology configurations when efficiently integrated together, allowing for tailored load-bearing performance. Different mechanical lead-bearing capacities were obtained by combining different graded TPMS structures as well as different lengths of transitional zone between two distinct structures.

The introduction of metaplates as 2D porous metamaterials demonstrates how structured designs can exceed classical mechanical limits. This research provides a pathway for the development of advanced materials with superior structural efficiency. In addition, a theoretical framework was stablished for predicting the thermal conductivity of metaplates using the simple yet computationally efficient waterfall algorithm concept. It has been proved that for a lattice structure it can happen that the global material characteristics exceed the theoretical and experimental limits for porous structures, proving that the porosity alone is not the only factor influencing the global behaviour of porous-based structures designs.

7.2.2 Structural optimization using ILSTO

The proposed ILSTO framework proves to be effective in optimizing structural elements under mechanical constraints. Firstly, the flexibility to adopt independent FE and LS grids ensures computational efficiency, as any arbitrary FE mesh can be optimized, while preserving high boundary resolution. Secondly, selecting finer grids for the LS domain results in a smoother boundary representation despite a slightly higher computational effort. In addition, parametric studies demonstrate the importance of the interpolation radii used for the local mapping of FE data into the LS domain; it has been shown that larger radii of the local interpolation function support, result in smoother boundaries but require careful balancing to maintain computational efficiency because it is possible to fall into a local minimum. Finally, despite the dependency on initial topologies of the optimal topology obtained, the optimized solutions exhibit

robust performance, fulfilling area constraints and achieving compliance minimization, though in some cases a deviation from a standard final topology was observed.

7.2.3 Thermal optimization

The thermal TO studies minimize heat transport potential capacitance, distributing material in regions with high temperature gradients. Results emphasize on the initial configurations, such that with smaller voids global minima convergence would be more feasible. In addition, the results demonstrate the ability of the ILSTO method to handle complex boundary conditions while ensuring robust convergence of area and thermal energy dissipation.

The thermal TO is aimed at minimizing the heat transport potential capacitance by distributing the material in regions with high temperature gradients. The obtained results emphasize that an initial configuration featuring small voids is more likely to guide the optimization problem toward a global minimum compared to configurations with large initial voids. In addition, the obtained results demonstrate the ability of the ILSTO method to handle complex boundary shapes and boundary conditions, while ensuring a robust convergence of area and thermal energy dissipation.

7.2.4 Combined thermo-mechanical optimization

The combination of thermal and mechanical Objective Functions (OFs) highlights the trade-offs between conflicting design requirements: The combination parameter β introduced in the multi-physics TO used in these cases, plays a pivotal role, with lower values favoring thermal objectives and higher values prioritizing mechanical performance. Furthermore, convergence curves reveal that the thermal and mechanical OFs require distinct material distributions, leading to competing optimization paths, see **Figure 6-15**. Nevertheless, the ILSTO approach successfully balances the required objectives, providing optimal topologies that meet thermal and structural requirements by complying with the constraints of the problem.

7.2.5 Parametric and sensitivity studies

Extensive studies on parameters, such as interpolation radii and time-step evolution, reveal that larger interpolation radii, $\bar{R}$, smooth boundaries but filter out smaller topological details, which may cause the problem to fall in a local minimum. In addition, the CFL-related time-step significantly accelerates the evolution of the boundaries in a meaningful way. However, due to the formulations of the velocity extension field, see Eq.(4-30), and relaxation procedure for the constraint's consideration, the boundaries are influenced during the relaxation

phase. Thus, selecting a too small time-step, i.e. not scaling up the normal CFL, may trap the problem into a local minimum.

7.3 Challenges and limitations

Despite its successes, the research acknowledges certain limitations:

- **Initial Topology Dependency**: The ILSTO method shows sensitivity to initial configurations, requiring careful normalization consideration during the initialization phase. This case is severe if multi-physics problems are considered.
- **Balancing Competing Objectives**: The combined thermo-mechanical optimization poses challenges in balancing conflicting requirements, necessitating further refinement of adaptive weighting strategies.
- **Ensuring the positive definiteness of the interpolation system:** When dealing with parametrized LSM, it is of great importance to be sure of the RBFs and the used kernels (See 4.4.2). Limitations of the positive definiteness of the RBF parametrization can cause ill-conditioning of the linear system when parametrizing the LS surface.

7.4 Future directions

Building on the findings of this research, several promising avenues for future work can be identified as detailed below.

1. **Experimental validation**: Even though numerical results of TO can be compared and validated with literature ones, physical prototyping and testing of optimized topologies will strengthen the practical applicability of the proposed methods.
2. **Artificial Intelligence (AI) integration**: AI and machine learning models, such as Machine Learning (ML), can aid in predicting optimal parameter settings and accelerating convergence. Many promising works build on convolutional neural networks are a great example in this field [107, 125]. However, due to its extreme nonlinear nature, topology optimization has yet a long journey to gain benefit from AI tools which need to be properly trained and tuned. Nevertheless, finding the best combination of the Lagrange Multipliers sounds promising as the convergence behavior of the solution relies heavily on these parameters, see 5.4 for more information.
3. **Multi-scale and multi-physics extensions**: Extending the ILSTO framework to include additional physics and multi-scale structures will expand its applicability. For instance, convectional heat problems,

radiational heat transfer problems, wave propagation and bandgap attenuation are a few examples that can be tackled with the current framework [59, 118, 242-244].

4. **Introducing nonlinear material models:** The material model for all the performed analyses was linear elastic; however, material models are often not linear in practice – such as the heat conduction coefficient which is typically temperature-dependent and the mechanical constitutive relationship of solids – and they can show an extremely nonlinear nature. Dealing with more practical real-world problems, such as optimized highly deformable structures used in soft robotics, requires the introduction of new material models and new solvers for the efficient applicability of the ILSTO framework [57, 244-246].

5. **Using other LS representation techniques:** Iso Geometric Analysis (IGA) is one of the new tools in representing physical boundaries [7]. The main advantage of redefining the problem by using this approach is the speed of solution which is faster than usual FEM. Also, the precise boundary description of IGA can facilitate the TO problems in general since the boundaries will not present the checkerboard problem [247, 248].

6. **Combining LSM and other TO methods**: Since bridging the LSM and other density-based models is feasible through CutFEM method, a new strategy would be implementing the current ILSTO method into a commercial density-based TO software such that real-world three-dimensional optimized parts can be obtained [249]. Integrating the LS-based methods with density-based TO methods is quite promising: an accurate optimized result can be achieved with a faster density-based method (often available in commercial FE packages) after a proper tuning with a LS approach.

7.5 Final remarks

This thesis bridges theoretical developments with practical applications, advancing the state of TO for structural and thermal systems. Combining innovative computational frameworks with rigorous numerical studies, it provides valuable insights into designing multi-functional, high-performance structures.

The proposed ILSTO framework opens opportunities for integration into commercial FEM software using a staggered-based approach. In this method, the LS-based topology evolution and FEM-based physical analyses operate iteratively in separate modules. Such decoupling ensures computational efficiency, enhances

boundary representation accuracy, and facilitates adaptability within existing platforms.

Furthermore, enabling users to define initial configurations interactively introduces practical constraints and desired features into the optimization process. Incorporating AI and ML tools could enhance this by predicting optimal initial conditions, improving convergence, and addressing real-world design challenges.

The versatility of ILSTO ensures its applicability beyond structural and thermal problems. With minor adjustments, it could address complex phenomena such as fluid dynamics, wave propagation, or multi-scale material design. Future developments may focus on nonlinear material behavior and real-time boundary adjustments for advanced applications like soft robotics and metamaterials.

In conclusion, ILSTO represents a transformative approach to TO, offering pathways to address increasingly complex design problems through its integration, interactivity, and flexibility. These advancements hold promises for both academic exploration and practical implementation in engineering and manufacturing.

References

1. Ashby, M.F., *The properties of foams and lattices.* Philosophical Transactions of the Royal Society A: Mathematical, Physical and Engineering Sciences, 2006. **364**(1838): p. 15-30.
2. Pan, C., Y. Han, and J. Lu, *Design and Optimization of Lattice Structures: A Review.* Applied Sciences, 2020. **10**(18): p. 6374.
3. Corkery, R.W. and E.C. Tyrode, *On the colour of wing scales in butterflies: iridescence and preferred orientation of single gyroid photonic crystals.* Interface focus, 2017. **7**(4): p. 20160154.
4. Chen, D., et al., *Functionally graded porous structures: Analyses, performances, and applications – A Review.* Thin-Walled Structures, 2023. **191**: p. 111046.
5. Chen, W., X. Su, and S. Liu, *Algorithms of isogeometric analysis for MIST-based structural topology optimization in MATLAB.* Structural and Multidisciplinary Optimization, 2024. **67**.
6. Ashby, M.F. and R.M. Medalist, *The mechanical properties of cellular solids.* Metallurgical Transactions A, 1983. **14**(9): p. 1755-1769.
7. Zhuang, C., Z. Xiong, and H. Ding, *Stress-related topology optimization with multilevel smoothed isogeometric densities and Bézier elements.* Computer Methods in Applied Mechanics and Engineering, 2023. **409**: p. 115974.
8. Kuci, E. and M. Jansen, *Level set topology optimization of elasto-plastic materials with local stress constraints.* Structural and Multidisciplinary Optimization, 2022. **65**.
9. Bourret, J., et al., *Effect of the pore volume fraction on the thermal conductivity and mechanical properties of kaolin-based foams.* Journal of the European Ceramic Society, 2013. **33**(9): p. 1487-1495.
10. Papadopoulos, A.M., *State of the art in thermal insulation materials and aims for future developments.* Energy and buildings, 2005. **37**(1): p. 77-86.
11. Zieliński, T.G., et al., *Reproducibility of sound-absorbing periodic porous materials using additive manufacturing technologies: Round robin study.* Additive Manufacturing, 2020. **36**: p. 101564.
12. Zieliński, T.G., *Generation of random microstructures and prediction of sound velocity and absorption for open foams with spherical pores.* The Journal of the Acoustical Society of America, 2015. **137**(4): p. 1790-1801.
13. Gibson, L.J. and M.F. Ashby, *Cellular Solids: Structure and Properties—Second Edition.* Published by the Press Syndicate of the University of Cambridge, 1997.
14. Hashin, Z. and S. Shtrikman, *A variational approach to the theory of the elastic behaviour of multiphase materials.* Journal of the Mechanics and Physics of Solids, 1963. **11**(2): p. 127-140.
15. Allaire, G. and R.V. Kohn, *Optimal bounds on the effective behavior of a mixture of two well-ordered elastic materials.* Quarterly of applied mathematics, 1993. **51**(4): p. 643-674.
16. Brighenti, R. and F. Tatar, *Thermo-mechanical performance of two-dimensional porous metamaterial plates.* International Journal of Mechanical Sciences, 2023. **238**: p. 107854.
17. Sigmund, O., *Design of material structures using topology optimization.* 1994, Technical University of Denmark Lyngby.
18. Dapogny, C. and F. Feppon, *Shape optimization using a level set based mesh evolution method: an overview and tutorial.* Comptes Rendus. Mathématique, 2023. **361**(G8): p. 1267-1332.
19. Gersborg-Hansen, A., M.P. Bendsøe, and O. Sigmund, *Topology optimization of heat conduction problems using the finite volume method.* Structural and multidisciplinary optimization, 2006. **31**: p. 251-259.

20. Lynch, M., et al., *Design, testing, and mechanical behavior of additively manufactured casing with optimized lattice structure.* Additive Manufacturing, 2018. **22**.
21. Wong, K.V. and A. Hernandez, *A review of additive manufacturing.* International scholarly research notices, 2012. **2012**.
22. Tan, L.J., W. Zhu, and K. Zhou, *Recent Progress on Polymer Materials for Additive Manufacturing.* Advanced Functional Materials, 2020. **30**(43): p. 2003062.
23. Shen, L., et al., *A novel metamaterial incorporating both auxeticity and thermal shrinkage.* International Journal of Mechanical Sciences, 2022. **233**: p. 107650.
24. Furth, M.E. and A. Atala, *Tissue engineering: future perspectives*, in *Principles of Tissue Engineering*. 2014, Elsevier. p. 83-123.
25. McClelland, R., et al., *7 - TISSUE ENGINEERING*, in *Introduction to Biomedical Engineering (Second Edition)*, J.D. Enderle, S.M. Blanchard, and J.D. Bronzino, Editors. 2005, Academic Press: Boston. p. 313-402.
26. Noroozi, R., et al., *Additively Manufactured Multi-Morphology Bone-like Porous Scaffolds: Experiments and Micro-Computed Tomography-Based Finite Element Modeling Approaches.* International Journal of Bioprinting, 2022. **8**(3).
27. Leong, K., et al., *Engineering functionally graded tissue engineering scaffolds.* Journal of the mechanical behavior of biomedical materials, 2008. **1**(2): p. 140-152.
28. Knight, A., *Cancer patient receives 3D printed ribs in worldfirst surgery.* Retrieved October, 2015. **3**: p. 2015.
29. Ali, D., et al., *Permeability and fluid flow-induced wall shear stress in bone scaffolds with TPMS and lattice architectures: A CFD analysis.* European Journal of Mechanics-B/Fluids, 2020. **79**: p. 376-385.
30. Castro, A., et al., *Numerical and experimental evaluation of TPMS Gyroid scaffolds for bone tissue engineering.* Computer methods in biomechanics and biomedical engineering, 2019. **22**(6): p. 567-573.
31. Castro, A.P., et al., *Micromechanical Behavior of TPMS Scaffolds for Bone Tissue Engineering.* Macromolecular Materials and Engineering, 2020. **305**(12): p. 2000487.
32. Pires, T., et al., *Numerical-experimental analysis of the permeability-porosity relationship in triply periodic minimal surfaces scaffolds.* Journal of Biomechanics, 2021. **117**: p. 110263.
33. Charbonnier, B., et al., *Custom-made macroporous bioceramic implants based on triply-periodic minimal surfaces for bone defects in load-bearing sites.* Acta biomaterialia, 2020. **109**: p. 254-266.
34. Al-Ketan, O., et al., *Forced convection computational fluid dynamics analysis of architected and three-dimensional printable heat sinks based on triply periodic minimal surfaces.* Journal of Thermal Science and Engineering Applications, 2021. **13**(2): p. 021010.
35. Vijayavenkataraman, S., et al., *Triply periodic minimal surfaces sheet scaffolds for tissue engineering applications: An optimization approach toward biomimetic scaffold design.* ACS Applied Bio Materials, 2018. **1**(2): p. 259-269.
36. Ma, S., et al., *Manufacturability, mechanical properties, mass-transport properties and biocompatibility of triply periodic minimal surface (TPMS) porous scaffolds fabricated by selective laser melting.* Materials & Design, 2020. **195**: p. 109034.
37. Song, K., et al., *Porous structure design and mechanical behavior analysis based on TPMS for customized root analogue implant.* Journal of the Mechanical Behavior of Biomedical Materials, 2021. **115**: p. 104222.
38. Al-Ketan, O., et al., *Functionally graded and multi-morphology sheet TPMS lattices: Design, manufacturing, and mechanical properties.* Journal of the mechanical behavior of biomedical materials, 2020. **102**: p. 103520.

39. Maskery, I., et al., *Insights into the mechanical properties of several triply periodic minimal surface lattice structures made by polymer additive manufacturing.* Polymer, 2018. **152**: p. 62-71.
40. Al-Ketan, O. and R.K. Abu Al-Rub, *Multifunctional mechanical metamaterials based on triply periodic minimal surface lattices.* Advanced Engineering Materials, 2019. **21**(10): p. 1900524.
41. Liao, B., et al., *3D-Printed Ti6Al4V Scaffolds with Graded Triply Periodic Minimal Surface Structure for Bone Tissue Engineering.* Journal of Materials Engineering and Performance, 2021: p. 1-12.
42. Restrepo, S., et al., *Mechanical properties of ceramic structures based on Triply Periodic Minimal Surface (TPMS) processed by 3D printing.* Journal of Physics: Conference Series, 2017. **935**: p. 012036.
43. Zhang, L., et al., *Topology-optimized lattice structures with simultaneously high stiffness and light weight fabricated by selective laser melting: Design, manufacturing and characterization.* Journal of Manufacturing Processes, 2020. **56**: p. 1166-1177.
44. Qiu, N., et al., *Mechanical performance of triply periodic minimal surface structures with a novel hybrid gradient fabricated by selective laser melting.* Engineering Structures, 2022. **263**: p. 114377.
45. Yang, L., et al., *Mechanical response of a triply periodic minimal surface cellular structures manufactured by selective laser melting.* International Journal of Mechanical Sciences, 2018. **148**: p. 149-157.
46. Qureshi, Z.A., et al., *Using triply periodic minimal surfaces (TPMS)-based metal foams structures as skeleton for metal-foam-PCM composites for thermal energy storage and energy management applications.* International Communications in Heat and Mass Transfer, 2021. **124**: p. 105265.
47. Strömberg, N., *A GAME FOR MULTI-SCALE TOPOLOGY OPTIMIZATION OF STATIC AND DYNAMIC COMPLIANCES OF TPMS-BASED LATTICE STRUCTURES.* 2023.
48. Deshpande, V.S., M.F. Ashby, and N.A. Fleck, *Foam topology: bending versus stretching dominated architectures.* Acta Materialia, 2001. **49**: p. 1035-1040.
49. Zhang, H., et al., *Extensible beam-like metastructures at the microscale: Theoretical and modified Hencky bar-chain modeling.* International Journal of Mechanical Sciences, 2020. **180**: p. 105636.
50. Liu, Y. and X. Zhang, *Metamaterials: a new frontier of science and technology.* Chemical Society Reviews, 2011. **40**(5): p. 2494-2507.
51. Engheta, N. and R.W. Ziolkowski, *Metamaterials: physics and engineering explorations*. 2006: John Wiley & Sons.
52. Bertoldi, K., et al., *Flexible mechanical metamaterials.* Nature Reviews Materials, 2017. **2**(11): p. 1-11.
53. Lyu, S., et al., *Origami-based cellular mechanical metamaterials with tunable Poisson's ratio: Construction and analysis.* International Journal of Mechanical Sciences, 2021. **212**: p. 106791.
54. Hu, J., et al., *Superior compressive properties of 3D printed plate lattice mechanical metamaterials.* International Journal of Mechanical Sciences, 2022. **231**: p. 107586.
55. Liang, E., et al., *Negative thermal expansion: Mechanisms and materials.* Frontiers of Physics, 2021. **16**(5): p. 53302.
56. Surjadi, J.U., et al., *Mechanical metamaterials and their engineering applications.* Advanced Engineering Materials, 2019. **21**(3): p. 1800864.
57. Chen, Y., B. Ai, and Z.J. Wong, *Soft optical metamaterials.* Nano Convergence, 2020. **7**(1): p. 1-17.
58. Fan, B., et al., *Magneto-optical metamaterials: nonreciprocal transmission and Faraday effect enhancement.* Advanced Optical Materials, 2019. **7**(14): p. 1801420.

59. Gorshkov, V., et al., *Acoustic metamaterials with controllable bandgap gates based on magnetorheological elastomers.* International Journal of Mechanical Sciences, 2022. **238**: p. 107829.
60. Gao, N., et al., *Acoustic Metamaterials for Noise Reduction: A Review.* Advanced Materials Technologies, 2022. **7**(6): p. 2100698.
61. Roh, Y., et al., *Terahertz imaging with metamaterials for biological applications.* Sensors and Actuators B: Chemical, 2022. **352**: p. 130993.
62. Della Giovampaola, C. and N. Engheta, *Digital metamaterials.* Nature Materials, 2014. **13**(12): p. 1115-1121.
63. Zadpoor, A.A., *Meta-biomaterials.* Biomaterials science, 2020. **8**(1): p. 18-38.
64. Deshmukh, S., et al., *Selection of periodic cellular structures for multifunctional applications directly based on their unit cell geometry.* International Journal of Mechanical Sciences, 2022. **220**: p. 107133.
65. Bertolino, G. and M. Montemurro, *Two-scale topology optimisation of cellular materials under mixed boundary conditions.* International Journal of Mechanical Sciences, 2022. **216**: p. 106961.
66. Sklan, S.R. and B. Li, *Thermal metamaterials: functions and prospects.* National Science Review, 2018. **5**(2): p. 138-141.
67. Yang, S., et al., *Controlling macroscopic heat transfer with thermal metamaterials: theory, experiment and application.* Physics Reports, 2021. **908**: p. 1-65.
68. Dai, G.-L., *Designing nonlinear thermal devices and metamaterials under the Fourier law: A route to nonlinear thermotics.* Frontiers of Physics, 2021. **16**(5): p. 53301.
69. Narayana, S., S. Savo, and Y. Sato, *Transient heat flux shielding using thermal metamaterials.* Applied Physics Letters, 2013. **102**.
70. Han, T., et al., *Manipulating Steady Heat Conduction by Sensu-shaped Thermal Metamaterials.* Scientific Reports, 2015. **5**(1): p. 10242.
71. Hamzehei, R., M. Bodaghi, and N. Wu, *Mastering the art of designing mechanical metamaterials with quasi-zero stiffness for passive vibration isolation: a review.* Smart Materials and Structures, 2024. **33**(8): p. 083001.
72. Wang, J., G. Dai, and J. Huang, *Thermal metamaterial: fundamental, application, and outlook.* Iscience, 2020. **23**(10): p. 101637.
73. Hu, R., et al., *Machine-Learning-Optimized Aperiodic Superlattice Minimizes Coherent Phonon Heat Conduction.* Physical Review X, 2020. **10**(2).
74. Narayana, S. and Y. Sato, *Heat flux manipulation with engineered thermal materials.* Physical review letters, 2012. **108**(21): p. 214303.
75. Vemuri, K., F. Canbazoglu, and P. Bandaru, *Guiding conductive heat flux through thermal metamaterials.* Applied Physics Letters, 2014. **105**: p. 193904.
76. Li, Y., et al., *Transforming heat transfer with thermal metamaterials and devices.* Nature Reviews Materials, 2021. **6**(6): p. 488-507.
77. Álvarez Hostos, J.C., V.D. Fachinotti, and I. Peralta, *Computational design of thermo-mechanical metadevices using topology optimization.* Applied Mathematical Modelling, 2021. **90**: p. 758-776.
78. Peralta, I., V.D. Fachinotti, and J.C. Alvarez Hostos, *A brief review on thermal metamaterials for cloaking and heat flux manipulation.* Advanced Engineering Materials, 2020. **22**(2): p. 1901034.
79. Zhang, Q., et al., *High-efficient heat flux manipulation of micro-scale thermal metamaterials with facile functional unit design.* Materials & Design, 2021. **204**: p. 109657.
80. Wang, K.X., et al., *An efficient and accurate numerical method for the heat conduction problems of thermal metamaterials based on edge-based smoothed finite element method.* Engineering Analysis with Boundary Elements, 2022. **134**: p. 282-297.

81. Alitalo, P. and S. Tretyakov, *Electromagnetic Cloaking With Metamaterials.* Materials Today, 2009. **12**.
82. Hu, R., et al., *Thermal camouflaging metamaterials.* Materials Today, 2021. **45**: p. 120-141.
83. Li, J., X. Wen, and P. Sheng, *Acoustic metamaterials.* Journal of Applied Physics, 2021. **129**(17).
84. Matlack, K.H., et al., *Designing perturbative metamaterials from discrete models.* Nature materials, 2018. **17**(4): p. 323-328.
85. Li, W., G. Yu, and Z. Yu, *Bioinspired heat exchangers based on triply periodic minimal surfaces for supercritical CO2 cycles.* Applied Thermal Engineering, 2020. **179**: p. 115686.
86. Dou, N.G., et al., *Ultralow thermal conductivity and mechanical resilience of architected nanolattices.* Nano Letters, 2018. **18**(8): p. 4755-4761.
87. Chen, Y., Z. Jia, and L. Wang, *Hierarchical honeycomb lattice metamaterials with improved thermal resistance and mechanical properties.* Composite structures, 2016. **152**: p. 395-402.
88. Gong, L., et al., *Thermal conductivity of highly porous mullite materials.* International Journal of Heat and Mass Transfer, 2013. **67**: p. 253-259.
89. Pabst, W., et al., *Young's modulus and thermal conductivity of model materials with convex or concave pores – from analytical predictions to numerical results.* Journal of the European Ceramic Society, 2018. **38**(7): p. 2694-2707.
90. Collishaw, P.G. and J.R.G. Evans, *An assessment of expressions for the apparent thermal conductivity of cellular materials.* Journal of Materials Science, 1994. **29**(9): p. 2261-2273.
91. Carson, J.K., et al., *Thermal conductivity bounds for isotropic, porous materials.* International Journal of Heat and Mass Transfer, 2005. **48**(11): p. 2150-2158.
92. Coble, R. and W. Kingery, *Effect of porosity on physical properties of sintered alumina.* Journal of the American Ceramic Society, 1956. **39**(11): p. 377-385.
93. Sobieski, W., *Waterfall Algorithm as a tool of investigation the geometrical features of granular porous media.* Computational Particle Mechanics, 2022. **9**(3): p. 551-567.
94. Kegl, M., B. Butinar, and B. Kegl, *An efficient gradient-based optimization algorithm for mechanical systems.* Communications in Numerical Methods in Engineering, 2002. **18**: p. 363-371.
95. Eschenauer , H.A. and N. Olhoff *Topology optimization of continuum structures: A review*.* Applied Mechanics Reviews, 2001. **54**(4): p. 331-390.
96. Nocedal, J., & Wright, S. J., *Numerical optimization.* Second ed, ed. S.S.i.O.R.a.F. Engineering). 2006, Berlin: Springer Nature.
97. Zhu, J.-H., W.-H. Zhang, and L. Xia, *Topology optimization in aircraft and aerospace structures design.* Archives of computational methods in engineering, 2016. **23**: p. 595-622.
98. Svanberg, K., *MMA and GCMMA-two methods for nonlinear optimization.* vol, 2007. **1**: p. 1-15.
99. Gao, J., et al., *A comprehensive review of isogeometric topology optimization: methods, applications and prospects.* Chinese Journal of Mechanical Engineering, 2020. **33**: p. 1-14.
100. Ferreira, R., et al., *Combination of topology and shape optimization with finite element modeling in the case of an aerospace component produced by laser based additive manufacturing.* Journal of Laser Applications, 2023. **35**(2).
101. Zhao, N., et al., *Direct additive manufacturing of metal parts for automotive applications.* Journal of Manufacturing Systems, 2023. **68**: p. 368-375.

102. Chandrasekhar, A., S. Sridhara, and K. Suresh, *AuTO: a framework for Automatic differentiation in Topology Optimization.* Structural and Multidisciplinary Optimization, 2021. **64**(6): p. 4355-4365.
103. Bi, M., et al., *Topology optimization for 3D concrete printing with various manufacturing constraints.* Additive Manufacturing, 2022. **57**: p. 102982.
104. Wu, J., et al., *Infill optimization for additive manufacturing—approaching bone-like porous structures.* IEEE transactions on visualization and computer graphics, 2017. **24**(2): p. 1127-1140.
105. Kollmann, H.T., et al., *Deep learning for topology optimization of 2D metamaterials.* Materials & Design, 2020. **196**: p. 109098.
106. He, Z., et al., *A physics-informed deep learning method for solving direct and inverse heat conduction problems of materials.* Materials Today Communications, 2021. **28**: p. 102719.
107. Wang, L., et al., *Deep learning driven real time topology optimization based on improved convolutional block attention (Cba-U-Net) model.* Engineering Analysis with Boundary Elements, 2023. **147**: p. 112-124.
108. Wang, Y., J.E. Kim, and K. Suresh, *Opportunities and Challenges of Quantum Computing for Engineering Optimization.* Journal of Computing and Information Science in Engineering, 2023. **23**(6).
109. Wu, J., et al., *A CAD-oriented parallel-computing design framework for shape and topology optimization of arbitrary structures using parametric level set.* Computer Methods in Applied Mechanics and Engineering, 2024. **431**: p. 117292.
110. Liu, S., X. An, and H. Jia, *Topology optimization of beam cross-section considering warping deformation.* Structural and Multidisciplinary Optimization, 2008. **35**: p. 403-411.
111. da Silva, G.A., A.T. Beck, and O. Sigmund, *Stress-constrained topology optimization considering uniform manufacturing uncertainties.* Computer Methods in Applied Mechanics and Engineering, 2019. **344**: p. 512-537.
112. Alekseev, G.V. and D.A. Tereshko, *Particle swarm optimization-based algorithms for solving inverse problems of designing thermal cloaking and shielding devices.* International Journal of Heat and Mass Transfer, 2019. **135**: p. 1269-1277.
113. Fujii, G. and Y. Akimoto, *Optimizing the structural topology of bifunctional invisible cloak manipulating heat flux and direct current.* Applied Physics Letters, 2019. **115**(17): p. 174101.
114. Fujii, G., Y. Akimoto, and M. Takahashi, *Exploring optimal topology of thermal cloaks by CMA-ES.* Applied Physics Letters, 2018. **112**(6): p. 061108.
115. Ikonen, T., et al., *Topology optimization of conductive heat transfer problems using parametric L-systems.* Structural and Multidisciplinary Optimization, 2018. **58**.
116. Kambampati, S., J. Gray, and H. Kim, *Level Set Topology Optimization of Load Carrying Heat Exchangers*. 2020.
117. Li, Q., et al., *Shape and topology design for heat conduction by Evolutionary Structural Optimization.* International Journal of Heat and Mass Transfer, 1999. **42**(17): p. 3361-3371.
118. Coffin, P. and K. Maute, *Level set topology optimization of cooling and heating devices using a simplified convection model.* Structural and Multidisciplinary Optimization, 2016. **53**(5): p. 985-1003.
119. Kang, Z., et al., *A method using successive iteration of analysis and design for large-scale topology optimization considering eigenfrequencies.* Computer Methods in Applied Mechanics and Engineering, 2020. **362**: p. 112847.
120. Campbell, S.D., et al., *Review of numerical optimization techniques for meta-device design [Invited].* Optical Materials Express, 2019. **9**(4): p. 1842-1863.

121. Wu, N., et al., *The advances of topology optimization techniques in orthopedic implants: A review.* Medical & Biological Engineering & Computing, 2021. **59**(9): p. 1673-1689.
122. Allaire, G., C. Dapogny, and F. Jouve, *Chapter 1 - Shape and topology optimization*, in *Handbook of Numerical Analysis*, A. Bonito and R.H. Nochetto, Editors. 2021, Elsevier. p. 1-132.
123. Bendsøe, M.P., *Optimization of structural topology, shape, and material.* Vol. 414. 1995: Springer.
124. Bendsoe, M.P. and O. Sigmund, *Topology optimization: theory, methods, and applications*. 2013: Springer Science & Business Media.
125. Bujny, M., *Level set topology optimization for crashworthiness using evolutionary algorithms and machine learning.* 2020, Technische Universität München.
126. Deaton, J.D. and R.V. Grandhi, *A survey of structural and multidisciplinary continuum topology optimization: post 2000.* Structural and Multidisciplinary Optimization, 2014. **49**(1): p. 1-38.
127. Gaynor, A.T. and J.K. Guest, *Topology optimization considering overhang constraints: Eliminating sacrificial support material in additive manufacturing through design.* Structural and Multidisciplinary Optimization, 2016. **54**(5): p. 1157-1172.
128. Li, H., et al., *Topology optimization for functionally graded cellular composites with metamaterials by level sets.* Computer Methods in Applied Mechanics and Engineering, 2018. **328**: p. 340-364.
129. Ogawa, S. and T. Yamada, *Topology optimization for transient thermomechanical coupling problems.* Applied Mathematical Modelling, 2022. **109**: p. 536-554.
130. Pizzolato, A., et al., *Multi-scale topology optimization of multi-material structures with controllable geometric complexity — Applications to heat transfer problems.* Computer Methods in Applied Mechanics and Engineering, 2019. **357**: p. 112552.
131. Rodrigues, H., C.A. Soto, and J.E. Taylor, *A design model to predict optimal two-material composite structures.* Structural optimization, 1999. **17**(2): p. 186-198.
132. Rozvany, G.I., *A critical review of established methods of structural topology optimization.* Structural and multidisciplinary optimization, 2009. **37**(3): p. 217-237.
133. Sigmund, O. and K. Maute, *Topology optimization approaches.* Structural and Multidisciplinary Optimization, 2013. **48**(6): p. 1031-1055.
134. Yamada, T., et al., *A topology optimization method based on the level set method incorporating a fictitious interface energy.* Computer Methods in Applied Mechanics and Engineering, 2010. **199**(45): p. 2876-2891.
135. Zhuang, C., Z. Xiong, and H. Ding, *Topology optimization of multi-material for the heat conduction problem based on the level set method.* Engineering Optimization, 2010. **42**(9): p. 811-831.
136. van Dijk, N.P., et al., *Level-set methods for structural topology optimization: a review.* Structural and Multidisciplinary Optimization, 2013. **48**(3): p. 437-472.
137. Hassani, V., et al., *A Comparison between Parametric Structural Optimization Methods and Software-Based Topology Optimization of A Rectangular Sample Under Tensile Load for Additive Manufacturing Processes.* 2021.
138. Allaire, G., et al., *Structural optimization under overhang constraints imposed by additive manufacturing technologies.* Journal of Computational Physics, 2017. **351**: p. 295-328.
139. Michell, A.G.M., *LVIII. The limits of economy of material in frame-structures.* The London, Edinburgh, and Dublin Philosophical Magazine and Journal of Science, 1904. **8**(47): p. 589-597.

140. Sigmund, O. and J. Petersson, *Numerical instabilities in topology optimization: a survey on procedures dealing with checkerboards, mesh-dependencies and local minima.* Structural optimization, 1998. **16**: p. 68-75.
141. Querin, O.M., G.P. Steven, and Y.M. Xie, *Evolutionary structural optimisation (ESO) using a bidirectional algorithm.* Engineering computations, 1998. **15**(8): p. 1031-1048.
142. Xie, Y.M. and G.P. Steven, *A simple evolutionary procedure for structural optimization.* Computers & Structures, 1993. **49**(5): p. 885-896.
143. Sethian, J.A., *Evolution, implementation, and application of level set and fast marching methods for advancing fronts.* Journal of computational physics, 2001. **169**(2): p. 503-555.
144. Allaire, G., F. Jouve, and A.-M. Toader, *A level-set method for shape optimization.* Comptes Rendus Mathematique, 2002. **334**(12): p. 1125-1130.
145. Wang, M., X. Wang, and D. Guo, *A level set method for structural topology optimization.* Computer Methods in Applied Mechanics and Engineering, 2003. **192**: p. 227-246.
146. Amstutz, S. and H. Andrä, *A new algorithm for topology optimization using a level-set method.* Journal of Computational Physics, 2006. **216**(2): p. 573-588.
147. Challis, V.J., *A discrete level-set topology optimization code written in Matlab.* Structural and Multidisciplinary Optimization, 2010. **41**(3): p. 453-464.
148. Yamasaki, S., et al., *A level set based topology optimization method using the discretized signed distance function as the design variables.* Structural and Multidisciplinary Optimization, 2010. **41**: p. 685-698.
149. Shojaee, S., M. Mohamadian, and N. Valizadeh, *Composition of isogeometric analysis with level set method for structural topology optimization.* Int J Optim Civil Eng, 2012. **2**(1): p. 47-70.
150. Sokolowski, J. and A. Zochowski, *On the topological derivative in shape optimization.* SIAM journal on control and optimization, 1999. **37**(4): p. 1251-1272.
151. Bourdin, B. and A. Chambolle, *Design-dependent loads in topology optimization.* ESAIM: Control, Optimisation and Calculus of Variations, 2003. **9**: p. 19-48.
152. Young, V., et al., *3D and multiple load case bi-directional evolutionary structural optimization (BESO).* Structural optimization, 1999. **18**: p. 183-192.
153. Andreasen, C.S., M.O. Elingaard, and N. Aage, *Level set topology and shape optimization by density methods using cut elements with length scale control.* Structural and Multidisciplinary Optimization, 2020. **62**: p. 685-707.
154. Abdi, M., I. Ashcroft, and R. Wildman, *Topology optimization of geometrically nonlinear structures using an evolutionary optimization method.* Engineering Optimization, 2017.
155. Wang, Y., et al., *Open-Source Codes of Topology Optimization: A Summary for Beginners to Start Their Research.* Computer Modeling in Engineering & Sciences, 2023. **137**: p. 1-34.
156. Andreassen, E., et al., *Efficient topology optimization in MATLAB using 88 lines of code.* Structural and Multidisciplinary Optimization, 2011. **43**(1): p. 1-16.
157. Sigmund, O., *A 99 line topology optimization code written in Matlab.* Structural and Multidisciplinary Optimization, 2001. **21**(2): p. 120-127.
158. Duysinx, P. and O. Sigmund. *New developments in handling stress constraints in optimal material distribution.* in *7th AIAA/USAF/NASA/ISSMO symposium on multidisciplinary analysis and optimization*. 1998.

159. Rossow, M. and J. Taylor, *A finite element method for the optimal design of variable thickness sheets.* Aiaa Journal, 1973. **11**(11): p. 1566-1569.
160. Haber, R.B., C.S. Jog, and M.P. Bendsøe, *A new approach to variable-topology shape design using a constraint on perimeter.* Structural optimization, 1996. **11**: p. 1-12.
161. Poulsen, T.A., *A simple scheme to prevent checkerboard patterns and one-node connected hinges in topology optimization.* Structural and Multidisciplinary Optimization, 2002. **24**: p. 396-399.
162. Tyflopoulos, E. and M. Steinert, *A Comparative Study of the Application of Different Commercial Software for Topology Optimization.* Applied Sciences, 2022. **12**(2): p. 611.
163. Ansys. *TO example*. 2024; Available from: https://www.ansys.com/applications/topology-optimization#tab1-3.
164. SOLIDWORKS. *TO example*. 2024; Available from: https://www.solidworks.com/.
165. NX, S. *TO example*. 2024; Available from: https://plm.sw.siemens.com/en-US/nx/.
166. nTop. *TO example*. 2024; Available from: https://www.ntop.com/software/capabilities/topology-optimization/.
167. COMSOL. *TO example*. 2024; Available from: https://www.comsol.com/.
168. Papanicolau, G., A. Bensoussan, and J.-L. Lions, *Asymptotic analysis for periodic structures*. 1978: Elsevier.
169. Sánchez-Palencia, E., *Non-homogeneous media and vibration theory.* Lecture Note in Physics, Springer-Verlag, 1980. **320**: p. 57-65.
170. Bendsøe, M.P. and N. Kikuchi, *Generating optimal topologies in structural design using a homogenization method.* Computer Methods in Applied Mechanics and Engineering, 1988. **71**(2): p. 197-224.
171. Allaire, G. and R. Kohn, *Topology optimization and optimal shape design using homogenization.* Topology design of structures, 1993: p. 207-218.
172. Bendsøe, M.P., A. Díaz, and N. Kikuchi, *Topology and generalized layout optimization of elastic structures.* Topology design of structures, 1993. **227**: p. 159-206.
173. Wu, J., O. Sigmund, and J.P. Groen, *Topology optimization of multi-scale structures: a review.* Structural and Multidisciplinary Optimization, 2021. **63**(3): p. 1455-1480.
174. Bendsøe, M.P., *Optimal shape design as a material distribution problem.* Structural Optimization, 1989. **1**(4): p. 193-202.
175. Zhou, M. and G. Rozvany, *The COC algorithm, Part II: Topological, geometrical and generalized shape optimization.* Computer methods in applied mechanics and engineering, 1991. **89**(1-3): p. 309-336.
176. Mlejnek, H.P., *Some aspects of the genesis of structures.* Structural optimization, 1992. **5**(1): p. 64-69.
177. Sigmund, O., *Materials with prescribed constitutive parameters: An inverse homogenization problem.* International Journal of Solids and Structures, 1994. **31**(17): p. 2313-2329.
178. Wu, W., et al., *Mechanical design and multifunctional applications of chiral mechanical metamaterials: A review.* Materials & Design, 2019. **180**: p. 107950.
179. Vogiatzis, P., et al., *Topology optimization of multi-material negative Poisson's ratio metamaterials using a reconciled level set method.* Computer-Aided Design, 2016. **83**.
180. Zhang, H., et al., *Multiscale topology optimization of biodegradable metal matrix composite structures for additive manufacturing.* Applied Mathematical Modelling, 2023. **114**: p. 799-822.
181. Das, S. and A. Sutradhar, *Multi-physics topology optimization of functionally graded controllable porous structures: Application to heat dissipating problems.* Materials & Design, 2020. **193**: p. 108775.

182. Chen, H., et al., *Design of Locally Resonant Acoustic Metamaterials with Specified Band Gaps Using Multi-Material Topology Optimization.* Materials, 2024. **17**: p. 3591.
183. Gao, J., et al., *Topology optimization for multiscale design of porous composites with multi-domain microstructures.* Computer Methods in Applied Mechanics and Engineering, 2019. **344**: p. 451-476.
184. Osher, S. and J.A. Sethian, *Fronts propagating with curvature-dependent speed: Algorithms based on Hamilton-Jacobi formulations.* Journal of computational physics, 1988. **79**(1): p. 12-49.
185. Osher, S.J. and F. Santosa, *Level Set Methods for Optimization Problems Involving Geometry and Constraints: I. Frequencies of a Two-Density Inhomogeneous Drum.* Journal of Computational Physics, 2001. **171**(1): p. 272-288.
186. Osher, S., R. Fedkiw, and K. Piechor, *Level set methods and dynamic implicit surfaces.* Appl. Mech. Rev., 2004. **57**(3): p. B15-B15.
187. Belytschko, T., S. Xiao, and C. Parimi, *Topology optimization with implicit functions and regularization.* International Journal for Numerical Methods in Engineering, 2003. **57**: p. 1177-1196.
188. Liu, Z., J.G. Korvink, and R. Huang, *Structure topology optimization: fully coupled level set method via FEMLAB.* Structural and Multidisciplinary Optimization, 2005. **29**: p. 407-417.
189. Liu, H., S. Osher, and R. Tsai, *Multi-valued solution and level set methods in computational high frequency wave propagation.* Communications in computational physics, 2006. **1**(5): p. 765-804.
190. Allaire, G., et al., *Multi-phase structural optimization via a level set method.* ESAIM: Control, Optimisation and Calculus of Variations, 2014. **20**(2): p. 576-611.
191. Zhao, H.-K., et al., *A Variational Level Set Approach to Multiphase Motion.* Journal of Computational Physics, 1996. **127**(1): p. 179-195.
192. Malladi, R. and J.A. Sethian. *Level set and fast marching methods in image processing and computer vision.* in *Proceedings of 3rd IEEE International Conference on Image Processing*. 1996.
193. Chopp, D.L., *Computing minimal surfaces via level set curvature flow.* 1991.
194. Allaire, G., C. Dapogny, and P. Frey, *Shape optimization with a level set based mesh evolution method.* Computer Methods in Applied Mechanics and Engineering, 2014. **282**: p. 22-53.
195. Allaire, G., F. Jouve, and G. Michailidis, *Thickness control in structural optimization via a level set method.* Structural and Multidisciplinary Optimization, 2016. **53**(6): p. 1349-1382.
196. Valance, S., et al., *A partition-of-unity-based finite element method for level sets.* International journal for numerical methods in engineering, 2008. **76**(10): p. 1513-1527.
197. Wei, P. and G.H. Paulino, *A parameterized level set method combined with polygonal finite elements in topology optimization.* Structural and Multidisciplinary Optimization, 2020. **61**(5): p. 1913-1928.
198. Eschenauer, H.A., V.V. Kobelev, and A. Schumacher, *Bubble method for topology and shape optimization of structures.* Structural optimization, 1994. **8**: p. 42-51.
199. Wei, P., et al., *An 88-line MATLAB code for the parameterized level set method based topology optimization using radial basis functions.* Structural and Multidisciplinary Optimization, 2018. **58**(2): p. 831-849.
200. Allaire, G. and O. Pantz, *Structural optimization with FreeFEM++.* Structural and Multidisciplinary Optimization, 2006. **32**(3): p. 173-181.
201. Otomori, M., et al., *Matlab code for a level set-based topology optimization method using a reaction diffusion equation.* Structural and Multidisciplinary Optimization, 2015. **51**(5): p. 1159-1172.

202. Laurain, A., *A level set-based structural optimization code using FEniCS.* Structural and Multidisciplinary Optimization, 2018. **58**(3): p. 1311-1334.
203. Kambampati, S., et al. *OpenLSTO: Open-source software for level set topology optimization.* in *2018 Multidisciplinary Analysis and Optimization Conference*. 2018.
204. Yaghmaei, M., A. Ghoddosian, and M.M. Khatibi, *A filter-based level set topology optimization method using a 62-line MATLAB code.* Structural and Multidisciplinary Optimization, 2020. **62**(2): p. 1001-1018.
205. Wang, Y. and Z. Kang, *MATLAB implementations of velocity field level set method for topology optimization: an 80-line code for 2D and a 100-line code for 3D problems.* Structural and Multidisciplinary Optimization, 2021. **64**(6): p. 4325-4342.
206. Sethian, J.A., *Fast marching methods.* SIAM review, 1999. **41**(2): p. 199-235.
207. Allaire, G., F. Jouve, and A.-M. Toader, *Structural optimization using sensitivity analysis and a level-set method.* Journal of computational physics, 2004. **194**(1): p. 363-393.
208. Karrman, A.M.B. and G. Allaire, *Structural optimization using sensitivity analysis and a level-set method, in Scilab and Matlab.* 2009.
209. Wang, M.Y. and X. Wang. *PDE-Driven Level Sets and Shape Sensitivity for Structural Topology Optimization.* in *International Design Engineering Technical Conferences and Computers and Information in Engineering Conference*. 2004.
210. Wang, S. and M.Y. Wang, *Radial basis functions and level set method for structural topology optimization.* International journal for numerical methods in engineering, 2006. **65**(12): p. 2060-2090.
211. Liu, Y., et al., *Parameterized level-set based topology optimization method considering symmetry and pattern repetition constraints.* Computer Methods in Applied Mechanics and Engineering, 2018. **340**: p. 1079-1101.
212. Deng, S. and K. Suresh, *Multi-constrained topology optimization via the topological sensitivity.* Structural and Multidisciplinary Optimization, 2015. **51**: p. 987-1001.
213. Li, H., et al., *A level set method for topological shape optimization of 3D structures with extrusion constraints.* Computer Methods in Applied Mechanics and Engineering, 2015. **283**: p. 615-635.
214. Kim, C., et al., *Freefem++ code for reaction-diffusion equation–based topology optimization: for high-resolution boundary representation using adaptive mesh refinement.* Structural and Multidisciplinary Optimization, 2020. **62**(1): p. 439-455.
215. Li, H., et al., *Full-scale 3D structural topology optimization using adaptive mesh refinement based on the level-set method.* Finite Elements in Analysis and Design, 2021. **194**: p. 103561.
216. Wang, C., et al., *A reaction diffusion-based B-spline level set (RDBLS) method for structural topology optimization.* Computer Methods in Applied Mechanics and Engineering, 2022. **398**: p. 115252.
217. Dunning, P.D. and H.A. Kim, *Introducing the sequential linear programming level-set method for topology optimization.* Structural and Multidisciplinary Optimization, 2015. **51**(3): p. 631-643.
218. Bujny, M., et al. *Evolutionary level set method for crashworthiness topology optimization.* in *ECCOMAS Congress*. 2016.
219. Wu, J., et al., *Level-set topology optimization for mechanical metamaterials under hybrid uncertainties.* Computer Methods in Applied Mechanics and Engineering, 2017. **319**: p. 414-441.
220. Kambampati, S., J.S. Gray, and H. Alicia Kim, *Level set topology optimization of structures under stress and temperature constraints.* Computers & Structures, 2020. **235**: p. 106265.

221. Kambampati, S., J. Gray, and H.A. Kim, *Level set topology optimization of load carrying battery packs.* International Journal of Heat and Mass Transfer, 2021. **177**: p. 121570.
222. Salazar De Troya, M.A., D.A. Tortorelli, and V.A. Beck. *Two dimensional topology optimization of heat exchangers with the density and level-set methods*. in *WCCM-ECCOMAS Congress*. 2021. Lawrence Livermore National Lab.(LLNL), Livermore, CA (United States).
223. Luo, J.-W., et al., *Topology optimization of thermal cloak using the adjoint lattice Boltzmann method and the level-set method.* Applied Thermal Engineering, 2022. **216**: p. 119103.
224. Boyd, S. and L. Vandenberghe, *Convex optimization*. 2004: Cambridge university press.
225. Wang, W., et al., *Regularization in space–time topology optimization for additive manufacturing.* Computer Methods in Applied Mechanics and Engineering, 2024. **431**: p. 117202.
226. Verbart, A., M. Langelaar, and F.v. Keulen, *A unified aggregation and relaxation approach for stress-constrained topology optimization.* Structural and Multidisciplinary Optimization, 2017. **55**: p. 663-679.
227. Marco, O., et al., *Exact 3D boundary representation in finite element analysis based on Cartesian grids independent of the geometry.* International Journal for Numerical Methods in Engineering, 2015. **103**(6): p. 445-468.
228. Wu, C., et al., *Level-set topology optimization for maximizing fracture resistance of brittle materials using phase-field fracture model.* International Journal for Numerical Methods in Engineering, 2020. **121**(13): p. 2929-2945.
229. Sethian, J.A. and P. Smereka, *Level set methods for fluid interfaces.* Annual review of fluid mechanics, 2003. **35**(1): p. 341-372.
230. Sethian, J.A. and J. Straint, *Crystal growth and dendritic solidification.* Journal of Computational Physics, 1992. **98**(2): p. 231-253.
231. Allaire, G., et al., *Structural optimization using topological and shape sensitivity via a level set method.* Control and cybernetics, 2005. **34**(1): p. 59-80.
232. Luo, Z., et al., *A level set-based parameterization method for structural shape and topology optimization.* International Journal for Numerical Methods in Engineering, 2008. **76**: p. 1-26.
233. Wang, M.Y. and P. Wei. *Topology optimization with level set method incorporating topological derivative*. in *6th World Congress on Structural and Multidisciplinary Optimization*. 2005. Citeseer.
234. Guo, Z., X. Cheng, and Z. Xia, *Least dissipation principle of heat transport potential capacity and its application in heat conduction optimization.* Chinese science bulletin, 2003. **48**(4): p. 406-410.
235. de Kruijf, N., et al., *Topological design of structures and composite materials with multiobjectives.* International Journal of Solids and Structures, 2007. **44**(22): p. 7092-7109.
236. Lohan, D.J., E.M. Dede, and J.T. Allison, *Topology optimization for heat conduction using generative design algorithms.* Structural and Multidisciplinary Optimization, 2017. **55**: p. 1063-1077.
237. Lee, G., Y. Joo, and S.J. Kim, *On the Objective Function for Topology Optimization of Heat Sinks.* IEEE Transactions on Components, Packaging and Manufacturing Technology, 2021. **11**(11): p. 1776-1782.
238. Deng, S. and K. Suresh, *Multi-constrained 3D topology optimization via augmented topological level-set.* Computers & Structures, 2016. **170**: p. 1-12.
239. Sigmund, O., *On benchmarking and good scientific practise in topology optimization.* Structural and Multidisciplinary Optimization, 2022. **65**(11): p. 315.

240. Chen, W., Y. Zheng, and Y. Wang, *Multi-objective topology optimization filled with multiple microstructures.* Composite Structures, 2023. **304**: p. 116322.
241. Yan, X., et al., *Two-scale optimal design of structures with thermal insulation materials.* Composite Structures, 2015. **120**: p. 358-365.
242. Manconi, E., B.R. Mace, and R. Garziera, *Wave propagation in laminated cylinders with internal fluid and residual stress.* Applied Sciences, 2023. **13**(9): p. 5227.
243. Dai, G. and J. Huang, *A transient regime for transforming thermal convection: Cloaking, concentrating, and rotating creeping flow and heat flux.* Journal of Applied Physics, 2018. **124**(23): p. 235103.
244. Shintake, J., et al., *Soft robotic grippers.* Advanced materials, 2018. **30**(29): p. 1707035.
245. Xavier, M.S., et al., *Soft Pneumatic Actuators: A Review of Design, Fabrication, Modeling, Sensing, Control and Applications.* IEEE Access, 2022. **10**: p. 59442-59485.
246. Hamed, E. and Y. Frostig, *Nonlinear thermo-mechanical behaviour of soft core sandwich panels–Creep effects.* Journal of Sandwich Structures & Materials, 2020. **22**(8): p. 2629-2654.
247. Qian, X., *Full analytical sensitivities in NURBS based isogeometric shape optimization.* Computer Methods in Applied Mechanics and Engineering, 2010. **199**(29): p. 2059-2071.
248. Qian, X., *Full analytical sensitivities in NURBS based isogeometric shape optimization.* Computer Methods in Applied Mechanics and Engineering, 2010. **199**(29-32): p. 2059-2071.
249. Aage, N., R. Giele, and C.S. Andreasen, *Length scale control for high-resolution three-dimensional level set–based topology optimization.* Structural and Multidisciplinary Optimization, 2021. **64**: p. 1127-1139.

La borsa di dottorato è stata cofinanziata con risorse del
Programma Operativo Nazionale Ricerca e Innovazione 2014-2020, risorse
FSE REACT-EU
Azione IV.4 “Dottorati e contratti di ricerca su tematiche dell’innovazione”
e Azione IV.5 “Dottorati su tematiche Green”